CORE-SHELL BASED METAMATERIALS: FABRICATION PROTOCOL AND OPTICAL PROPERTIES

Vashista C. de Silva, B.S.E.E, M.S.E.E.

Dissertation Prepared for the Degree of

DOCTOR OF PHILOSOPHY

UNIVERSITY OF NORTH TEXAS

December 2017

APPROVED:

Vladimir Drachev, Major Professor
Arup Neogi, Committee Member
Usha Philipose, Committee Member
Yuri Rostovtsev, Committee Member
Michael Monticino, Interim Chair of the Department of Physics
Su Gao, Dean of the College of Science
Victor Prybutok, Dean of the Toulouse Graduate School

De Silva, Vashista C. *Core-Shell Based Metamaterials: Fabrication Protocol and Optical Properties*. Doctor of Philosophy (Physics), December 2017, 93 pp., 7 tables, 49 figures, 110 numbered references.

The objective of this study is to examine core-shell type plasmonic metamaterials aimed at the development of materials with unique electromagnetic properties. The building blocks of metamaterials under study consist of gold as a metal component, and silica and precipitated calcium carbonate (PCC) as the dielectric media. The results of this study demonstrate important applications of the core-shells including scattering suppression, airborne obscurants made of fractal gold shells, photomodification of the fractal structure providing windows of transparency, and plasmonics core-shell with a gain shell as an active device. Plasmonic resonances of the metallic shells depend on their nanostructure and geometry of the core, which can be optimized for the broadband extinction. Significant extinction from the visible to mid-infrared makes fractal shells very attractive as bandpass filters and aerosolized obscurants. In contrast to the planar fractal films, where the absorption and reflection equally contribute to the extinction, the shells' extinction is caused mainly by the absorption. This work shows that the Mie scattering resonance of a silica core with 780 nm diameter at 560 nm is suppressed by 75% and only partially substituted by the absorption in the shell so that the total transmission is noticeably increased. Effective medium theory supports our experiments and indicates that light goes mostly through the epsilon-near-zero shell with approximately wavelength independent absorption rate. Broadband extinction in fractal shells allows as well for a laser photoburning of

holes in the extinction spectra and consequently windows of transparency in a controlled manner. Au fractal nanostructures grown on PCC flakes provide the highest mass normalized extinction, up to 3 m^2/g, which has been demonstrated in the broad spectral range. In the nanoplasmonic field active devices consist of an Au nanoparticle that acts as a cavity and the dye molecules attached to it via thin silica shell as the active medium. Such kind of devices is considered as a nano-laser or nano-amplifier. The fabricated nanolasers were studied for their photoluminescence kinetic properties. It is shown that the cooperative effects due to the coupling of dye molecules via Au nanoparticle plasmons result in bi-exponential emission decay characteristics in accord with theory predictions. These bi-exponential decays involve a fast superradiant decay, which is followed by a slow subradiant decay. To summarize, this work shows new attractive properties of core-shell nanoparticles. Fractal Au shells on silica cores prove to be a good scattering suppressor and a band pass filter in a broadband spectral range. They can also be used as an obscurant when PCC is used as the core material. Finally, gold nanoparticles coated with silica with dye results in bi-exponential decays.

ACKNOWLEDGMENTS

I am indebted to countless people for their help and guidance during my time at University of North Texas (UNT) and Purdue University. I would like to express gratitude to my major advisor, Prof. Vladimir Drachev, for his instructions, guidance and commitment in helping me achieve my goals. I owe special thanks to Prof. Vladimir Shalaev, my previous advisor, for his help and guidance throughout the time at Purdue. My committee members, Professors Arup Neogi, Usha Philipose, and Yuri Rostovtsev, have also graciously assisted during my doctoral research at UNT, and I thank them for their help. I would like to thank my fellow colleague Dr. Piotr Nyga, who provided help with me his knowledge in many fields, especially semi continuous metal films and my fellow graduate students, for the useful discussions we had over our research.

My in-laws and my family's love and support have given me the confidence to pursue my academic goals, and without them I would not be the man I am today. My most heartfelt thanks are for them.

Lastly but not leastly, a special thank you to my wife Athulya Hewawasam whose support, encouragement, patience and enduring love were unquestionably the firm foundation upon which the past years of my life have been built. Her tolerance of my occasional unrefined mood swings is a proof in itself of her unyielding devotion and love.

TABLE OF CONTENTS

LIST OF TABLES

LIST OF FIGURES

CHAPTER 1

INTRODUCTION

This dissertation is organized to first introduce important concepts and experimental procedures in the area of plasmonics and optical metamaterials relating to my doctoral research in physics at University of North Texas.

The document has several main sections. Chapter 1 explains how my topics are relevant to the fields and optics, plasmonics and metamaterials. Next section is the chapter 2, where I discuss optical properties of an isolated metal nanoparticles, core-shells with fractal or continuous metal structures. Optical properties of the core-shell structures further studied then with different core materials. The results of their extinction cross section spectra are normalized per mass and per particle number in both visible and mid infrared (mid-IR) spectral ranges in chapter 3. I describe optical properties and development of aerosol obscurants with pre-set windows of transparency using photo-modification in chapter 4. In chapter 5, I show how to achieve so called Kerker invisibility (scattering suppression) with fractal shells. Finally, in chapter 6, we have presented studies of emission kinetics of a core-shell based nanolaser.

1.1. Interaction of Light and Matter

We have been observing influence of light and matter often but hardly stop and think carefully on the physics behind such phenomena. When you are starting to think about the physics behind such phenomena, the topic of light and matter get more interesting. My research study is mainly about light interaction with metal. Therefore, let's discuss about light and metal. You shall see in next few chapters, the light can strongly couple into metal with certain conditions. This will introduce collective oscillations of the metal's free electrons known as plasmons. Optics of plasmonic materials has been my core focus for several years of the doctoral research at University of North Texas.

The field of plasmonics is studied broadly on how the electromagnetic (EM) waves interact with metal or metal-dielectric structures. For several thousand years its known that metal colloidal nanoparticles have interesting optical properties [7], ancient glassmakers had manufactured glass

FIGURE 1.1. 4th century A.D., Rome, the Lycurgus Cup viewed with transmitted light (left panel) and reflected light (right panel) [1].

by including certain metal nanoparticles. When the incident light hit the glass, it absorbs light in particular wavelength regions. This will give glass two different colors depending on whether the incident light is reflected off the glass or transmitted through the glass. This phenomenon of two colors, is called dichrosim in optics [8]. This is related to plasmon excitation in the metal nanoparticles. Such glasses are displayed in the British Museum and are a good example for dichroic glass from the 4th century A.D. [1] which is shown in figure 1.1. The Lycurgus cup with two different colors are coming from the absorption of small 20-50 nm size gold particles embedded in the glass of the Lycurgus cup. As the gold particles are embedded with the glass, the plasmonic excitations of electrons in the gold particles absorb and scatter blue and green light. Therefore, when a light source is placed inside the Lycurgus cup, someone sees as a reddish color due to absorption and scattering of green and blue light. When the light source is outside the cup, the reflected light from the glass gives greenish color. The dichrosim results in the Lycurgus cup is

due to plasmonic response of the metal-glass composite.

As we gathered from earlier, in order to discuss the optical properties of metal particles more clearly we need to discuss surface plasmon (SP) resonances. Let's consider metal particles embedded in dielectric host. Plasmons are defined by collective oscillations of conduction electrons in a metal particle or nanostructure.These plasmonic nanostructures can act as optical nanoantennas by acquiring and confining EM energy in a nanometer area, which are called "hot spots" [9, 10, 11]

Gold and silver metal particles are considered noble metals. SP resonances of noble metals appear from the ultra violet (UV) to the visible (Vis) parts of the EM spectrum. Wavelength of these optical resonances are determined by several conditions, such as the dielectric function of the metal, shape, size and the surrounding medium. In order to understand the material clearly we need to review electromagnetic concepts with plasmonics in particular. Starting with Maxwell's equations, their constitutive relations, and material's electric/magnetic properties can be found in number of textbooks, such as Jackson [12, 13]. Properties of the material or medium are governed by the electric and magnetic susceptibilities χ_e and χ_m. These susceptibilities are directly related to the material's permittivity ε and permeability μ.

(1) $$\varepsilon = \varepsilon_0(1+\chi_e) = \varepsilon_0\varepsilon_r = \varepsilon^{'} + i\varepsilon^{"}$$

(2) $$\mu = \mu_0(1+\chi_m) = \mu_0\mu_r = \mu^{'} + i\mu^{"}$$

Knowing the description of ε and μ for the material helps tremendously to understand the EM properties. As seen from equations 1, and 2 it is not always going to be constant value for ε and μ. These parameters can change with the frequency. It should also mention that these parameters are complex numbers. Material responses in equations 1, and 2 are the real and imaginary part of the ε and μ. These complex numbers help us to understand EM properties associated with different material, such as lossy and magnetic materials.

1.2. Background

In the past decade there had been much improvement in fabrication and characterization methods of fractal metal-dielectric nanostructures. These structures can be used in different applications due to high local field enhancement. Fractal metal-dielectric nanostructures can be divided into two different types, planar films and core-shell type nanostructures. Both types can be used in different applications, such as single molecule detection [14], surface-enhanced infrared (IR) absorption [15], and surface-enhanced Raman spectroscopy [16].

In my research work, I am concentrated on core-shell plasmonic nanostructures which are also belonging to the fractal metal-dielectric category. Optical properties of metallic core-shell nanostructures can be controlled by their composition, size and shape as planar counterpart where fractal metal-dielectric fabricated on substrate. Not like their planar counterparts, core-shell structures dispersible in liquids or air, showing strong scattering and/or absorption, are of interest for many applications including sensing [17], obscurants [18], enhanced biomedical imaging [19], photothermal therapy [19], photon-heat conversion based energy harvesting [20], and spaser [6]. Core-shell nanostructures are made by chemical synthesis of noble metal gold around the dielectric core. Here, the gold shell is synthesized as fractal (see section 2.5.2 for more details), which is also called semi-continuous metal film in literature. Plasmon resonances of these structures can be in broad spectral range depending percolation threshold [21] where metal fractals with random sizes and shapes present in the composite. As the fractal metal nanostructure reach the percolation threshold, it goes through changes between metallic and dielectric behaviours. Therefore, these nanostructures can support plasmon resonances in a very broad range. It has been shown that fractal metal films on planar substrates support broad spectral range resonances from ultra violet (UV) [21] to far infrared (IR) [22].

The purpose of my research is to study core-shell nanostructures with different types of materials and their optical properties with structural modifications. It allows as well for a laser photoburning of holes in the extinction spectra and consequently windows of transparency in a controlled manner. Applications such as aerosolized obscurants are very interesting due to significant extinction from the visible to mid-IR fractal shells. The extinction of the fractal shell is mainly

caused by the absorption so that the total transmission of the core material can be increased and can be used towards invisibility and cloaking devices. The fractal nanostructures grown on different sized and shaped core materials with optimization have shown highest mass normalized extinction over broad spectral range from UV to far IR. Inverse design of above core-shell nanostructure is also being studied, which has a gold core and silica shell provides insight on spaser based nanolaser and their emission kinetics. Fluorescent dye molecules are doped over a core-shell nanoparticle. The emission from the dye excites and drives the nanolasing of the core-shell nanostructure and enhanced fluorescence is observed.

CHAPTER 2

OPTICAL PROPERTIES

The chapter 2 starts with a brief introduction to the plasmonic and scattering properties of a single metal particle, dielectric-metal:core-shell particles, and fractal metal films. First, I describe the plasmonic properties of noble metal particles and thin metal films and the theories used to model them are discussed. Secondly, scattering and extinction spectra of individual metal particles and their dependence on the host material permittivity and the shape of the particles are discussed.

2.1. Plasmonic Basics of Single Metal Nanoparticles

Noble metal nanoparticles are known for their optically striking vivid colors. These colors are the substantiation of SP resonances. SP resonances are excited by external light at optical frequencies. Definition of the SPs is listed as follows. The collective oscillations of conduction electrons in metal structure are excited by an external field results in highly localized fields called SPs by providing matching conditions for both external field and the collective oscillations. The resonance frequency of these SPs depend on the dielectric functions of the metal and the host medium as shown in figure 2.1 in addition to the shape and size of the metal particle.

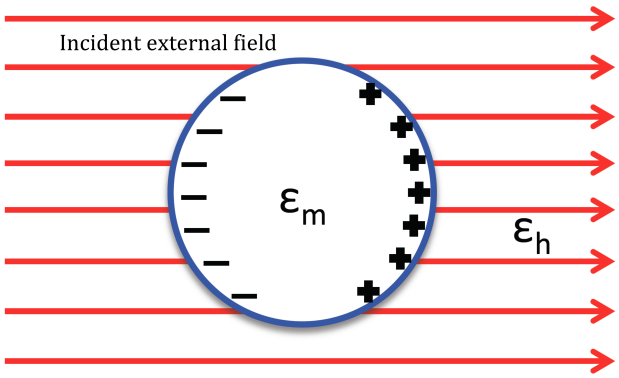

FIGURE 2.1. Excitation of particles plasmons through the polarization of metallic nanoparticles.

Figure 2.2 shows spectral position of the these plasmon frequencies for different shapes and sizes of the metal particles. Here N is the number of electrons, e is the electron charge, m is the mass of an electron, and ε_0 is the free space permittivity, and l is the charge density distributions

of polarity. l can have values 1,2,3. With increasing sphere surface l can have higher values than the dipole (l=1) [23] (l=2 and 3 are quadrupole, and multipole plasmons respectively)

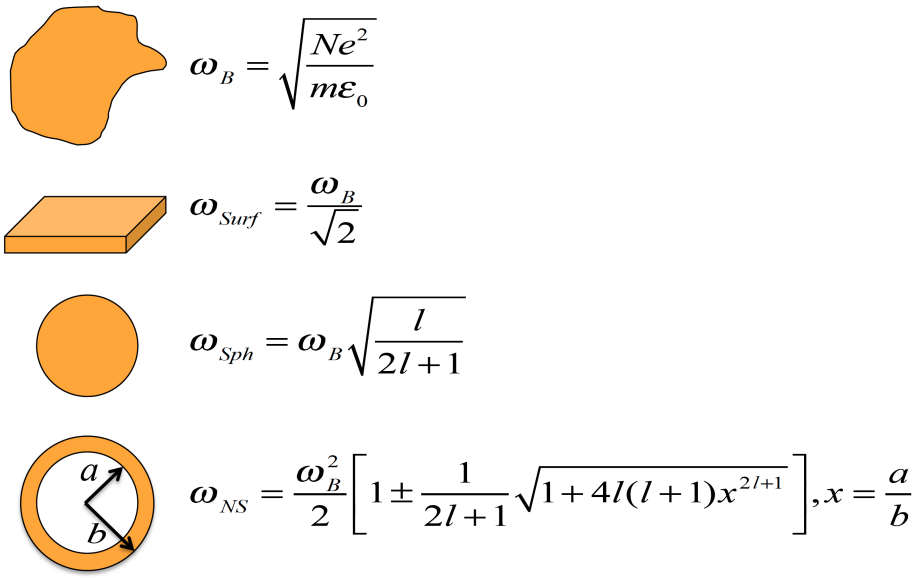

FIGURE 2.2. The plasmon energies and shapes.

To visualize SP phenomena, let's consider a metallic sphere in a diaelectric host medium with electromagnetic (EM) field. In a quasi-static approximation, the metal sphere with radius R which is much smaller than the EM wave's wavelength R$\ll \lambda$. This way the phase of the EM field all across the metal sphere is considered constant. This approximation is only good for particles with diameter in the order of tens of nanometers and smaller. As seen from the section 2.1, incident EM field change the conduction electrons with reference to the positive ions. This kind displacement outcomes in a restoring force of the conduction electrons, which leads to oscillations. When the frequencies of the electric field and SPs in resonance,the oscillations result in enhanced EM field inside the metallic sphere and near the embeded dielectric medium. Due to the EM field applied, polarizability, α of the metallic sphere can be calculated using the boundry conditions and defined through (for details see the example [12, 2])

(3) $$\mathbf{P} = \varepsilon_h \alpha \mathbf{E}_0$$

where

$$\alpha = 4\pi R^3 \left(\frac{\varepsilon_m - \varepsilon_h}{\varepsilon_m + 2\varepsilon_h}\right) \tag{4}$$

Here P is dipole moment, ε_m and ε_h are the permittivity of the metal sphere and host medium, and R is the radius of the sphere. The polarizability is the largest when the denominator in the equation 4 is a minimum. Then the system mentioned in figure 2.1 is excited on resonance as the denominator approaches to zero and maximum polarizability is obtained. Vivid colors mentioned at the beginning of this section comes from SP resonance in the polarizability of the metal particle and host medium. This is happening because the cross-sections of scattering and absorption of the radius, R of this particle is much smaller than the wavelength.

2.2. Basics of Light Scattering and Absorption

This section will provide brief overview of scattering of plane EM waves. This will not provide a comprehensive explanation of all scattering as this brief overview will provide information related to my research studies. More completed text about scattering can be found through Bohren and Huffman [2] and van de Hulst [24] and I have used them as reference for this section.

In EM experiments, more often, the only waves detectors collect are scattered EM waves as opposed to absorbed waves. If you think about the everyday life, we do mostly deal with scattered waves. Let's consider few examples: an object can be seen as light scattered from the object, and the sky can be seen because of light from the sun is scattered by the atmosphere. The colors we see daily are the result of different scattering efficiencies of various frequencies when an object scatters light. If we see blue from an object, that means the object scatters blue light more efficiently than other colors, and other colors may have been absorbed by or transmitted through the object.

Before we begin the mathematical introduction of scattering and absorption, let's consider particular scattering regimes with respect to the incident EM wavelength and particle dimensions. There are two regimes, namely Rayleigh and Mie. The Rayleigh regime is used for particle sizes are much smaller than the wavelength ($R \ll \lambda$), and the Mie regime is used for particle sizes are on the order of the wavelength or larger ($R \geq \lambda$). If the particle sized are much larger than the wavelength ($R \gg \lambda$), then the ray optics can be used easily. Both Rayleigh and Mie scattering are

used as elastic scattering, where there is no energy lost during the scattering; incident wavelength is equal to the scattered wavelength. But inelastic scattering, on the contrary, happens when there is energy lost in the scattered wave. In this case, incident wavelength is not equal to the scattered wavelength due to the energy lost. We don't discuss inelastic scattering in this document. My goal is to provide basic understanding about scattering, extinction and absorption concepts of random metal-dielectric core-shell structures and their small metallic scatters.

This study considers only single scatter events, which means that EM plane wave is incident and scattered away from the particle without any other scattering events from other particles. That is the situation when the particle is independent from other neighbouring particles. For more information about multiple scattering, advanced EM texts such as Jackson [12] would be helpful.

Basic mathematics for single scatter with arbitrary shape are described here for scattering and extinction cross sections. To introduce the basic mathematical concepts of the scattering for rest of the sections, Bohren and Huffmans book as the reference [2] has been used as the reference.

When a small object is incident by a light source, it generates radiation due to the electron oscillation. This radiation process is called the scattering. If an object transfers the incident energy to a different energy (e.g. heat), the incident energy is absorbed by the object. The extinction is defined as the contribution from both the scattered and absorbed light from the incident light by the object, and therefore the extincted energy is the sum of both the absorbed and scattered energy.

We begin with Maxwell's equations to solve the problem of absorption and scattering of light by a small spherical particle with the correct boundary conditions. We use the general formulation of the problem as shown in figure 2.3.

$$\nabla^2 E + k^2 E = 0 \qquad \nabla^2 H + k^2 H = 0 \tag{5}$$

Where

$$k = \sqrt{\omega^2 \varepsilon \mu} \tag{6}$$

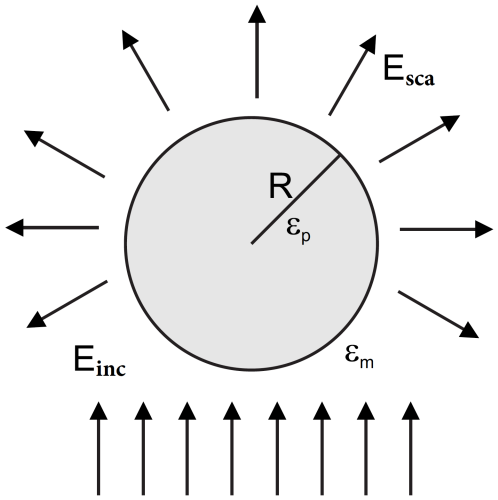

FIGURE 2.3. An object with optical constants ε_p is embedded in a medium with optical constants ε_m, and incedent by a plane wave with an electric field E_{inc}. The object radiates a scattered field in all directions, to an electric field E_{sca} outside of the object.

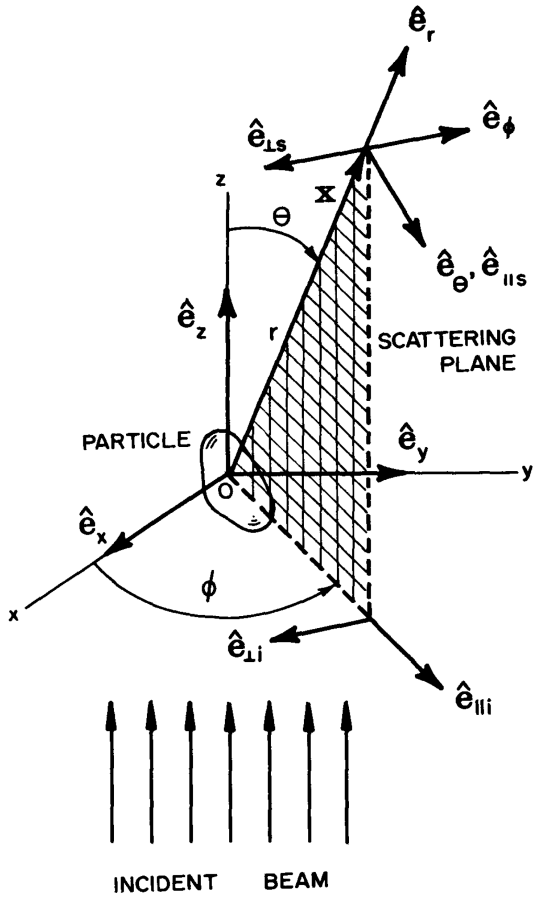

FIGURE 2.4. Scattering Coordinates system.[2]

the parameters of both particle and medium are described with the electric permitivity (ε) and magnetic permeability (μ) (Relative μ of the material under study is set to be 1). The electromagnetic field is satisfied the Maxwell equations at points where ε and μ are discontinuous at the boundary due to microscopic properties between the boundary of particle and medium as they crosses. For such conditions we can apply the following to the fields:

$$[E_2(x) - E_1(x)] \times \tilde{n} = 0$$
$$[H_2(x) - H_1(x)] \times \tilde{n} = 0 \tag{7}$$

x on S where $\tilde{n}$ is normal to the particle surface.

We can find the relationship between incident and scattered electric fields of a plane wave

from an object using the S-matrix and the boundary conditions. The S-matrix is used to find the relationship between initial and final conditions of an object when it interacts with fields, this has been used in quantum mechanics, scattering, and many other applications.

From figure 2.4, it is convenient to write the incident electric field in the components of parallel and perpendicular as the scattering plane lies.

$$E_i = (E_{0\shortparallel}\hat{e}_{\shortparallel i} + E_{0\perp}\hat{e}_{\perp i})\exp(ikz - i\omega t)$$
$$E_i = E_{\shortparallel i}\hat{e}_{\shortparallel i} + E_{\perp i}\hat{e}_{\perp i} \tag{8}$$

$$\hat{e}_{\perp i} = \sin\phi\hat{e}_x - \cos\phi\hat{e}_y$$
$$\hat{e}_{\shortparallel i} = \cos\phi\hat{e}_x + \sin\phi\hat{e}_y \tag{9}$$

We can also write incident electric field with x, and y components as follows;

$$E_{\shortparallel i} = E_{xi}\cos\phi + E_{yi}\sin\phi$$
$$E_{\perp i} = E_{xi}\sin\phi - E_{yi}\cos\phi \tag{10}$$

And the scattering filed is written as follows;

$$E_s = E_{\shortparallel s}\hat{e}_{\shortparallel s} + E_{\perp s}\hat{e}_{\perp s} \tag{11}$$

The amplitude of the scattered field by an object is linearly proportional to incident field due to the linearity stated in the equation 7. Therefore, the comparison between the incident and scattered fields can be written in matrix form. S-Matrix describe here is a 2x2 unitary matrix.

$$\begin{bmatrix} E_{\shortparallel s} \\ E_{\perp i} \end{bmatrix} = \frac{e^{ik(r-z)}}{-ikr} \times \begin{bmatrix} S2 & S3 \\ S4 & S1 \end{bmatrix} \begin{bmatrix} E_{\shortparallel i} \\ E_{\perp s} \end{bmatrix} \tag{12}$$

This problem is solvable when spherical particles are considered. It was Gustav Mie in 1908 [25] who first showed this, then Bohren and Huffman [2] completed the derivation of Mie theory. We can get so much information from completed scattering matrix which is derived from Mie theory. This includes polarization dependence of scattered light, and more importantly the cross sections, which give the geometrical understanding of how the incident field is to the scattered, absorbed or extincted power.

$$C_{sca} = \frac{P_{sca}}{I_{inc}} \qquad C_{abs} = \frac{P_{abs}}{I_{inc}} \qquad C_{ext} = \frac{P_{ext}}{I_{inc}} \tag{13}$$

the absorption cross section can be defined as follows since extincted power is simply the sum of the scattered and absorbed power.

$$C_{abs} = C_{ext} - C_{sca} \tag{14}$$

2.3. Scattering Regimes

Scattering regimes can be described by three models depending on the size parameter, x which is defined as x=$\frac{2\pi r}{\lambda}$. Here numerator is the circumference of the object and the denominator is the incident wavelength. Based on the x value, three regimes are:

- $x \ll 1$ is the Rayleigh scattering region where particle sizes are much smaller than the wavelength of light.
- $x \approx 1$ is the Mie scattering region where particle sizes are comparable to the wavelength of light
- $x \gg 1$ is the geometric scattering region where particle sizes are much larger than the wavelength of light.

2.3.1. Rayleigh Theory

In the Rayleigh theory approach, where $x \ll 1$, the electromagnetic field is uniform over the whole particle volume. We can use boundary conditions for quasi-static approximation and get

equations 3, and 4 mentioned in section 2.1. In the Rayleigh region absorption and scattering cross sections are [2]:

$$C_{sca} = \frac{8\pi}{3} k^4 R^6 Re\left[\frac{\varepsilon_m - \varepsilon_h}{\varepsilon_m + 2\varepsilon_h}\right]^2$$
$$C_{abs} = 4\pi k R^3 Im\left[\frac{\varepsilon_m - \varepsilon_h}{\varepsilon_m + 2\varepsilon_h}\right] \tag{15}$$

Where **Re** is the real part of the expression and **Im** is the imaginary part of the expression. Here $k = \frac{2\pi}{\lambda}$ and efficiencies are defined as $Q = \frac{C}{\pi r^2}$. When we are looking at the efficiencies, we see that $Q_{sca} \propto \frac{1}{\lambda^4}$ and $Q_{abs} \propto \frac{1}{\lambda}$.

In 1871 Lord Rayleigh tried to explain the blue color of the sky and red color of the sunset. This was the first quantitative theory of the scattering. Let's consider what Rayleigh scattering is: that is when the electromagnetic wave is in contact with a particle (atom/molecule) and creates a dipole moment, Equation 3, as the electrons move up and down. The frequency of this oscillating dipole is same as the incident wave, and this is called the Rayleigh scattering.

Q_{sca}, scattering efficiency, is inversely proportional to λ^4, which means shorter wavelengths will give higher efficiency compared to longer wavelength. e.g. $\lambda = 475nm$, blue light, is factor of 4.2 times as efficient as $\lambda = 680nm$, red light. Also different molecules/atoms/particles will have different scattering efficiencies as they have different number of electrons in different configurations.

2.3.2. Mie Theory

When it comes to $x \approx 1$, Rayleigh scattering approximation is not applicable. The reason is that electromagnetic field is not uniform over the whole particle volume. Such particles are too small to make use of geometric scattering theory. Therefore, it is necessary to make use of Mie theory and it addresses scattering and absorption of a plane wave by a homogeneous sphere. Equations for scattering and absorption are derived from solving Maxwell's equations with the regions including inner and outer of the sphere boundary conditions. Mie theory can give better understanding of scattering and absorption properties of spherical particles (or not so spherical)

on the order of a wavelength. Particle size with the order of wavelength gives mainly forward scattering with very limited wavelength dependence. Therefore, all the light scattered by visible wavelengths is almost the same. That's the reason why we see clouds as white color: when sunlight hits the water vapor which are about micron in size, sunlight scatters all the colors in the visible spectrum equally to give white color.

Mie theory considers the electromagnetic fields (inside and around) of the particle. These fields were found using spherical harmonics or Bessel functions in terms of vector harmonics **M** and **N** of the wave function ψ.

$$
\begin{aligned}
M_{emn} &= \bigtriangledown \times (r\psi_{emn}) \\
M_{omn} &= \bigtriangledown \times (r\psi_{omn}) \\
N_{emn} &= \frac{\bigtriangledown \times M_{emn}}{k} \\
N_{omn} &= \frac{\bigtriangledown \times M_{omn}}{k}
\end{aligned}
\tag{16}
$$

"e" and "o" denote even and odd harmonics modes respectively. Incident electrical plane wave and internal electromagnetic waves are written as the following equations in terms of vector spherical harmonics.

$$
\begin{aligned}
E_{inci} &= E_0 \sum_{n=1}^{\infty} (i)^n \frac{2n+1}{n(n+1)} (M_{oln}^{(1)} - iN_{eln}^{(1)}) \quad and \quad E_n = E_0 (i)^n \frac{2n+1}{n(n+1)}, \\
E_{inci} &= \sum_{n=1}^{\infty} E_n (M_{oln}^{(1)} - iN_{eln}^{(1)}), \\
E_{inner} &= \sum_{n=1}^{\infty} E_n (c_n M_{oln}^{(1)} - id_n N_{eln}^{(1)}), \\
H_{inner} &= \frac{-k_1}{\omega \mu_1} \sum_{n=1}^{\infty} E_n (d_n M_{oln}^{(1)} + ic_n N_{eln}^{(1)}).
\end{aligned}
\tag{17}
$$

Here the coefficients c_n and d_n are calculated through boundary conditions of E_n, and μ_1 is defined as the permeability of the particle. k_1 is the wave number of the particle. The $^{(1)}$ is the

radial dependency of the wave function, and it is defined as the first kind of the spherical Bessel functions. Finally, the scattered electromagnetic fields are expressed as follows.

$$
\begin{aligned}
E_{sca} &= \sum_{n=1}^{\infty} E_n(ia_n N_{eln}^{(3)} - b_n M_{oln}^{(3)}), \\
H_{sca} &= \frac{k}{\omega\mu} \sum_{n=1}^{\infty} E_n(ib_n N_{oln}^{(3)} + a_n M_{eln}^{(3)}).
\end{aligned}
\tag{18}
$$

As described for equation 17 here also the coefficients a_n and b_n are calculated through boundary conditions. k is the wave number of the particle. The $^{(3)}$ is the radial dependency of the wave function, and it is defined as the third kind of the spherical Bessel functions or some call it spherical Hankel functions.

The scattering and extinction cross sections can be calculated from the following equation.

$$
\begin{aligned}
C_{sca} &= \frac{2\pi}{K^2} \sum_{n=1}^{\infty} (2n+1)(\mid a_n \mid^2 + \mid b_n \mid^2) \\
C_{ext} &= \frac{2\pi}{K^2} Re(a_n + b_n)
\end{aligned}
\tag{19}
$$

a_n and b_n are called the scattering coefficients. They consist of Ricatti-Bessel functions, size parameter, and dielectric function of the particle and the medium. If the reader is interested in learning further about equations 16,17, 18, and 19 please find the Bohren and Huffman book [2] pages 83-103.

2.3.3. Coated Sphere

The electromagnetic field scattered by coated spherical particle has the same form as the one described in the Mie Theory section. However, the scattering coefficients, a_n and b_n are depend on the radial changes of ε and μ.

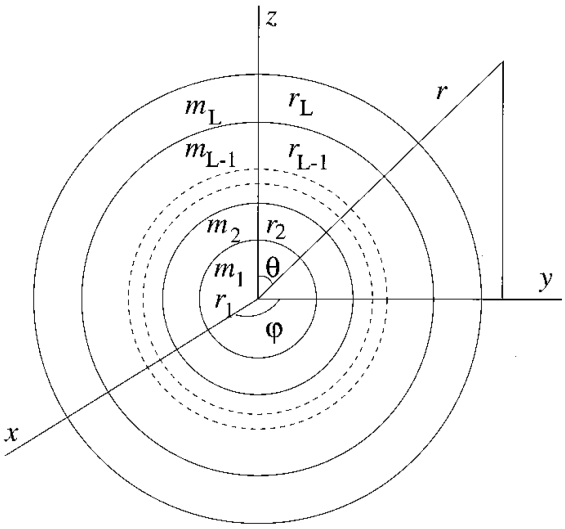

FIGURE 2.5. Geometry of a multilayered coated sphere [3].

Above in figure 2.5 with spherical geometry is commemorating to the scattering of a plane wave upon a multilayered sphere. m_L is the complex refractive index of the L^{th} material shell, r_L is the outer radius of the shell, and L^{th} layer is defined as $x_L = \frac{2\pi r_L}{\lambda}$ where λ is the wavelength of the incident plane wave. Since there are multiple boundary conditions to be considered at the interfaces of different regions, they can be expressed in an infinite series of spherical harmonics. The scattering coefficients can be expressed as the following equations.

$$a_n = \frac{\psi_n(x_L)}{\xi_n(x_L)} \bullet \frac{H_n^a(m_L x_L) - m_L D_n^{(1)}(x_L)}{H_n^a(m_L x_L) - m_L D_n^{(3)}(x_L)}$$
$$b_n = \frac{\psi_n(x_L)}{\xi_n(x_L)} \bullet \frac{m_L H_n^b(m_L x_L) - D_n^{(1)}(x_L)}{m_L H_n^b(m_L x_L) - D_n^{(3)}(x_L)} \quad (20)$$

Where $D_n^{(1)}(x_L)$, and $D_n^{(3)}(x_L)$ are the logarithmic derivatives of the RicattiBessel functions. H_n^a and H_n^b are added as the recursive functions. These functions are with logarithmic derivatives and ratios of the RicattiBessel functions seen from the equation 20. There have been many numerical methods introduced to predict scattering and absorption properties of the coated sphere. The evaluation of these scattering coefficients, a_n and b_n are explained in textbooks and peer-reviewed journals. Namely, Bohren-Huffman [2] and Aden-Kerker [26] and found that there

are still simulation difficulties due to computation problems with the RicattiBessel functions. In order to overcome these difficulties, the algorithm by Wu [3] introduce the procedure stated above that involves logarithmic derivatives and ratios of the Ricatti-Bessel functions. This procedure helps to avoid computational difficulties. This improved numerical method was used to analytically calculate scattering and absorption coefficients of the fabricated core-shell nanostructures with modified shells using Effective Medium Theory (EMT).

2.4. Effective Medium Theory (EMT)

Most of the research is based on core-shell type nanostructures with metal fractals as the shell. These metal fractal shells are quite complex with random geometries. One could use Maxwell's equations to obtain the optical properties of the core-shell by calculating all the random geometries. Even though this is a very accurate procedure, it will be hard to manage as it needs the geometry of the fractals exactly. Therefore, this is an extremely difficult problem for fractal nanostructures that is considered in this research work. But there is a more efficient way of finding needed optical properties of these core-shell structures: that is by finding the effective properties of the structure. This can be done without analyzing or measuring the precise geometry of the fractal shell, but by finding the filling fraction f and permittivity ε_m material that embedded in a host material. With knowing material's complex dielectric functions ε_m, host material's ε_h, and filling fraction f, one could replace the complicated fractal shell by a uniform and homogeneous film with the same thickness and an effective permitivity ε_{eff}. The core-shell structure with an effective shell will give the same far-field optical response as the actual sample. There are a few effective medium methods to be used but there are most commonly used two methods been used to find optical properties. They are called Maxwell Garnett Theory (MGT) [27], and Bruggeman's Effective Medium Theory (EMT) [28]. There are also other methods that can be used to calculate optical properties of random metal structures, namely spectral [29] and scaling [30] theories. Maxwell Garnett theory is used for the cases where the fractals are well separated from each other and embedded in a host medium.

(21) $$\frac{\varepsilon_{eff}-\varepsilon_h}{\varepsilon_{eff}+(d-1)\varepsilon_h}=f\frac{\varepsilon_m-\varepsilon_h}{\varepsilon_m+(d-1)\varepsilon_h}$$

As seen from the MGT equation 21, ε_{eff} can be calculated by using known ε_m, ε_h, d (dimension), and f. MGT only works for the fractals with separated inclusions that are embedded in a host material. The derivation of the effective permitivity, ε_{eff} is explained in books by Shalaev [29] and Kreibig [31]. The problem with this method is that MGT is not symmetrical when it comes to ε_m, and ε_h as seen from the equation 21. Asymmetry is particularly strong when the difference between the permittivities is larger. The MGT equation can be used and generalized so that the two inclusions show symmetry. This is done by introducing two filling factions f_1 and f_2 for both inclusions and permittivities ε_1 and ε_2 respectively, in a host medium with permittivity ε_h.

(22) $$\frac{\varepsilon_{eff}-\varepsilon_h}{\varepsilon_{eff}+(d-1)\varepsilon_h}=f_1\frac{\varepsilon_1-\varepsilon_h}{\varepsilon_1+(d-1)\varepsilon_h}+f_2\frac{\varepsilon_2-\varepsilon_h}{\varepsilon_2+(d-1)\varepsilon_h}$$

MGT works well for low concentration of metal f but for higher metal f concentrations Bruggeman's Effective Medium Theory (EMT) is used widely. Equation 22 can be used to explain Bruggeman's EMT. For this, both ε_1 and ε_2 are addressed as inclusions with filling fractions f_1 and f_2 embedded in an effective medium with permittivity ε_{eff}. This means the host medium is treated as the effective medium and it implies that ε_h=ε_{eff}.

(23) $$0=f_1\frac{\varepsilon_1-\varepsilon_{eff}}{\varepsilon_1+(d-1)\varepsilon_{eff}}+f_2\frac{\varepsilon_2-\varepsilon_{eff}}{\varepsilon_2+(d-1)\varepsilon_{eff}},\quad and\quad f_1+f_2=1,$$

Also equation 23 can be used for any number of materials by generalizing in the following:

(24) $$\sum_i\frac{\varepsilon_i-\varepsilon_{eff}}{\varepsilon_i+(d-1)\varepsilon_{eff}}$$

The equation 23 is a quadratic and has solutions as the following which are explained in

more details through Bergman [32].

$$\varepsilon_{eff} = \frac{1}{2(d-1)}[d(f_1\varepsilon_1 + f_2\varepsilon_2) - \varepsilon_1 - \varepsilon_2 \pm \sqrt{(d(f_1\varepsilon_1 + f_2\varepsilon_2) - \varepsilon_1 - \varepsilon_2)^2 + 4(d-1)\varepsilon_1\varepsilon_2}] \quad (25)$$

The solution for the equation 25 is chosen with positive imaginary part of the effective permittivity due to the causality in the media. Also this ε_{eff} is been calculated such that any type of material can be chosen as the host material which is a great advantage and major difference of Bruggeman's EMT over Maxwell Garnett MGT formulation.

Let's consider a hypothetical nanostructure consisting of a dielectric core and a metal shell (core-shell microsphere). By using above equation 25 for the metal shell and equation 19 for finding the extinction cross-section, we can get an idea how the Q_{ext} behaves for the core-shell microsphere with a fractal metal shell. In this example, I have used r= 400 nm silica microsphere with 50 nm thick gold shell with different filling fractions, f.

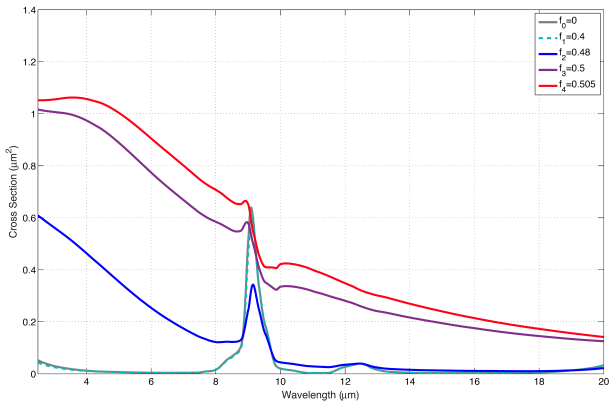

FIGURE 2.6. Q_{ext} of 50 nm shell (shell thickness) on a Silica sphere with 400nm (Core radius) $f_0 = 0$ (Bare Silica), $f_1 = 0.4$, $f_2 = 0.48$, $f_3 = 0.5$, and $f_4 = 0.505$ (simulated with Mie theory for coated sphere with EMT for shell's effective permittivity, and fractal shell dimension is set to 2).

It can be seen that in the above figure 2.6, the EMT coated shell, for low gold concentration or filling fraction, has no extinction for shorter and longer wavelengths except Si-O-Si vibrational band at 9 μm. This is because extinction (absorption+scattering), in this case absorption of the

plasmon resonances is not present above gold plasmon resonance which is around 560 nm (for single gold nanoparticles). But as the gold filling fraction grows, at some point it shows broad and almost wavelength independent extinction cross-section. This is due to the fact that there are no more single gold nanoparticles, instead there are some fractal like gold structures created on the shell as filling fraction increases. Therefore, different size of fractals provide broader absorption through out the spectrum.

2.5. Methods and Materials

2.5.1. Synthesis of SiO_2 Core Au Shell Microspheres

Silica microspheres (Bangs Lab) with diameters of about 0.5 μm, 0.8 μm, 1.8 μm and 4.5 μm were coated with gold nanostructures using a modified method of the reduction of gold salt, chloroauric acid ($HAuCl_4$) with formaldehyde (CH_2O) in the presence of surfactants and stabilizers. The reduction method was initially developed for continuous shells [33, 34], where the silica surface must be seeded with gold nanoparticles prior to shell growth (see figure 2.7). The seeding step was omitted in our experiments and the chemicals concentrations were adjusted to facilitate fractal growth rather than continuous shells.

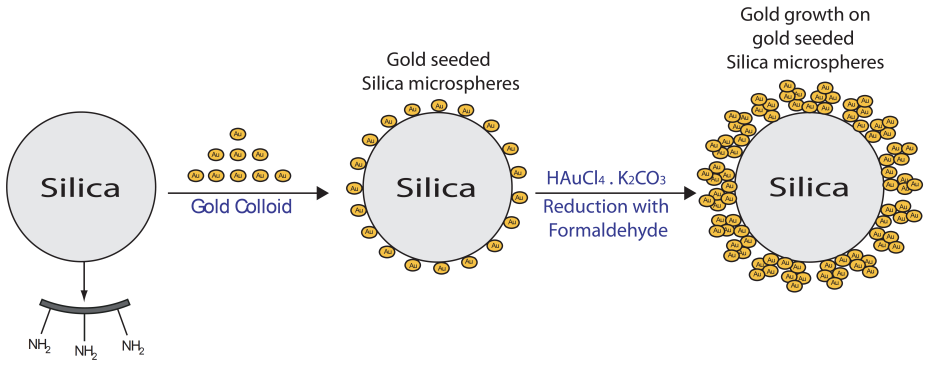

FIGURE 2.7. Synthesis of continuous shell.

2.5.2. Synthesis of Fractal Core-Shell

In order to fabricate fractal shells, gold was directly synthesized on the amino functionalized silica microspheres. The surface coverage of the gold on the microsphere surface was varied for different samples by varying the reduction time. Specifically, 30 mg of potassium carbonate

(K_2CO_3) was dissolved in 100 mL of ultra-pure water with 18.2 MOhms resistivity. The solution was stirred for 10 minutes, and 300 μL of 50 mM $HAuCl_4$ was added into the solution. Next, amine functionalized silica microspheres followed by 40 μL of 0.36 mM CH_2O were added to the vigorously stirred solution. After the growth of the gold shells, the shell surface was stabilized with polyvinylpyrrolidone (PVP) to prevent aggregation of the microspheres. Finally, the solution was centrifuged to collect gold-coated silica microspheres and remove the residual reagents. Collected particles were re-dispersed in ultra-pure water and centrifuged a few times to further remove residual reagents.

2.5.3. Synthesis of Coreless Fractal Shells

Synthesis of coreless fractal shells were made by etching away the silica core of our standard core-shell colloid. This was done using buffered hydrofluoric acid (BHF), which is a silicon dioxide (SiO_2) etchant. Fabricated core-shell structures were submerged in the BHF solution for 5-10 minutes. Then the particles were separated by washing with ultrapure water several times.

2.5.4. Synthesis of Au Fractal Shells on Precipitated Calcium Carbonate

Synthesis of Au fractal shell on precipitated calcium carbonate (PCC) was slightly modified relative to the Au-SiO_2 procedure. Namely, the PCC surface was first modified with amino groups. To accomplish this, 0.52 g of PCC (700 nm median size) was suspended in absolute ethanol and stirred for 30 minutes at a rate of 1000 rpm. Then 50 μL of 3-aminopropyltriethoxysilane (APTES) was added drop wise and the solution stirred overnight (12 hours). Stirring was stopped when the two layers of separation were observed. The APTES coated PCC were in the lower part, as they precipitated to the bottom. The solution was refluxed for one more hour to ensure the amino groups bonded to the PCC surface as covalent bonds. These particles were centrifuged several times in order to remove the residues. As the result of Au reduction performed with the reduction of gold salt, chloroauric acid ($HAuCl_4$) with formaldehyde (CH_2O) in the presence of surfactants and stabilizers (see section 2.5.2 for more details), the Au fractal shell was then formed on the amino group modified surface of PCC particles. Shell structure was controlled by varying the PCC concentration and reduction time. PCC was provided by Specialty Minerals. The chemicals, PVP,

$HAuCl_4$, K_2CO_3, and CH_2O were purchased from Sigma-Aldrich.

2.5.5. Electron Microscopy

The field emission scanning electron microscope (FESEM) images provide the structural characterization of the samples including metal coverage. Consequent analysis gives the fractal dimension, particles mean size, and the particle surface density.

2.5.6. Substrate Preparation

In order to deposit coated spheres on substrates as a mono layer, substrates were prepared with proper cleaning and coating.

First the glass substrates are cleaned with Piranha cleaning solution (mixture of sulphuric acid (H_2SO_4) and hydrogen peroxide (H_2O_2), then rinsed with ultra purer water 5-10 times and blow dried with N_2. For ZnSe use acetone and methanol rinses and blow dry with N_2.

PVP (Poly (Vinyl Pyridine)) Coated Substrates

Make 1% PVP solution (300 mg of PVP, M.W. 40K in 30 mL of EtOH, Ethanol). Submerge substrates in the 1% PVP solution for 12-14 hours. Take the substrate out and rinse with EtOH couple of times and dry it with N_2.

Polyelectrolyte Coated Substrates

The following polymers were prepared and used. Polycation Solution: PDADMAC (Poly (diallyldimethylammonium chloride)), M.W. 100K-200K in 0.5M NaCl. Polyanion Solution: PSS (Poly (sodium 4-styrenesulfonate)), M.W. 70K in 0.5M NaCl.

Glass has negative surface charge. Therefore, submerge substrate in Polycation solution and keep it for 10-20 minutes and wash the substrate with ultra pure water. Now submerge the substrate in Polyanion and keep it for 10-20 minutes and wash the substrate with ultra pure water. Repeat this procedure couple of times till you gets 5-10 bilayers. Final layer should depend on the surface charge of the particles.

The following FESEM images show an example of the monolayer results.

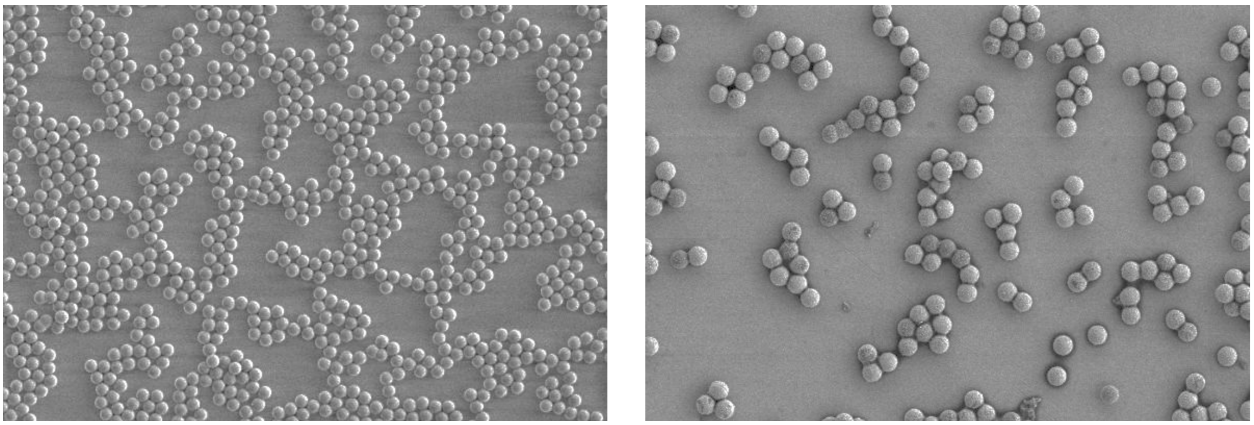

FIGURE 2.8. Gold coated silica microspheres in PVP coated ZnSe.

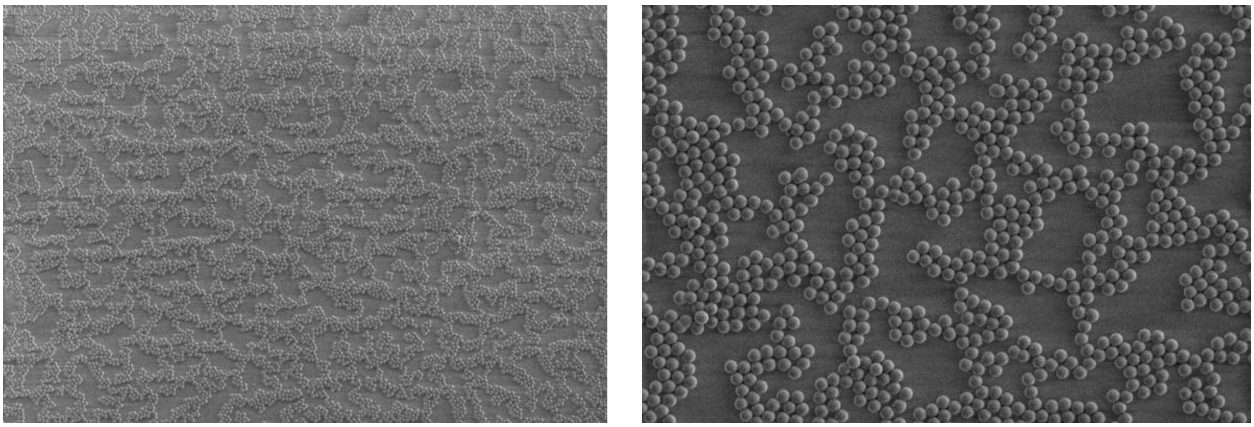

FIGURE 2.9. Gold coated silica microspheres in polyelectrolyte coated glass.

2.5.7. Fractal Dimension

To find the fractal dimension, first we use a SEM image (see figure 2.10) with high magnification where we can see the fractals clearly. The red color circle below is broken into smaller circles, each of which is smaller in size of the original. In this case it takes N smaller circles to cover the original, where N is the number of small circles that enveloped by the larger circle, R/R_o is the ratio to which the smaller circles compare to the larger one and D is the dimension. To calculate accurate D, make another circle inside the first circle and do the same procedure. D can be approximated accurately by repeating this process 3-4 times.

It was calculated as the power dependence of the number of gold nanoparticles N_P inside the circle of radius R, $N_P/N_o = (R/R_o)^D$, where N_o is the number of nanoparticles in a small reference circle of radius R_o.

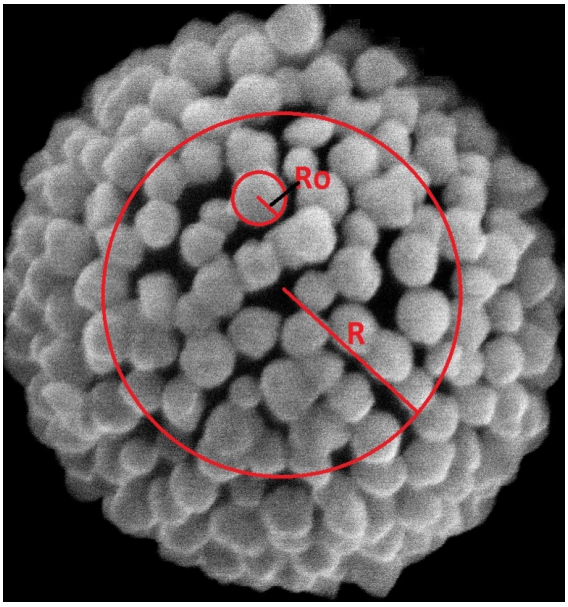

FIGURE 2.10. Fractal Dimension.

2.5.8. Optical Spectroscopy

The synthesized gold-coated microspheres were deposited as a sub-monolayer on zinc selenide (ZnSe) substrates for infrared spectroscopy and on fused silica substrates for spectroscopy in the visible range. A drop-and-dry method was used for highly uniform distribution. The ultraviolet visible (UV-Vis) and infrared (IR) extinction spectra were collected using UV-Vis-near IR and FTIR spectrometers and normalized by the particles surface density (particles per μm^2).

2.5.9. Laser Photomodification

The laser used for photomodification studies was a 10.6 μm pulsed MTL-3GT Mini TEA CO_2 laser (Edinburgh Instruments Ltd.). The laser radiation was linearly polarized and the pulse duration was 50 ns with 1 Hz repetition rate. The laser radiation was linearly polarized. For energy densities of up to 450 mJ cm^{-2}, a single pulse was used to modify the desired area of a sample. For higher energy densities, the laser beam was focused with a ZnSe lens to reach the required energy density. The desired size of the Photomodification area was obtained by scanning the sample with a 2D computer-driven motorized stage system.

CHAPTER 3

OBSCURANTS

3.1. Background on Obscurants

Optical properties of metallic nanoparticles can be controlled by their composition, size and shape. Nanoparticles dispersible in liquids or air, showing strong scattering and/or absorption (extinction), are of interest for many applications including obscurants [18], photothermal therapy [19], enhanced biomedical imaging [19], photon-heat conversion based energy harvesting [20], and sensing [17]. Depending on the application, specific optical properties and spectral bandwidth are required. Most of the applications rely on optical properties in the visible and the near-infrared. Some, like photothermal therapy and photon-heat conversion, require strong absorption. For others like biomedical imaging, strong scattering is important.

Obscurants can be divided into two categories such as anthropogenic and naturally existing particles, which can be suspended in air. These particles are used to obscure the particular parts of the electromagnetic (EM) spectrum by either blocking or weakening the transmission. Hygroscopic chloride smoke, and alkali halide smoke are some examples of anthropogenic obscurants. Dust, fog, and mist are some examples of natural obscurants. Use of obscurants is one of the oldest war techniques used decades ago, however details about these techniques have yet to be found due to the time period, but some information can be found in historical scripts, and it dates back to 200-1500 BC [35, 36].

In order to use particles as efficient obscurants we need to define a proper measuring scale to identify which ones are stronger or weak obscurants. For this, extinction spectra normalized by mass should be a better scale as it provides extinction cross section per weight. To be a stronger obscurant, the extinction normalized by mass should be high in the broad spectral range from visible to infrared and it should be characterized by the mass extinction coefficient (MEC), with unit

The content in this chapter is reproduced from Vashista C. de Silva, Piotr Nyga, and Vladimir P. Drachev, "Optimization and photomodification of extremely broadband optical response of plasmonic core-shell obscurants", Published August 26th 2016 in Journal of Colloid and Interface Science,Vol. 484, pp. 116124, with permission from Elsevier.

m^2/g. These airborne particles can obscure some parts of the electromagnetic spectrum by attenuating the transmission of electromagnetic waves through scattering and absorption or each of them individually. The existing obscurants are typically appropriate either for the visible or infrared range not both ranges, which means that one has to use a set of different types of obscurants to cover all, visible, near-IR, mid-IR, and far-IR ranges. There are some different types of obscurants used for the visible spectrum, such as: the hexachloroethane, alkali halide and phosphorus-derived smokes [37, 38, 39, 40, 41, 42].The MEC (see section 3.2.1 for more details) of such smokes in the range of 2-5 m^2/g for visible spectral [39, 40], but it substantially decreases as the wavelength increases [37, 39, 40, 41]. In addition, these smokes are potentially toxic [42]. Having said that, there are non-toxic obscurants. An example of non-toxic visible obscurants are nanometer size titanium dioxide (TiO_2) [40, 43, 44, 45] or silicon dioxide (SiO2) [45] powders. Measured MEC of titanium dioxide reaches about 4 m^2/g [40, 44]. However, their obscuring properties are very limited in infrared, since the scattering strongly decreases as the wavelength increases. For the infrared, graphite and various metals flakes have been experimentally tested as candidates for obscurants. Some of the materials, like brass, are toxic [46] and, some, like graphite based materials are flammable [47]. Calculations show that metallic fibers with few micrometers length and diameter of the order of 50-100 nm could give high MEC in the narrow band in the IR. Silver fibers in isopropanol show MEC of up to 20 m^2/g at 5 μm [48, 49]. Note that these high aspect ratio metal fibers are hardly keeping their properties if suspended in air due to their mechanical instability and sensitivity of the optical response to the geometry of individual fiber and their agglomeration.

It is beneficial for the obscurant applications to have aerosol with high extinction at low mass in a spectral range covering visible, near-mid-far-IR, which would be considered as extremely broadband in this case. Such an extremely broadband response is typical for fractal planar films of Au or Ag [50, 22, 51, 52, 53, 54]. These fractals in solutions or in planar films enable a photoburning of the spectral holes in the visible and near-IR [55, 56] and far-IR [57, 5]. A preset spectral window of transparency is another desirable feature of the obscurants. This topic is going to be covered in more details in chapter 4.

3.2. Results and Discussion

Submicron particles can be simultaneously an aerosol and a good platform for the fractal metal nanostructures. The resonant narrow-band optical response [58, 59, 60, 61] or broadband 0.5-1 μm [62] response of the core-shell particles depends on the shell nanostructure.

Recently it was shown that the extremely broadband extinction (0.5-20 μm) of the metallic fractal nanostructures is caused mainly by the absorption if grown on a sphere, in contrast to the planar fractal films, where the absorption and reflection equally contribute to the extinction [63].

The optimized obscurants made of core-shell submicron particles, each of which is covering this spectral range from the visible to IR. It allows as well for a laser photoburning of holes in the extinction spectra and consequently making windows of transparency in a controlled manner. The photomodification at an IR wavelength makes window of transparency at the longer wavelength side. This topic is explained in more details in chapter 4.

The core-shell nanoparticles have been synthesized using colloidal chemistry and consist of gold fractal nanostructures grown on precipitated calcium carbonate (PCC) microparticles or silica (SiO_2) microspheres. The experiments show that the rich surface of the PCC flakes is the best core for the fractal shells providing the highest mass normalized extinction over the extremely broad spectral range. The mass normalized extinction cross section up to 3 m^2/g has been demonstrated in the broad spectral range from the visible to mid-infrared. The broadband response is a characteristic feature of each core-shell microparticle. It should be emphasized that this broadband response is not due to different types of core-shells, but rather from the same. This is in contrast to, for example nanorods, which can also provide a broadband response, but due to different aspect ratios. Below shows some examples of fabricated core-shell structures.

3.2.1. Extinction Cross-Section

The extinction cross section, C_{ext}, is defined in the equation 26 below as the intensity change in the incident beam under transmission through a single layer of particles.

$$\Delta I = -I_o C_{ext} N_V \Delta l = -I_o C_{ext} N_S \tag{26}$$

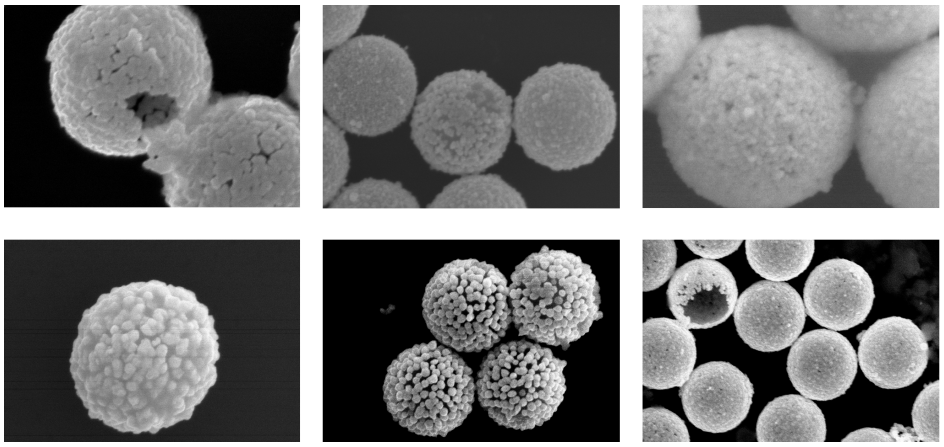

FIGURE 3.1. Fabricated core-shell structures with different metal fractals.

where I_o is the incident intensity, Δl is a hypothetical thickness of a single layer of particles, N_V and N_S are the particle volume density and surface density respectively. Mass normalized extinction is given as:

$$\frac{C_{ext}}{m_p} = -\frac{\Delta I}{I_o N_S m_p} = \frac{1-T}{N_S m_p}[m^2/g] \tag{27}$$

In here the ratio of $\frac{C_{ext}}{m_p}$ is called the MEC, where $m_p = \rho V_p$ (material density times particle volume) is the average mass of a particle. Here, N_S has been estimated from FESEM images: explanation is given under figure 3.2. Average particle mass using known particle density and calculated particle mass. Particle mass was calculated by using known material density and volume of the particle. The second approach is expressed in the equation 28, with the known total mass in the spot, area of the central and edge parts of the spot, and particle coverage at the center and edge of the spot: explanation is given under figure 3.3.

$$\frac{C_{ext}}{m_p} = \frac{1-T}{M}[S_C + S_e\frac{f_e}{f_c}][m^2/g] \tag{28}$$

Total particle mass in the spot, M is calculated following the equation 29, where S_c, S_e and f_c, f_e are respectively surface areas of the center and edge, and fractions of the center and edge.

(29) $$M = \int_0^R M_S(r) 2\pi r dr \approx M_s(center) S_C + M_s(edge) S_e$$

Here M_S is given by the equation 30.

(30) $$N_S m_p = M_s(center) = M[S_C + S_e \frac{f_e}{f_c}]^{-1}$$

Thus one can use two ways to perform the mass normalization after measurements of the transmission spectra T, based on equation 27 or 28. In the first case the particle surface density N_S has to be estimated from FESEM images, and average particle mass must be calculated from known particle density and measured mass density. The second approach (equation 28) implies measurements of the total mass in the spot, area of the central and edge parts of the spot, and particle coverage at the center and at the edge. To deposit a prior known mass in the spot a water or ethanol solution with known mass of particles is prepared. This solution is then deposited in a small volume on a substrate. A very uniform distribution of particles can be obtained on both the ZnSe and glass substrates. The radial dependence and consequently total mass is measured typically out of about 20 images. Below figure 3.3 show as an example how the spot appears and radial dependence.

In order to calculate N_S, I have taken 10-20 FESEM images at low magnification of the sample that has been analyzed. There are two examples shown below. First figure 3.2 shows how the core-shell microspheres made of silica cores are analyzed and second example is shown in figure 3.3 to explain how the PCC's N_S is calculated and what magnifications the FESEM is taken.

In order to show how the area of the central and edge parts of the spot is calculated, I have included an example using above figure 3.3, which shows how the PCC particles are distributed on a substrate. Black color circles separate both the center and edge areas. From this information, one could calculate the surface areas for both center and edge. The surface coverage is calculated by taking multiple FESEM images on both areas and analyzing using a Matlab code [64] which was developed to calculate the high contrast images. This code helped to distinguish between contrasts.

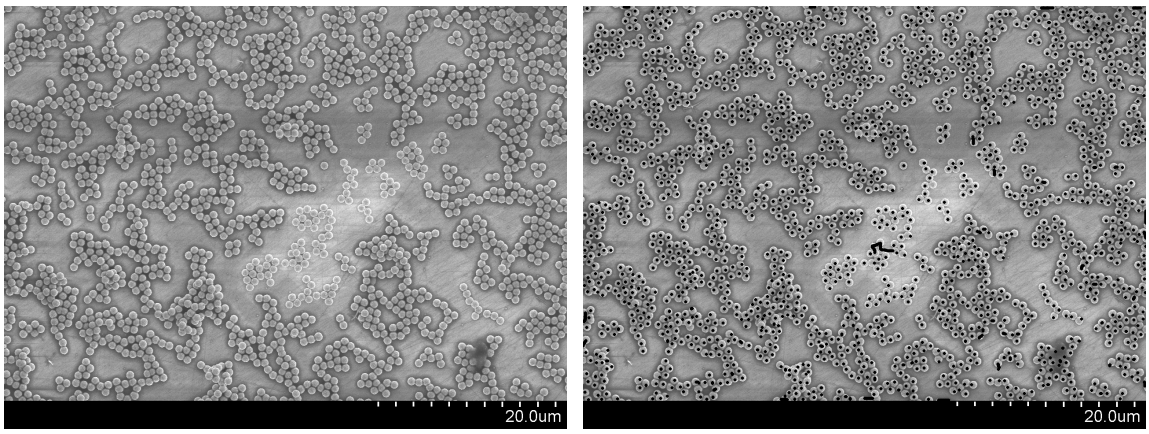

FIGURE 3.2. Number density of silica core- gold shell microspheres using FESEM images.

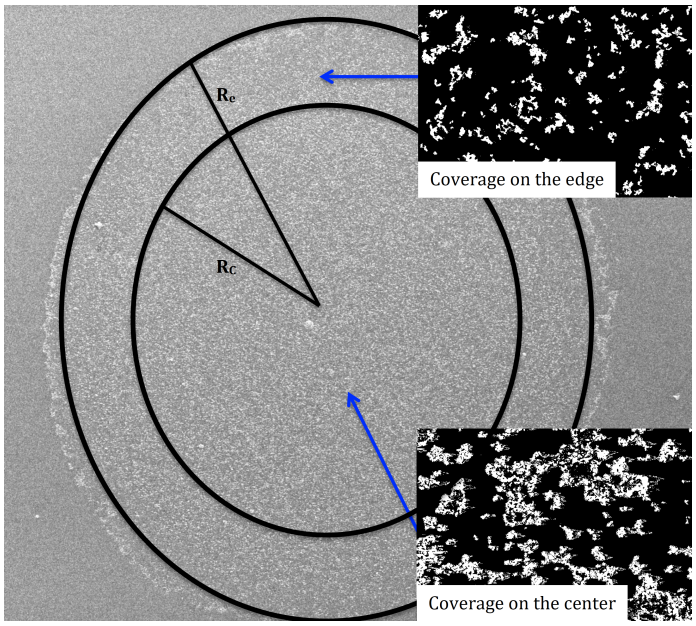

FIGURE 3.3. Number density of PCC microspheres.

It is important to remember that while taking the FESEM images, one needs to acquire them with high contrast otherwise accuracy of the coverage calculations won't be much reliable due to the restriction in above cited Matlab code. Now with this information one could calculate the MEC.

Several different core-shell structures have been studied, all are based on dielectric core and fractal gold shell. The shell optical properties are influenced by the surface plasmon resonances (SPRs). Resonances in a broad spectral range are supported by the localized plasmon modes. A variety of these modes coexists due to fractal geometry of the metal nanostructures

[50, 22, 10, 31]. The extremely broadband spectrum extends from the near ultraviolet to the mid-infrared (0.3 - 20μm). In order to cover the long wavelength side of this range the geometry should allow placement of enough nanoparticles providing long chains supporting the plasmon modes. This requirement is easy to satisfy in case of planar films but does not make obvious the selection of the core diameter or characteristic size. The optimization of mass extinction cross-section was performed experimentally for different diameters of the silica core and complex shape PCC microparticles.

3.2.2. Silica-Gold Core-Shell Microparticles

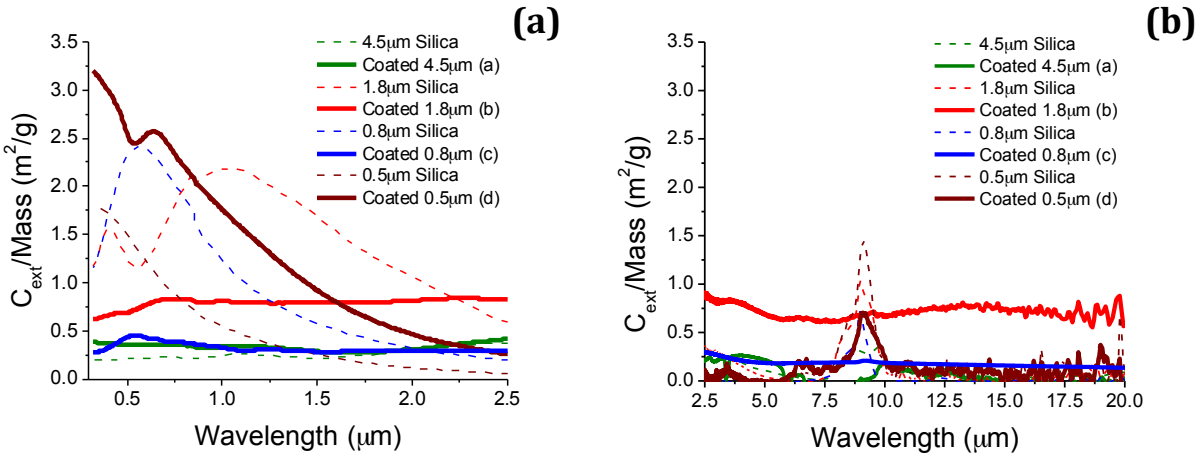

FIGURE 3.4. Mass normalized extinction cross-section spectra in the VIS - near-IR (A) and mid-IR far-IR spectral ranges (B) for the gold coated SiO2 microspheres - solid lines and for the bare SiO_2 microspheres dashed lines (core diameters in μm: 4.5-green, 1.8-red, 0.8-blue, and 0.5-brown).

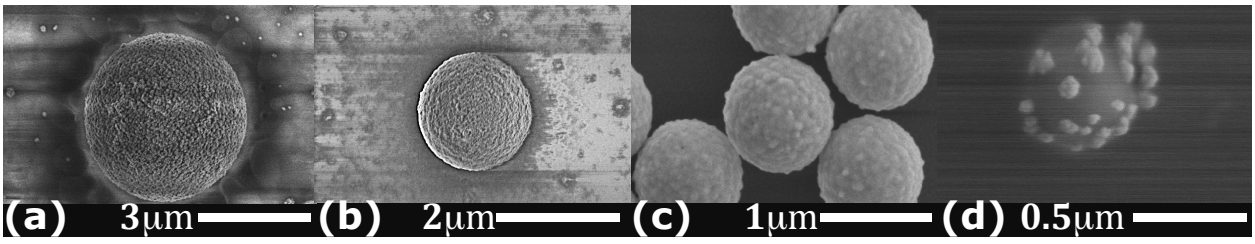

FIGURE 3.5. FESEM images of gold coated SiO_2 microspheres (core diameters in μm: 4.5 (a), 1.8 (b), 0.8 (c), and 0.5 (d)).

A number of silica-gold core-shell structures with different core diameters was synthesized as a first step of optimization. Figure 3.4 shows the mass normalized extinction cross-section

spectra of the core-shell microparticles in the VIS - near-IR (a) and mid-IR far-IR spectral ranges (b).

TABLE 3.1. Calculated experimental parameters of samples shown in figure 3.5 (a-d).

	a	b	c	d
Shell thickness (nm)	89	73	67	70[a]
Total diameter (nm)	4532±74	1860±20	920±10	579±11
Density (μm^{-2})	0.008± 0.001	0.055± 0.01	0.50± 0.02	0.60± 0.06
Shell Mass (g)	$1.0E^{-10}$	$1.4E^{-11}$	$2.3E^{-12}$	$1.2E^{-13}$
Core Mass (g)	$8.7E^{-11}$	$5.3E^{-12}$	$5.0E^{-13}$	$8.2E^{-14}$
Total Mass (g) per microsphere	$1.9E^{-10}$	$1.9E^{-11}$	$2.8E^{-12}$	$2.0E^{-13}$

[a] Gold is synthesized as isolated particles, and each nanoparticle has mean diameter of about 70 nm.Coverage of Au particles on the silica sphere is 0.1. Shell mass of sample (d) is calculated by multiplying shell volume by coverage times gold density. Au density = 19 g/cm^3, SiO_2 density = 2 g/cm^3.

FESEM images of the core-shell nanostructures with different core size are shown in figure 3.5 corresponding to the MEC spectra figure 3.4.

Core-shell structures in figure 3.5 have shell thickness of about 70-90 nm with core diameters ranging from 0.5 μm to 4.5 μm with all the parameters shown in table 3.1. The 0.5 μm silica particles have different uncompleted shells. Isolated Au nanoparticles are randomly distributed on the core surface. The core-shell structures are labeled as per core diameter: 4.5 μm- green, 1.8 μm- red, 0.8 μm- blue, and 0.5 μm- brown. Figure 3.4 shows strong extinction for 0.5 μm sample in the visible and others show broadband extinction from visible to mid-infrared. The small core-shells (0.5 μm) show spectra corresponding to the combined plasmon resonance of the isolated gold nanoparticles and bare silica microsphere. The other three samples show optimum in the MEC for the 1.8 μm core-shells. Qualitatively it can be understood from the following. Indeed, in order to cover a broad band and specifically long wavelength side of the spectrum, the circumference of the surface should allow to place enough nanoparticles providing long chain supporting the plasmon modes. This point makes the larger diameter to be preferable for the broadband response. Some kind of saturation of the response versus diameter can be expected though. Also this could be due to the fact that gold fractals on the shell are not as connected as expected and leads to resonance to die off as spectra extend to mid infrared region. Therefore, one of these could be the reasons why

we don't see strong MEC from 4.5 μm core-shell particles. However, increasing the core-shell diameter tends to increase the mass of the shell and core, which explains the highest MEC for a middle size core-shell.

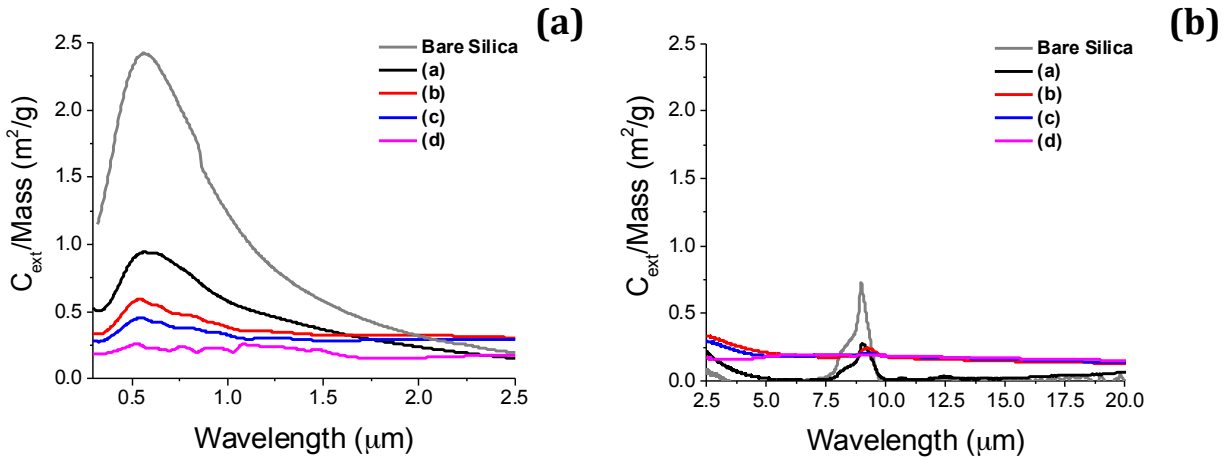

FIGURE 3.6. Mass normalized extinction cross-section spectra in the VIS - near-IR (a) and mid-IR far-IR spectral ranges (b) for gold coated SiO_2 microspheres (core diameter 0.8 μ m with different gold shell coverage).

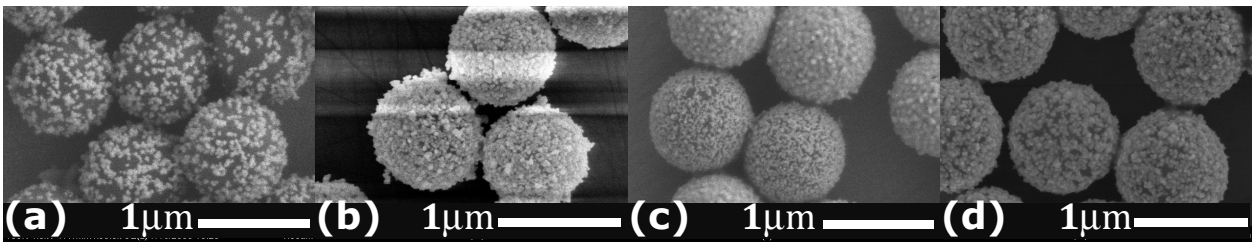

FIGURE 3.7. FESEM images of gold coated SiO_2 microspheres (core diameter 0.8 μ m with different gold shell coverage).

It was studied how the gold coverage changes the properties of MEC. Also, we have included fractal dimension calculations to explain how the core-shell microspheres made of 0.8 μm cores react in the broadband spectrum from 0.4-20 μm.

The gold shells shown in figure 3.7 have fractal nanostructures with fractal dimension D=1.75-1.82. These were calculated using be equation 31 and plotted to find the D using the average slope of the spectra which is shown in figure 3.8 for gold coated SiO_2 microspheres (a)-(d). N, R, and R_o are calculated according to the example shown in the chapter 2 under section 2.5.7 called fractal dimension.

TABLE 3.2. Calculated experimental parameters for Au coated silica with core diameter 0.8μm shown in figure 3.7 (a-d).

	a	b	c	d
Shell thickness (nm)	43	63	67	67
Total diameter (nm)	870±20	910±10	920±10	920±10
Density (μm^{-2})	0.63±0.07	0.66±0.02	0.57±0.02	0.50±0.02
Fractal dimension (D)	1.7655	1.8159	1.7483	1.7448
Shell Mass (g)	$6.80E^{-13}$	$1.30E^{-12}$	$1.60E^{-12}$	$2.30E^{-12}$
Core Mass (g)	$5.05E^{-13}$	$5.05E^{-13}$	$5.05E^{-13}$	$5.05E^{-13}$
Total Mass (g) per microsphere	$1.18E^{-12}$	$1.80E^{-12}$	$2.10E^{-12}$	$2.80E^{-12}$

*Au density = 19 g/cm^3, SiO_2 density = 2 g/cm^3

$$\log(N) = D \times log\frac{R}{R_o} \tag{31}$$

The results in figure 3.6 with corresponding images in figure 3.7 show effect of the different gold coverage on the core-shell performance for silica core diameter 0.8 μm (see all the parameters in table 3.2). Figure 3.6 shows that the mass normalized extinction tends to extend over the visible and infrared ranges with increasing the Au shell coverage. The bare SiO_2 particles show reasonably high extinction in the visible spectral range resulting from scattering which decreases as the spectrum proceeds to the infrared, except at 9 μm due to the vibrational stretching band of SiO_2 [65]. Au fractal film on SiO_2 substantially enhances the extinction of particles in IR spectral range due to the resonant conditions in the Au fractal shell and at the same time the visible extinction stays at reasonable level. With core diameter 0.8 μm we can achieve $\sim$ 0.5 MEC while it shows that $\sim$ 1 m^2/g can be obtained with 1.8 μm microspheres. This is the best mass normalized extinction from visible to infrared spectrum that can be resolved out of 0.5 μm, 0.8 μm, 1.8 μm, and 4.5 μm core-shell spherical microspheres.

3.2.3. Coreless Gold Shell Microspheres

An important aspect of obscuring particles, for their applicability, is their weight. In order to decrease the weight we prepared coreless microspheres. Obviously the coreless shells should

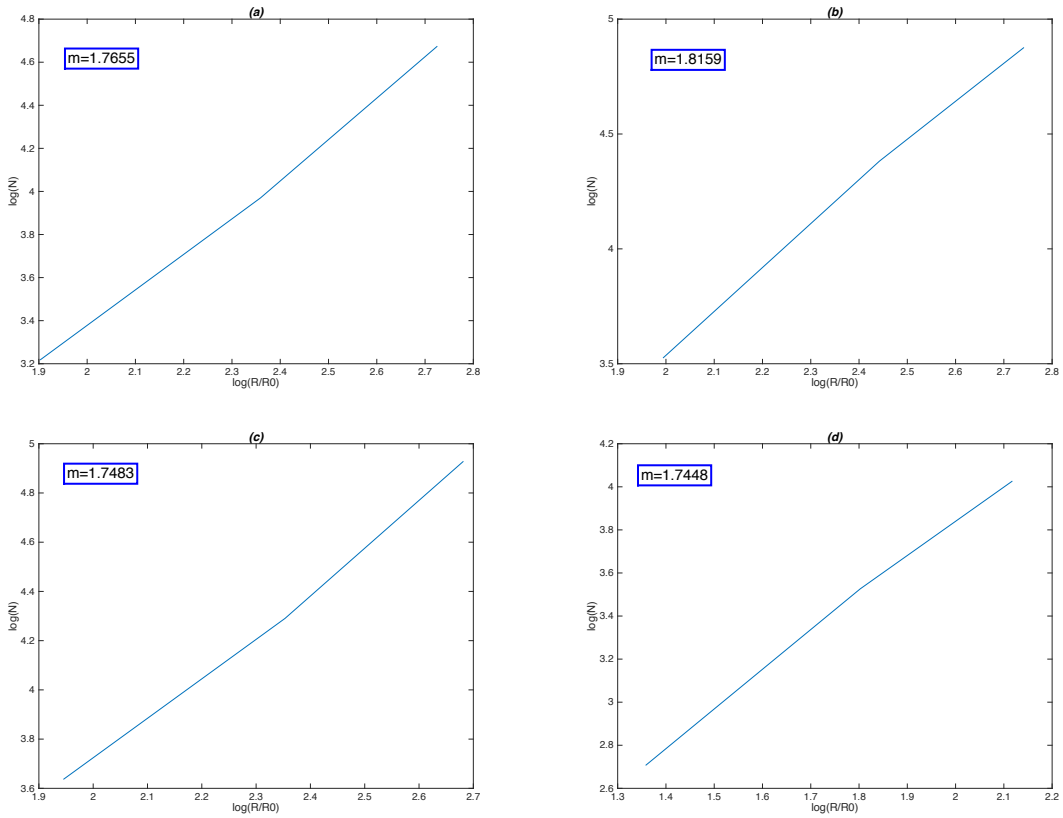

FIGURE 3.8. Fractal Dimension of fractal gold shells on SiO_2 microspheres (core diameters in μm: 4.5 (a), 1.8 (b), 0.8 (c), and 0.5 (d)).

improve the mass normalized extinction if the shell extinction is not affected by the core removal, reduced weight results in higher mass normalized extinction. Coreless structures were made by etching away the silica core in the samples fabricated as described in the methods. A representative Au shell on silica core and coreless Au shell are presented in figures 3.9 (b) and (c), respectively. Through the hole, missing shell part, it is visible that the core-less structure was achieved. The gold shell after core etching preserves its shape and morphology for majority of the structures. It is stable in solution and on a substrate. Of course, it preserves the shape as long as one does not apply any external mechanical force or strain.

The extinction of these coreless particles are normalized per mass is plotted in figure 3.9 (a). MEC is increased in 3.9 (c) as expected when compared to the 3.9 (b) coreshell structure. This increase in MEC confirms that the shell extinction holds after etching. Coreless structures mass ($2E^{-12}$g) is lower as compared to core-shell structure ($2.6E^{-12}$g). The vibrational stretching band

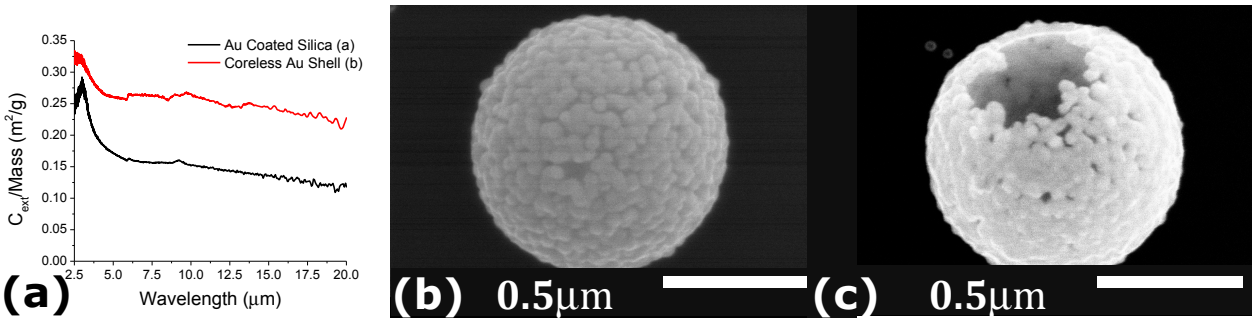

FIGURE 3.9. (a) Mass normalized extinction spectra of gold coated SiO2 and coreless microspheres. FESEM image of the gold coated SiO2 (b) and coreless (c) microspheres (core diameter is about 0.8μm).

of SiO_2 [65] at 9μm which is slightly visible for particles with silica core, and does not appear for the coreless structures.

3.2.4. Gold Fractals on Precipitated Calcium Carbonate

Next we studied Au fractal shells on different core materials. The goal of this part of experiments was to study the effect of the core shape, like flakes on the obscurants performance. In addition, the PCC material has lower density, 0.53 g/cm^3 instead of 2 g/cm^3 for silica. Due to higher refractive index 1.65 [66] and high-opacity [67] the PCC can be a good substrate for the fractal shell. As it was mentioned in section 2.5.4 the synthesis includes one more step to modify the surface with amino groups prior to the Au shell reduction in order to grow the Au fractals. One can see in figure 3.10 that the performances of these structures through the broadband spectral range (0.3-20μm) is very good.

TABLE 3.3. Calculated experimental parameters of PCC samples shown in figure 3.10(a-c).

	a	b	c
PCC particle surface density (μm^{-2})	0.28±0.04	0.16±0.02	0.08±0.01

Average mass core=2.3E-14 g, average mass shell=7.2E-13 g, Mass total per PCC=7.4E-13 g, PCC density=0.53 g/cm^3.

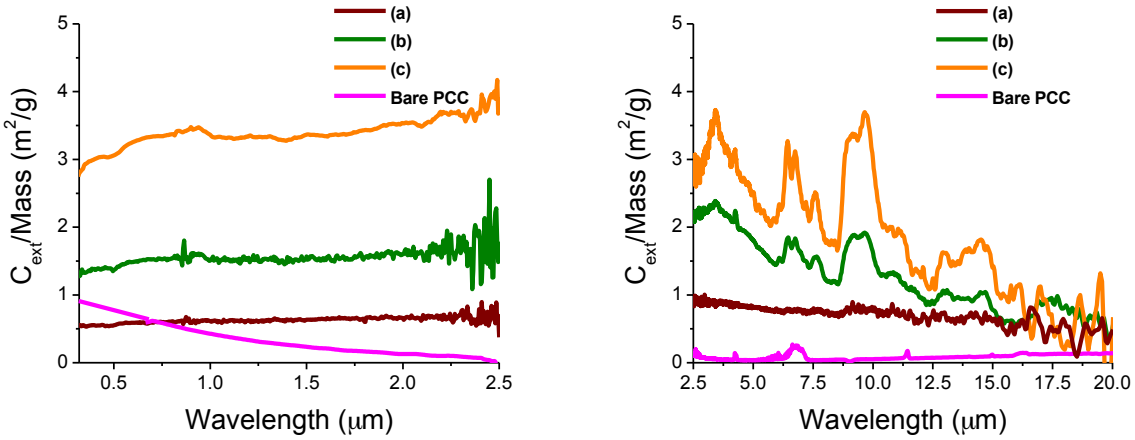

FIGURE 3.10. Mass normalized extinction cross-section spectra in the VIS - near-IR (A) and mid-IR far-IR spectral ranges (B) for gold-coated PCC and bare PCC particles. The reduction time is gradually increased: a) 1.5 hrs, b) 3.5 hrs, and c) 48.5 hrs.

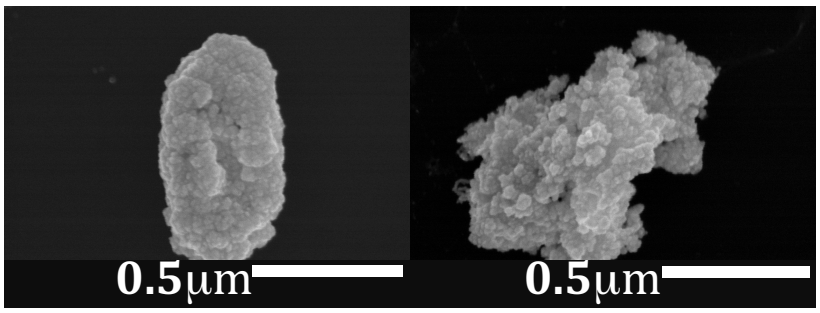

FIGURE 3.11. FESEM images of Au coated PCC of the size 0.7μm and illustrates how the Au structure is formed on PCC.

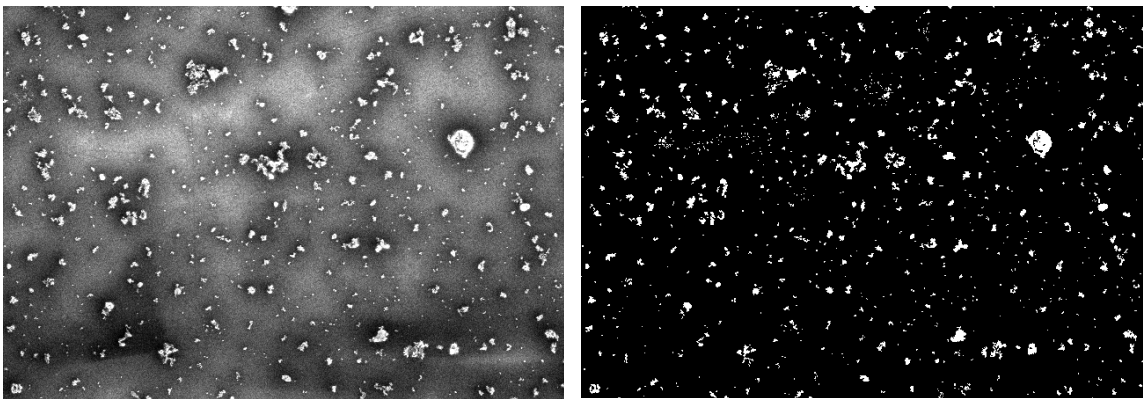

FIGURE 3.12. FESEM images of Au coated PCC on substrate (left) and processed image for number density calculation (right).

In order to perform the mass normalization procedure for the PCC particles, one has to provide uniform deposition of the particles on a substrate. The mass normalization in the PCC

case was a challenge due to significant variation in the shape and size of the bare particles. This was done using image processing tool (MatLab) [64], shown in figure 3.12 where the left figure shows the original FESEM image and right figure after image is processed how the contrast PCC particles were selected. This gives the N_S for the particular sample. Spectra in figure 3.10 show increase in mass normalized extinction cross-section as the gold reduction time increases and consequently the fractal shell becomes more rich and increases in mass. FESEM images in figure 3.11 show sufficient fractal like Au coverage on the randomly shaped and sized PCC. As previously discussed regarding mass normalization, the uniformity and distribution of PCC on the substrate should be significant to satisfy equation 28. Mass of individual PCC particles, calculated using the average size of the particle and its density, is 2.3E^{-14} g (table 3.3). The average size of PCC was measured by analyzing about 50 PCC particles using FESEM images. The spectra of Au-coated PCC particles in figure 3.11 show that the extinction extends over the visible and infrared ranges. The extinction of bare PCC particles shows reasonably high extinction in the visible spectral range due to the strong scattering and decreases as spectra proceeds to infrared. Au fractal film on PCC greatly enhances the extinction in both visible and IR spectral range due to the resonant conditions in the Au fractal shell and scattering of PCC. Note that the increase in the MEC for PCC fractal shells by factor 4.7 in the VIS-mid-IR is due to material density ratio 3.3 and the rest caused by the shape effect.

3.3. Conclusions

We performed experimental optimization of the mass extinction coefficient for plasmonic core-shell obscurants covering the spectral range from the visible to far-IR due to fractal structure of the shell. The shell gold nanoparticles have been synthesized with the colloidal chemistry method and form fractal nanostructures grown on precipitated calcium carbonate microparticles or silica microspheres. Gold was selected as a chemically more stable shell relative to silver. One can see that mass normalized extinction spectra can be increased by carefully changing the chemical synthesis procedures and the core materials. Gradually increasing the mass of fractal shell the optimal of MEC can be achieved in the whole spectral range of interest. Further increase in the metal coverage results in a transition of the fractal shell to a continuous shell with narrow resonance

and increased mass. Among the three samples with silica spherical core of 0.8, 1.8, and 4.5 μm in diameter the optimum in the MEC appeared to be for the 1.8 μm core-shells. Qualitatively it can be explained as a trade of between necessity to provide enough surface area to place enough nanoparticles in the fractal structure to support the plasmon modes at long wavelength range and demand to minimize volume/mass. By etching the silica core the hollow gold shells with good stability and increased mass normalized extinction have been synthesized. The mass normalized extinction cross section of up to 3 m^2/g has been demonstrated in the broad spectral range from the visible to mid-infrared for precipitated calcium carbonate core microparticles. The MEC for PCC is about 4.7 times greater relative to silica, which, in part, is due to the factor 3.3 less material density and the rest is due to the rich PCC microparticle shape. It is important that the broadband response is a characteristic feature of each core-shell microparticle.

CHAPTER 4

PHOTOMODIFICATION

4.1. Background

During the past decade the work on photomodification has focused on the interaction of pulse laser and planar metal films: semi-continuous metal films mostly done for UV to near-IR spectral ranges. It has been established that local structural and polarization dependent changes can be obtained for semi-continuous metal films [68, 69, 70] and fractals based on colloids [71, 55, 70]. The following is a discussion and explanation on how these changes have been achieved through photoburning of local metal-dielectric nanostructures that resonate near the laser wavelength.

The authors [4] have investigated photomodification of semi-continuous silver thin films on glass substrates using the Photo Scanning Tunneling Microscope (PSTM). In their study, they photomodified the silver structures with Nd:YAG (Second harmonic generation) with 5 ns pulses at 532 nm with 9 mJ cm^{-2}. The left part of figure 4.1 shows a PSTM near field image which was probed at 633 nm. It shows nonuniform distribution of laser intensity, though it contains highly localized hot spots. The right part of figure 4.1 shows a PSTM near field image which was photomodified at 532 nm and probed at 633 nm on the same area of the sample. It shows that the left and right images display similar features in addition to some changes in a few locations. The intensity plots for each image shows 40% decrease in the intensity after photomodification for the spot aligning with the cross section between the horizontal line and the black color pointed arrow. The authors [4] suggest that the changes they observed in field intensity distribution are due to the sintering of silver film.

The photomodification study introduced here is a theoretical research done by Genov [5]. In this study, authors have used metal films closer to percolation threshold. An adiabatic illumination mode is used for photomodification where irradiation is a series of pulses with gradually increasing

The content in this chapter is reproduced from Vashista C. de Silva, Piotr Nyga, and Vladimir P. Drachev, "Optimization and photomodification of extremely broadband optical response of plasmonic core-shell obscurants", Published August 26th 2016 in Journal of Colloid and Interface Science,Vol. 484, pp. 116124, with permission from Elsevier.

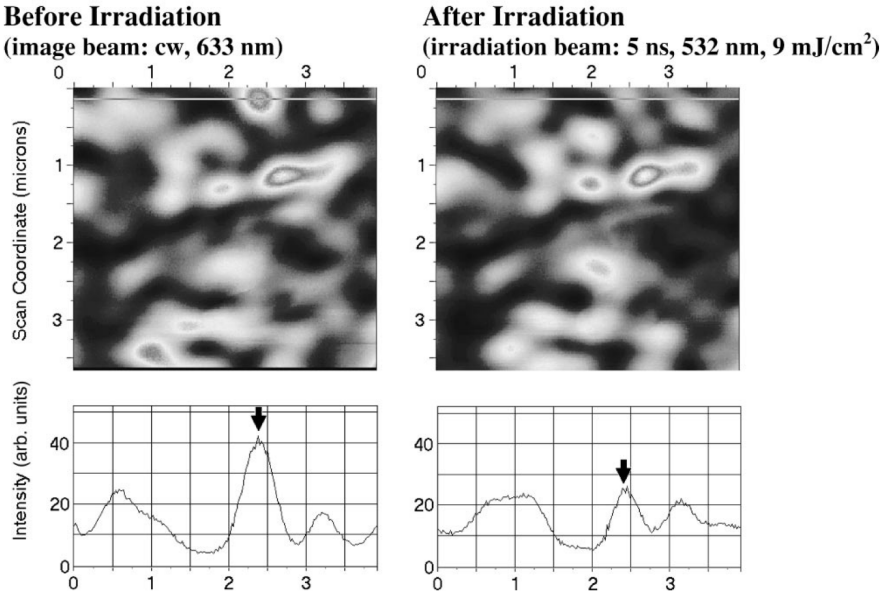

FIGURE 4.1. PSTM images (probe at 633 nm) of semi-continuous silver film on glass substrates before and after photomodification [4].

intensity.

Authors [5] suggest that the optical filters with windows transparency above any preset wavelength could be achieved by using photomodification of the metal structures closer to percolation threshold with highly localized hot spots. During the photomodification, as the authors explain, the adiabatic illumination pulses with increasing intensity only destroy single metal bonds where local field exceeds the threshold value of the intensity. In other words, metal bonds are destroyed when the external force exceeds the threshold value of the metal bond. The mechanism of these changes could be explained as the sintering of metal structure. These changes could results in a decrease in absorption in and around the photomodification wavelength. According to their simulations, the authors carried out the photomodification procedure until the incident laser intensity reaches to a maximum value $I_{0,max}$, which is enough to destroy 0.01% small fraction of the metal fractals giving impressive changes in the spectrum of the metal structure. As mentioned above, restructuring of metal structures happen only for the ones that resonate with the laser wavelength. Therefore, after photomodification most of the metal structures resonate sufficiently and provide good absorption below the photomodified wavelength. Thus, location of the transparency

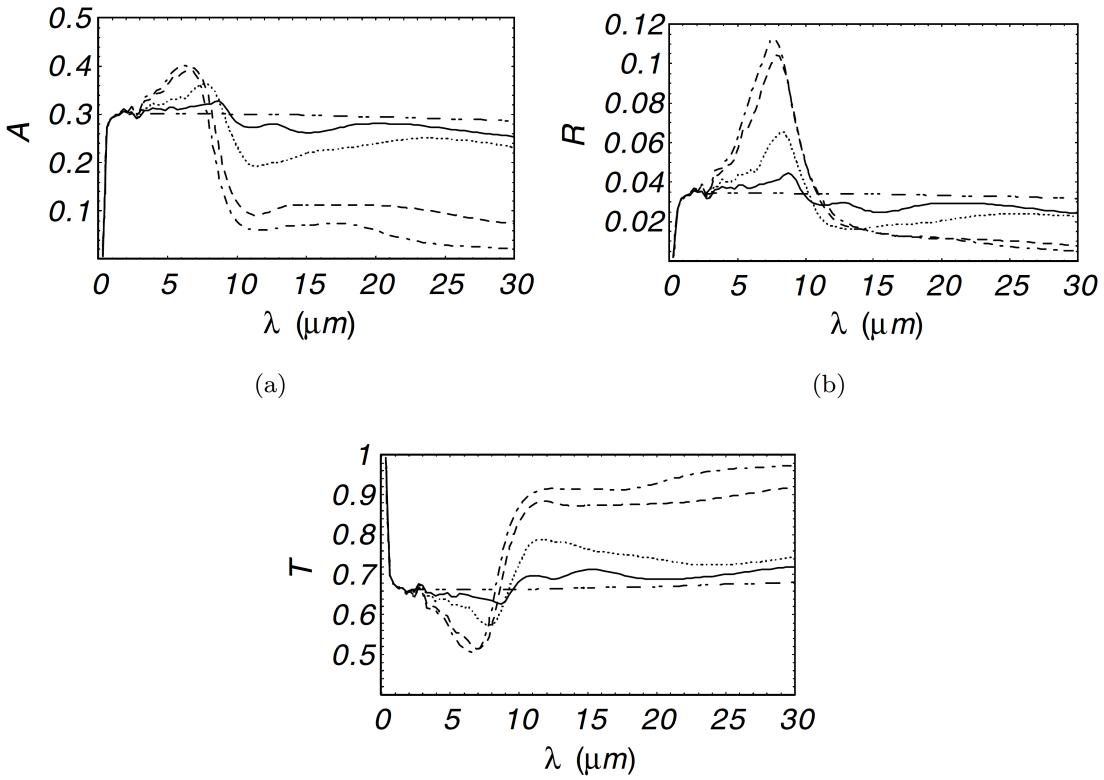

FIGURE 4.2. Analytically calculated absorption **A** (a), reflectance **R** (b), and transmittance **T** (c) spectra of fractal silver structure photomodified with series of light pulses at 10μm with the maximum intensity 0.1 (solid line), 0.2 (doted line), 0.5 (dashed line) and 0.8 (dot-dashed line). Before photomodification spectra are shown as dash double dot lines [5].

window can be controlled by the wavelength of the laser irradiation. Figure 4.2 shows the absorption (**A**), reflectance (**R**), and transmittance (**T**). In these simulations, the authors considered silver metal film at a percolation threshold with adiabatic laser wavelength at 10μm for different laser intensities (four varies maximum intensities). Silver film before photomodification (initial film) is shown as *dash double dot* -·· lines. Figures 4.2 (a), and (c) show that absorption has decreased and transmittance has increased after 10 μm. It is clear that window of transparency is achieved for wavelengths closer to 10 μm and above. Different sizes of silver fractals resonate at their respective wavelengths. Thus the fractal size is directly proportional to particular wavelength. The fractals that are larger in size resonate at longer wavelengths than those with photomodification wavelength, which might have small fractals connected to them that resonate at photomodification

wavelength and could be destroyed. Hence, window of transparency is seen around and above the photomodification wavelength. This also could be explained by looking at the spectra of absorption and reflectance, where there is an increase around the photomodification wavelength. This could be due to the break up of large size fractals that resonate at longer wavelengths and the creation of smaller fractals that supports the photomodification wavelength.

The changes shown in this study are different from those we observed in our previous study which explained fractal aggregates [71, 55, 70] in the visible and near-IR, as windows of transparency only closer to the photomodification wavelength.

Windows of transparency near IR of the optical spectrum are very important for biological photonics devices as biological fluids such as human blood, which has a narrow transmission window near IR of the optical spectrum [72]. As for the biological applications, treatment of cancerous microorganisms is very important. The first observation in 2008 by photomodification of gold nanoshell solution demonstrated that it consists of silica core (140 nm) and gold shell (15 nm). It was done with one pulse at 1 ns pulse, energy density about 4 $mJcm^{-2}$ and with low bubble formation, which is safe for normal tissues other than cancer cells. These nanoshell were photomodified with two different wavelengths with single pulse, at 1064 nm (4 ns) and 900 nm (8 ns) with energy densities ranging from 0.1 $mJcm^{-2}$ to 50 Jcm^{-2}. Blue shifting of the solution was observed by the naked eye, and the absorption spectrum confirmed that absorption goes from 900 nm to 530 nm [73].

4.2. Photomodification of Broadband Response in Infrared of The Fractal Core-Shells

Metal nanoshells are comprised of a dielectric core with a metallic shell. In this experiment, dielectric cores and metallic shells are made of silica and gold respectively. Gold nanoshells are similar to gold colloids and exhibit strong optical extinction due to the strong plasmonic resonance in the metal dielectric configuration [61, 74]. The extinction cross section of gold nanoshells in near infrared is often a few times greater than the nanoshells cross section, which is not seen in the gold colloidal particles even with the comparable core-shell geometries [74, 31]. It is also shown that optical resonance of metal nanoshells can be moved from visible to mid infrared by changing the core diameter and the shell thickness [34]. This tunability is unique compared to just metal

colloidal nanoparticles.

Laser induced changes in structure and optical properties of metallic nanospheres [75], nanorods [76, 77, 78] and core-shell spheres with uniform shells [79, 80] have been extensively studied in UV, VIS and near-IR. However, there were no studies in the mid-IR performed for the fractal core shells with a broadband extinction. The high, broadband extinction core-shell structures studied and can be used as a basis for the development of efficient optical obscurants with preset windows of transparency within a broad spectral range through photomodification of the nanoscale morphology of the fractal metal shell on dielectric core.

A photomodification of the fractal metal shell nanostructure can be accomplished by using a laser pulse light-induced changes due to the coalescence or ablation of the nanostructures. A relatively high-intensity incident pulse can excite resonant responses in the metal nanostructure. If the accumulated energy in a local volume of the resonant mode reaches a threshold value, it can generate sufficient heating to restructure the metal in the area. The structure of the resonant mode is thereby modified, and the modified volume no longer absorbs at the incident laser wavelength. One specific feature, predicted for the IR photomodification for planar films and confirmed in experiments [57, 5] is that the absorption at wavelengths longer than the laser wavelength can be greatly decreased as a result of the photomodification process. Theory work of this study is described in detail in section 4.1. In our study we found similar behaviors for the fractal shells.

The selective photomodification of core-shell extinction was performed for the Au fractal shells formed on silica microspheres. In the experiments, core-shell particles were deposited on ZnSe substrates, which are appropriate for spectroscopic analysis and photomodification experiments in the IR as ZnSe has enough transmission in the near IR to IR. Photomodification was performed using CO_2 laser operating at 10.6 μm generating 50 ns pulses. The photoburning experiment was performed using one pulse photomodification with a linear vertical polarization and the next pulse with orthogonal polarization at the same location in the sample. Thus the cross-polarized photomodification can be performed and then measured by polarization controlled FTIR spectrometer at two orthogonal linear polarizations.

First, in the spectral-burning experiment Au-coated 0.8 μm silica microspheres were pho-

tomodified by a single laser pulse with linear polarization. The pulse energy density ($1/e^2$) was 150 mJcm^{-2}.

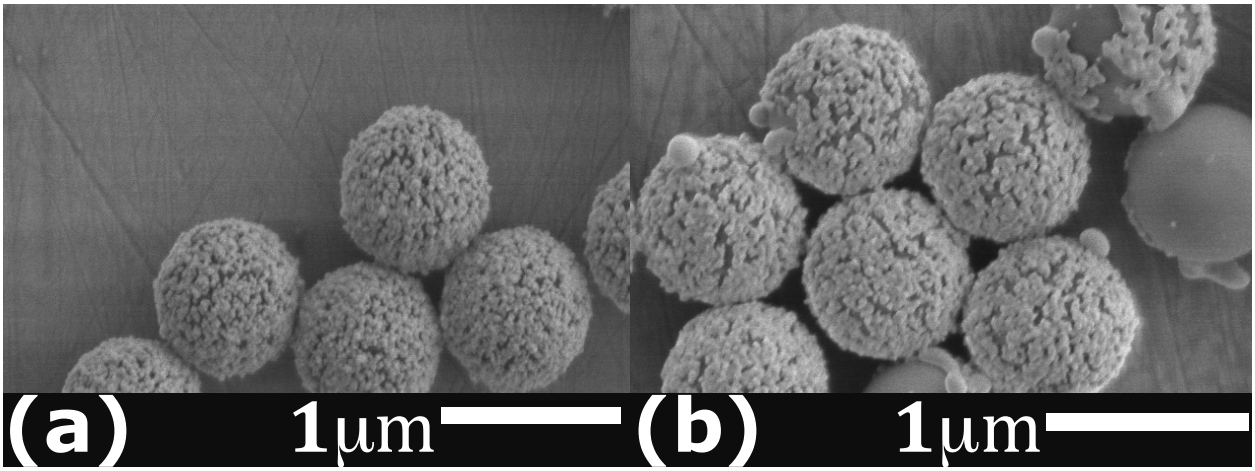

FIGURE 4.3. FESEM images of gold coated SiO_2 microsphere structures. (a) before and (b) after photomodification with CO_2 pulsed laser.

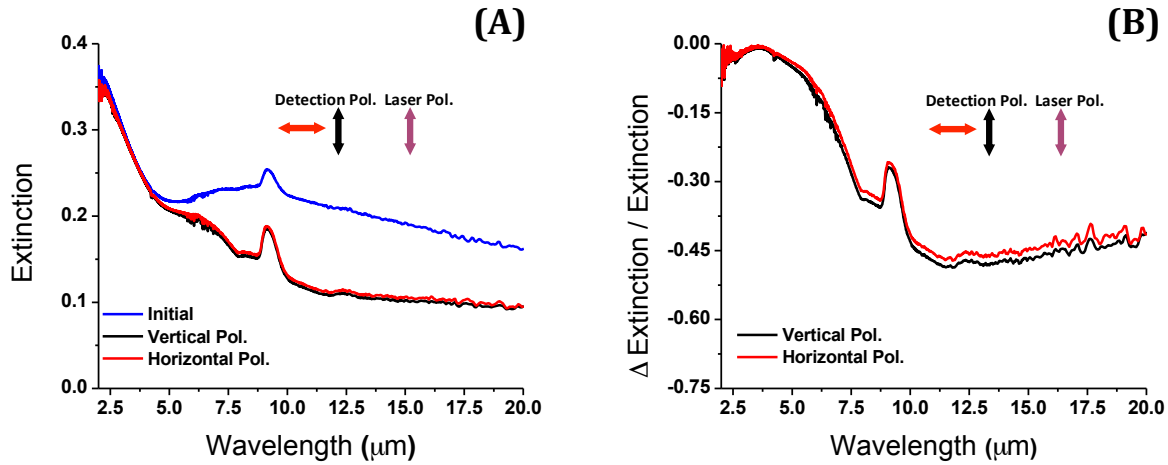

FIGURE 4.4. (**A**) Extinction (normalized per ZnSe substrate) of the gold coated SiO_2 microsphere structures before (blue) and after photomodification with the CO_2 laser operating at 10.6 μm, (black) vertical and (red) horizontal measurement polarizations, and (**B**) relative changes in extinction normalized by initial extinction. The laser wavelength was 10.6 μm and energy density was 150 mJcm^{-2}.

Figure 4.3(b) shows noticeable changes in the structure of core-shells after photomodification as compared to the original structure (figure 4.3 (a)). There are spherical Au particles with 100-150 nm diameter present on the SiO_2 cores, probably due to the coalescence of resonant fractal structures. The spectra in figure 4.4 (A) show the initial extinction of core-shell particles (nor-

malized to ZnSe substrate) and the extinction after photoburning. The photomodification process results in a decrease of the extinction for wavelengths longer than about 4 μm, creating long-pass filters. This effect can be clearly seen in figure 4.4 (B), where relative changes in extinction are presented. The changes in extinction are nearly independent on the probe beam polarization.

Surprisingly, there is no polarization selectivity here even though the spectral selectivity clearly manifests itself, as shown in figure 4.4 (B) for normalized relative changes in the extinction spectra. We see that an incident laser pulse of a certain polarization (vertical in this case) results in almost the same spectral changes for both the vertical and horizontal polarizations of the probe light in the FTIR measurements. The corresponding structural changes of the shells metal nanostructure are different for different particles, as can be seen in figures 4.3 (A) and (B).

Next, photomodification with a second pulse was performed, this time with the orthogonal linear polarization as compared to the first pulse. The same area of sample was illuminated. Thus Au shells were photomodified with cross-polarized pulses. The energy density for this particular photomodification was 150 mJcm^{-2}.

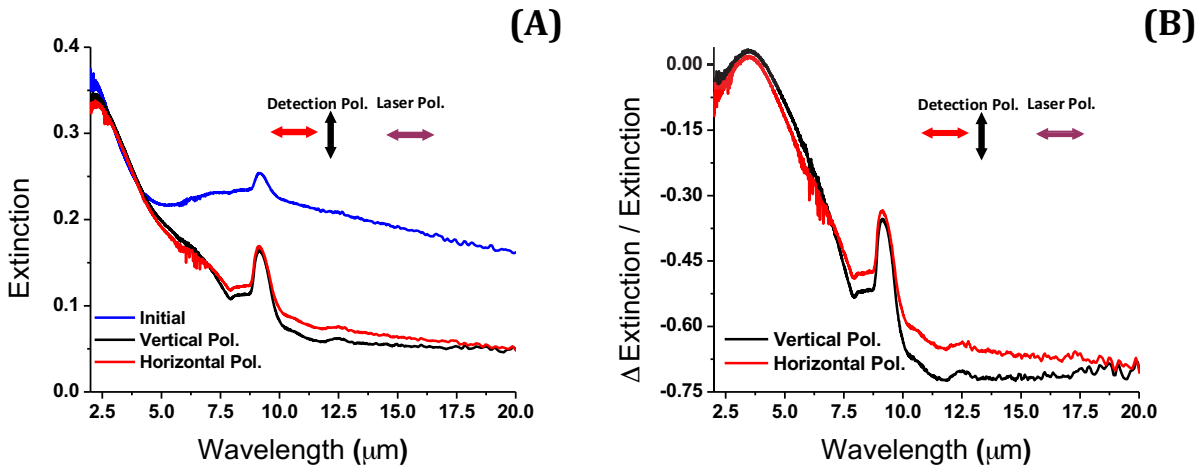

FIGURE 4.5. (**A**)Extinction (normalized per ZnSe substrate) of the gold coated SiO2 microsphere structures before (blue) and after photomodification with the CO_2 laser, (black) vertical and (red) horizontal polarizations, and (**B**) relative changes in extinction normalized by initial extinction. The laser wavelength 10.6 μm and energy density was 150 mJcm^{-2}.

After cross-polarized photomodification the extinction decreases further (figure 4.5 (A)) for wavelengths longer than 4 μm and hardly changes for shorter wavelengths. The relative change

in extinction saturates for the wavelengths longer than the laser wavelength (figure 4.5 (B)). The observed decrease in extinction is stronger than that for the single pulse photomodification as presented in figure 4.4. Also there is a polarization dependence of the resulting extinction for the probe light.

It is important to emphasize the following points concerning the polarization dependences:

(a) Before the photomodification, the spectra collected with two orthogonal polarizations are the same since, indeed, there is no any preferable direction in average.

(b) However, the linear polarization of the laser light used for photoburning can potentially introduce the anisotropy. Surprisingly there is only a minor difference for the spectra at two orthogonal polarizations of probe. This observation is in contrast to the polarization selectivity of photomodification experiments at the visible or near infrared ranges [55, 56]. The experiments with the planar films photomodification [57] show much worse selectivity in the mid-IR relative to the Vis /near IR. This fact indicates a larger overlap for the linear polarized plasmon modes at the longer wavelength.

(c) The experiments in this work were done with the fractal shells on spherical microspheres, which makes polarization selectivity negligible relative to the planar films due to variation in the angle of incidence on the spherical surface.

(d) A slightly more pronounced difference appeared after the second pulse, where polarization is orthogonal to the first one. The second pulse with orthogonal polarization does not rebuild the symmetry since the two modes for two polarizations are not independent. Since the process of cross-polarization photoburning is done in series, the next step is dependent on the changes made by the previous pulse, and then a difference in the probe spectra for orthogonal polarizations can be expected.

(e) Nevertheless, we should mention that two pulses with orthogonal polarizations make better filter contrast than two pulses of the same polarization. The cross polarization photomodification resulted in more than three times decrease of the core-shells extinction for wavelengths longer than 10.6 μm. Note the importance of the cross-polarized pulses.

Indeed, a second pulse of the same polarization does not improve the contrast of the extinction spectra. Thus it is possible to perform spectrally selective photoburning of absorption of fabricated airborne obscurants. The extinction of spectral selectivity and contrast ratio of core-shell structures are comparable to those obtained for planar fractal silver films photomodified with nanosecond CO_2 laser pulses with energy density of the same order [57] and those theoretically predicted [5].

4.3. Conclusions

The spectral photoburning of resonant areas in the gold fractal shells with CO_2 nanosecond laser resulted in the spectrally selective modification of their extinction. The photomodification resulted in localized and non-uniform changes of gold fractal nanostructures. This led to the formation of obscurants with a window of transparency in the longer wavelength part of the infrared.

CHAPTER 5

INVISIBILITY

5.1. Introduction

Light scattering by core-shell particles made of dielectric and metal manifests in a variety of phenomena which were predicted many decades ago [58, 59, 60]. The scattering suppression for coated confocal ellipsoids was introduced by Aden and Kerker [58, 59, 60] in the approximation of long wavelength planar electromagnetic waves. The authors called this scattering suppression 'invisibility'. In the core-shell spheres, total sizes could be up to one fifth of the wavelength while still achieving sensible invisibility for planar electromagnetic waves [81, 82]. In this case, the wave can penetrate through the shell and the effect is associated with the out-of-phase scattering properties of plasmonic materials and the dielectric core. By varying the relative dimensions of the dielectric core and high quality continuous metal shell, the sharp optical resonances of these nanoparticles can be varied over hundreds of nanometers in wavelength, across the visible and into the infrared region of the spectrum [61, 83]. In contrast, semicontinuous shells provide broadband response similar to the planar semicontinuous films, as it was shown for the visible spectral range [84, 85, 62]. The optical properties of the metal-dielectric semicontinuous films are influenced by multiple surface plasmon resonances (SPRs) in metal nanostructures, accumulating and building up electromagnetic energy in a broad spectral range at the nanometer scale [21, 86, 51, 87, 52, 88, 89, 10, 5, 57, 53, 54]. A universal phenomenon in the localization of optical energy in inhomogeneous plasmonic media is the formation of hot spots, spatially fluctuating field with spikes in nanometer-size regions determined by the minimum scale of the nanoplasmonic system [87, 52]. The picture of nanolocalization of the optical energy in disordered clusters is called inhomogeneous localization [88, 89] assuming that there are different plasmonic eigenmodes, which coexist at close frequencies and have completely different localization sizes, ranging

The content in this chapter is reproduced from Vashista C. de Silva, Piotr Nyga, and Vladimir P. Drachev, "Scattering suppression in epsilon-near-zero plasmonic fractal shells", Published October 12th 2015 in Optical Materials Express,Vol. 5, No. 11, pp. 24912500, with permission from OSA.

from the minimum scale to the scale of the entire systems. Each eigenmode may consist of a different number of sharp hot spots. Note that such type of disordered geometry has typically fractal dimensions [86, 51]. As it is known for the planar fractal films, the critical value of the metal coverage, called percolation threshold [21], results in a variety of plasmon resonances covering a spectral range from the visible to infrared. Thus the fractal films being synthesized on the microspheres can be promising aerosolized obscurants in the extremely broad visible-infrared spectral range.

Here we study silica-gold core-shell microspheres with plasmonic fractal shells. The similarities and differences with the planar noble metal fractal films have been experimentally established, though not addressed in the earlier publications [84, 85, 62]. We show that the forward scattering of the silica microspheres is strongly suppressed, and the reflection of the fractal shells does not grow with coverage approaching the percolation threshold. This is in contrast to the planar fractal films, where the forward scattering decreases and backscattering increases as the metal coverage increases. An even less intuitive result is that the total extinction of the core-shell is decreased relative to the bare core response. The system is simulated using Mie theory with Aden and Kerker extension [58]. The fractal shell parameters are calculated with the Bruggeman effective medium theory (EMT) [90]. We discuss the EMT results and its applicability using the scaling theory approach [86, 51]. The model provides a reasonable agreement with experiments in the broad spectral range, from 400 nm to 20 μm, covering shorter and longer wavelengths relative to the microsphere size. Both experiments and simulations show that a fractal shell with metal filling factor close to 0.5 enables scattering suppression in the visible range along with the increase in total transmission at the wavelength of Mie scattering peak at about 560 nm. The results indicate that this suppression is not just a spectral shift of the resonance in scattering, but suppression of its amplitude without noticeable shift. In the infrared range the gold semicontinuous shell hides the absorption resonance of the silica sphere at 9 μm . The effective permittivity for our samples is shown to be epsilon-near-zero for the real part $\varepsilon^{'}$. The imaginary epsilon multiplied by the frequency $\omega\varepsilon^{"}$ approximately does not depend on the wavelength across the broad spectral range 0.5-20 μm .

5.2. Results and Discussion

In the experiments, silica microspheres with a diameter of about 780 nm were coated with gold nanostructures using a modified method of the reduction of gold salt, which is described in section 2.5.2. This method was initially developed for continuous shells [33], and the synthesis procedure was modified in order to fabricate fractal shells. The synthesized gold-coated microspheres were deposited on zinc selenide (ZnSe) substrates for the infrared spectroscopy and on fused silica substrates for spectroscopy in the visible range [91].

Several different samples have been synthesized to study the effect of the shell structures with gradually increasing gold coverage (p). The spectra for normalized extinction (NE) are presented in figure 5.1. The normalized transmittance (NT) spectra were first normalized by the transmittance of the bare substrate. Since the density of microspheres on the substrate was slightly different for each sample, the extinction was normalized according to the density. The normalized extinction spectra were calculated as NE=$\frac{-log(NT)}{N_S}$, where N_S is the core-shell microsphere surface density calculated from the field emission scanning electron microscopy (FESEM) images and taken in μm^2, and is presented in table 5.1. FESEM images of different shell structures corresponding to the normalized extinction spectra are presented in figure 5.2. The samples are labeled from 0 to 4, where 0 corresponds to the sample of bare silica microspheres ($p_0 = 0$) and 1-4 correspond to the samples with gradually increasing gold coverage in the shells, namely $p_1 = 0.38 \pm 0.03$, $p_2 = 0.47 \pm 0.01$, $p_3 = 0.58 \pm 0.03$, and $p_4 = 0.85 \pm 0.02$. Note that the FESEM images allow us to measure only 2D projection of the structure and the gold coverage is calculated for such a plane view. This is a reasonable approximation of the resultant filling fraction of metal (f), which we use in the simulations for less dense shells. The samples 3 and 4 can be clearly seen as having 3D structure, and thus the filling fraction can be less than that estimated from the plane coverage. The shells have the fractal structure with fractal dimension D = 1.75-1.82 (see table 5.1). It was calculated (see section 2.5.7) as the power dependence of the number of gold nanoparticles Np inside the circle of radius R, $\frac{N_p}{N_0} = (\frac{R}{R_0})^D$ [86]. For the bare silica microspheres there is an absorption peak due to the Si-O-Si vibrational stretching band at 9 μm [65] and there is an extinction peak in the visible spectral range due to the Mie scattering resonance at 560 nm (see figure 5.1 for

p = 0).

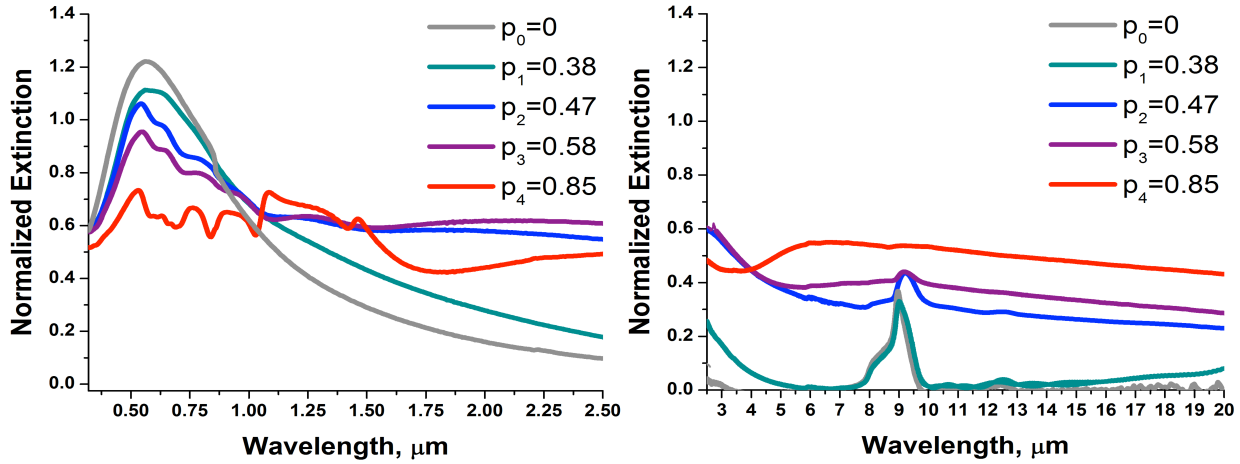

FIGURE 5.1. Normalized extinction spectra of the core-shell particles with different gold shell coverage and morphologies shown in figure 5.2.

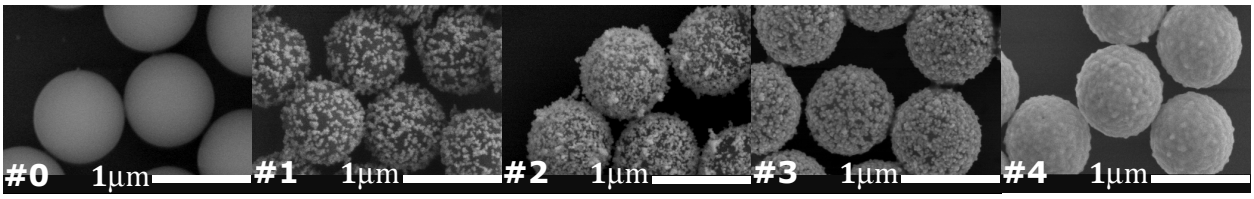

FIGURE 5.2. FESEM images of the core-shell particles with different gold shell coverage and morphologies.

The spectra in figure 5.1 show strong dependence on the shell structure. The extinction spectra become broadband and spread out from the visible to infrared as the coverage increases. Note that this feature looks similar to the planar semicontinuous films, where the broadening of extinction spectra has been theoretically and experimentally demonstrated near the percolation threshold [86, 51, 87, 52, 88, 89, 10, 5, 57, 53, 54]. The critical feature of the semicontinuous films is the enhanced absorption at the range of the surface coverage, measured as the relative deviation from the percolation $\delta p = \frac{(p-p_c)}{p_c}$, between 0.2 and 0.2, where p_c = 0.68 [86]. The shell structure of the sample **1** is composed mainly of small Au fractals, most of which are isolated. The deviation δp_1 = -0.44 and, consequently, the extinction increases little for longer wavelengths, similar to the planar films. As soon as the relative deviation δp reaches the critical range, as for sample **3**, the extinction increases in the near- and mid-infrared regions. The extinction increases for both

below and above the Si-O-Si vibration band for this shell structure. The extinction of bare SiO_2 spheres at the position of the Si-O-Si vibration band is caused mainly by the absorption in silica, and scattering does not have a major effect [65]. By keeping the shell thickness relatively constant and increasing the metal filling fraction from sample **2** to sample **4**, the extinction is gradually increased. Figure 5.1 shows that broadening occurs for samples **2**-**4**. Surprisingly, it completely hides the absorption of the silica vibration band at 9 μm. Note that since silica microspheres have very low absorption in the visible, the extinction from bare silica particles is purely due to the scattering. As the gold coverage of the shell structure increases, creating gold fractals, the extinction decreases. The scattering peak at 560 nm is suppressed and substituted by absorption in the shell at the lower level, so that the total transmission is increased. Indeed the absorption in the visible range is almost independent of the wavelength. It allows us to estimate the magnitude of the absorption at 560 nm and confirms that scattering is significantly suppressed.

Detailed measurements with the integrating sphere allow us to determine contributions of both scattering and absorption. The core-shell optical studies are typically limited to the extinction; however, the scattering measurements give important details of the core-shell optics. The transmittance (T), specular reflectance (R), and forward- (FS) and back-scattering (BS) spectra were collected for bare silica and gold-coated silica microspheres, i.e. sample 0 with p = 0 and sample **4** with p = 0.85. The spectra were collected with the integrating sphere accessory [91]. The transmittance was measured along the optical axis of the integrating sphere; forward scattering occurred in the forward semi-sphere and excluded light transmitted along the axis; the specular reflectance was measured as the reflected light with incidence angle of 8 degrees; backscattering occurred in the backward semi sphere and excludes specular reflection. All the spectra are normalized per particle surface density (N_S), 0.4 μm for bare microspheres and 0.5 μm^{-2} for core-shell sample **4**. The results are plotted in figure 5.3 for cross sections of the corresponding processes. For a single layer of microspheres, the attenuation of transmitted light intensity is $\Delta I = -I_0 C_{ext} N_s$, where I_0 is the input light intensity, C_{ext} is the microparticle extinction cross section and N_s is the particle surface density. Thus $C_{ext} N_s = 1 - T$, $C_{FS} = \frac{FS}{N_s}$, $C_{BS} = \frac{BS}{N_s}$, and $C_R = \frac{R}{N_s}$, where C_{ext}, C_{FS}, C_{BS}, and C_R are the extinction, forward-scattering, back-scattering, and specular reflection cross sec-

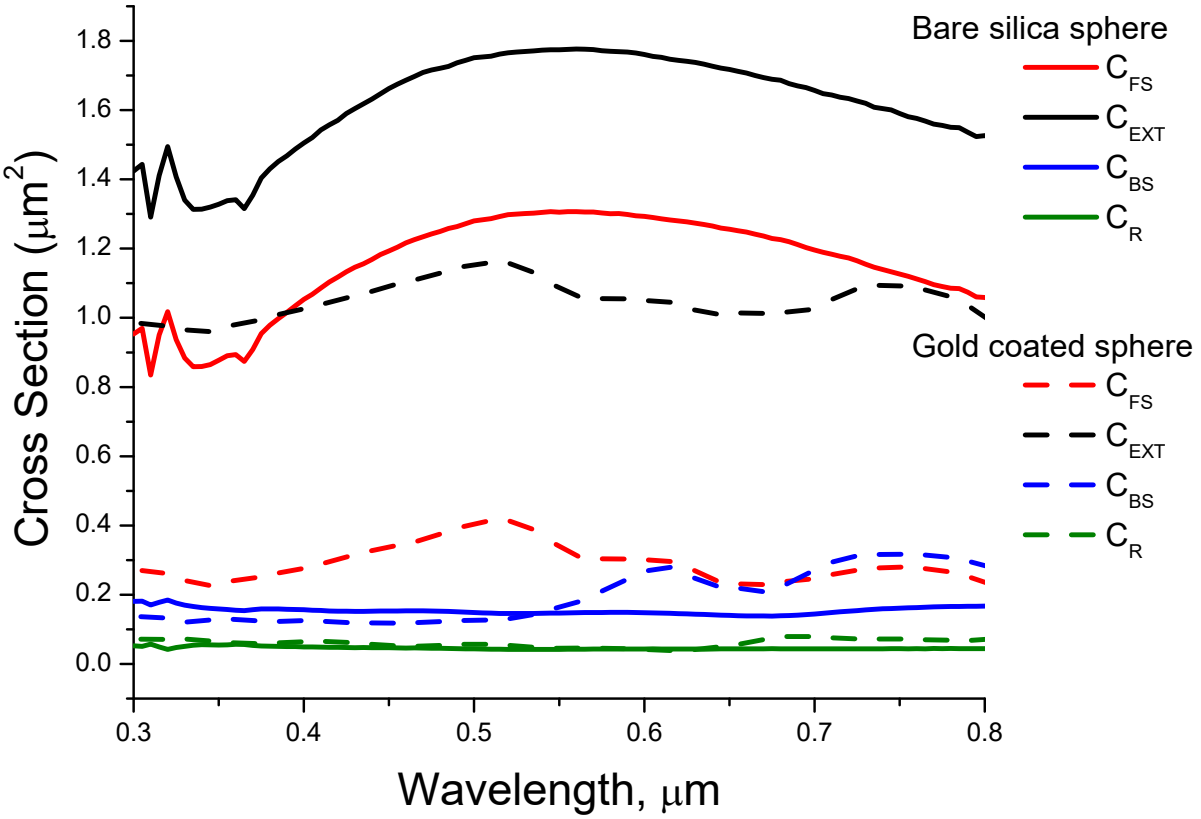

FIGURE 5.3. Measured cross sections, C_{FS}, C, C_{BS}, and C spectra of a submonolayer of bare silica microspheres **0** (solid lines) and gold-coated silica microspheres **4** (dashed lines).

tions, respectively. The extinction cross section (black dashed line in figure 5.3) of the gold-coated sphere has decreased as compared to the bare silica microsphere (black solid line) near the Mie resonances. Also, the forward scattering of the gold-coated spheres (red dashed line) is suppressed on average by about 75% compared to the bare silica microspheres (red solid line). The reflectance and backscattering for the gold-coated microspheres have not increased significantly compared to the bare silica microspheres.

In order to explore the effect of scattering cancellation in the effective medium approximation, numerical simulations have been performed and presented in figure 5.4 for the visible range and infrared range. To calculate the extinction cross section C_{ext} of gold coated silica core-shell

TABLE 5.1. Experimental (EXP) and simulations (SIM) parameters.

	Sample #0	Sample #1	Sample #2	Sample #3	Sample #4
Shell thickness (nm), EXP[a]	0	43	63	67	67
Total diameter (nm), EXP	d=785±3	d=870±20	d=910±10	d=920±10	d=920±10
Total diameter (nm), SIM[b]	800	880	900	920	920
Plane metal surface coverage (p), EXP	0	0.38±0.03	0.47±0.01	0.58±0.03	0.85±0.02
Metal volume filling fraction (f), SIM	0	0.4	0.48	0.5	0.505
Microsphere density number on a substrate (μm^2), EXP	0.4±0.02	0.63±0.07	0.66±0.02	0.57±0.02	0.5±0.02
Effective n_{surr}[c], SIM					
VIS[d]	1	1.2	1.2	1.3	1.4
IR[e]	2.4	2.4	2.4	2.4	2.4
T[f] @ 560 nm, EXP	29%				47%
C_{FS}[g] @ 560 nm (μm^2), EXP	1.3				0.3
Fractal dimension (D), EXP		1.77	1.82	1.75	1.75

[a]EXP=Experimental values

[b]EXP=Simulation values

[c]n_{surr}=Refractive index of surrounding media

[d]VIS=SiO_2 substrate, PVP thin coating, and air

[e]IR=ZnSe substrate, PVP thin coating, and air

[f]T=Transmission

[g]C_{FS}=Foward scattering cross section

particles, the Mie theory based algorithm described elsewhere [2] was used, and the particle was modeled as a concentric system with a silica core of radius r_1 (400 nm) and gold shell with thickness t_1 and total radius $r_2 = r_1 + t_1$. The silica wavelength dependent dielectric constant was taken from [92, 93]. The effective permittivity ε_{br} of the gold shell in form of semicontinuous film with different metal fraction f was calculated using the Bruggeman effective medium approximation [90]:

$$f\frac{\varepsilon_m - \varepsilon_{br}}{\varepsilon_m + 2\varepsilon_{br}} + (1-f)\frac{\varepsilon_h - \varepsilon_{br}}{\varepsilon_h + 2\varepsilon_{br}} = 0 \tag{32}$$

where ε_h is the permittivity of host or surrounding medium and ε_m stands for the Drude-Lorentz model for the gold dielectric constant [94]. The filling factor f ranges from 0 to 1, where 0

corresponds to the case without a shell and 1 to a continuous gold film. The Drude-Lorentz model includes contributions from free electrons and interband transitions:

$$\varepsilon_m = 1 - \frac{\omega_p^2}{\omega^2 + i\alpha\Gamma_p\omega} + \sum_n \frac{g_n\omega_n^2}{\omega_n^2 - \omega^2 - i\alpha\Gamma_n\omega} \tag{33}$$

To match the Johnson and Christy (J&C) experimental data [94], the equation with Drude parameters ω_p= 9 eV, Γ_p=0.07 eV [94] and two Lorentzian oscillators with parameters as follows were used: g_1= 0.3, ω_1= 2.7 eV, Γ_1= 0.3 eV,g_2= 0.8, ω_2= 3.05 eV, Γ_2= 0.5 eV [95].The loss factor α is used to modify the gold damping term (Γ_p) to introduce the difference between J&Cs bulk gold dielectric constant and the dielectric constant of the nanostructured gold. The possible range of the loss factor reported in the literature is from 0.5 for bulk gold [3] and up to 4 for e-beam lithography fabricated nanoparticles [95]. It is known that chemically synthesized nanoparticles have better crystal quality than continuous thin films, where the grain boundaries contribute to the electron relaxation. This justifies the selection of the loss factor for isolated nanoparticles in the shell to be 0.5-1.

Note that using the Theye formula for the electron relaxation constant Γ=τ^{-1}+$b_\tau\omega^2$ has been avoided, which is quite popular in the literature on fractal metal films with the parameters involved as fitting in the ranges τ_0=(0.2-3)E^{-15}s, b_τ=(0.5-3.5)E^{-16}s [62, 51]. Indeed, such frequency dependence was introduced initially for the electron-electron collisions V_{ee}. A careful study of the temperature dependence of the electron relaxation constant by Motulevich proves that V_{ee} could only be observed at helium temperatures for metals and spectral ranges, where the interband transitions are negligible [96]. Moreover, the assumption of the frequency dependence for the relaxation constant will require frequency dependence of the electron density as well [96], an unexpected result. This is explained in detailed in section 2.3.2. The extinction cross section is given by:

$$C_{ext} = \frac{2\pi}{k^2}\sum_{m=1}^{\infty}(2m+1)Re(a_m + b_m) \tag{34}$$

where k=$\frac{2\pi}{\lambda}$ is the wave vector, λ is the wavelength in the ambient medium, and a_m and b_m

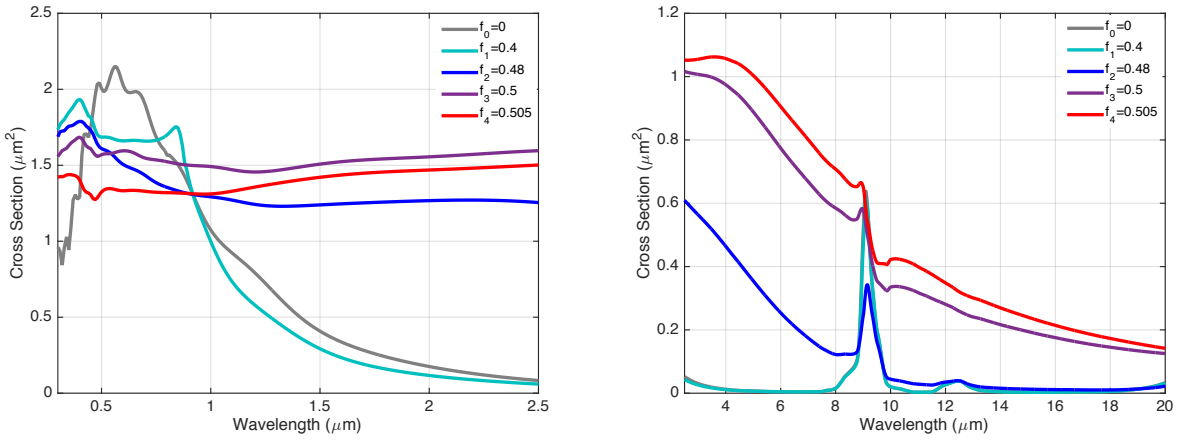

FIGURE 5.4. Extinction cross-section spectra for different metal filling fraction, f (0, 0.4, 0.48, 0.5, and 0.505) simulated for the visible-near IR and IR spectral range.

are the scattering coefficients of electrical field. The coefficients a_m and b_m were calculated using an algorithm described by Wu et al [3]. The sum runs for values of m from 1 to ∞, but the series can be truncated at some maximum m_{max} (m_{max}= kr_2) [2]. To closer resemble the experimental conditions in IR spectral range (ZnSe substrate), we used n = 2.4 for the refractive index of the surrounding medium.

There are three parameters which are either not known or known with little certainty from the experiment. As we mentioned above, the plane gold surface coverage *p* is measured accurately from the SEM images, but it should be considered generally as a volume fraction and could be overestimated due to this 3D effect. The shell thickness is measured using the physical boundary of the metal edge, so that the thickness used for the effective permittivity can be decreased. The effective refractive index of the surrounding medium is estimated as an effective parameter by combining contributions of the substrate, PVP coating, and air. It can be coverage dependent and vary from 1.1 to 1.5 for the glass substrate, and 1.4 to 2.4 for ZnSe substrate. Thus, we use a slight variation of these parameters shown in the table 5.1 for best fit of the experimental results.

With the EMT model, the simulated optical spectra (figure 5.4) show quite good correspondence to the experimental spectra (figure 5.1). Interestingly, the effective permittivity of the shells close to the percolation threshold calculated with equation 32 shows near zero behavior (figure 5.5) of the real part in the broad spectral range, and the product $\omega\varepsilon$" is weakly dependent (or even

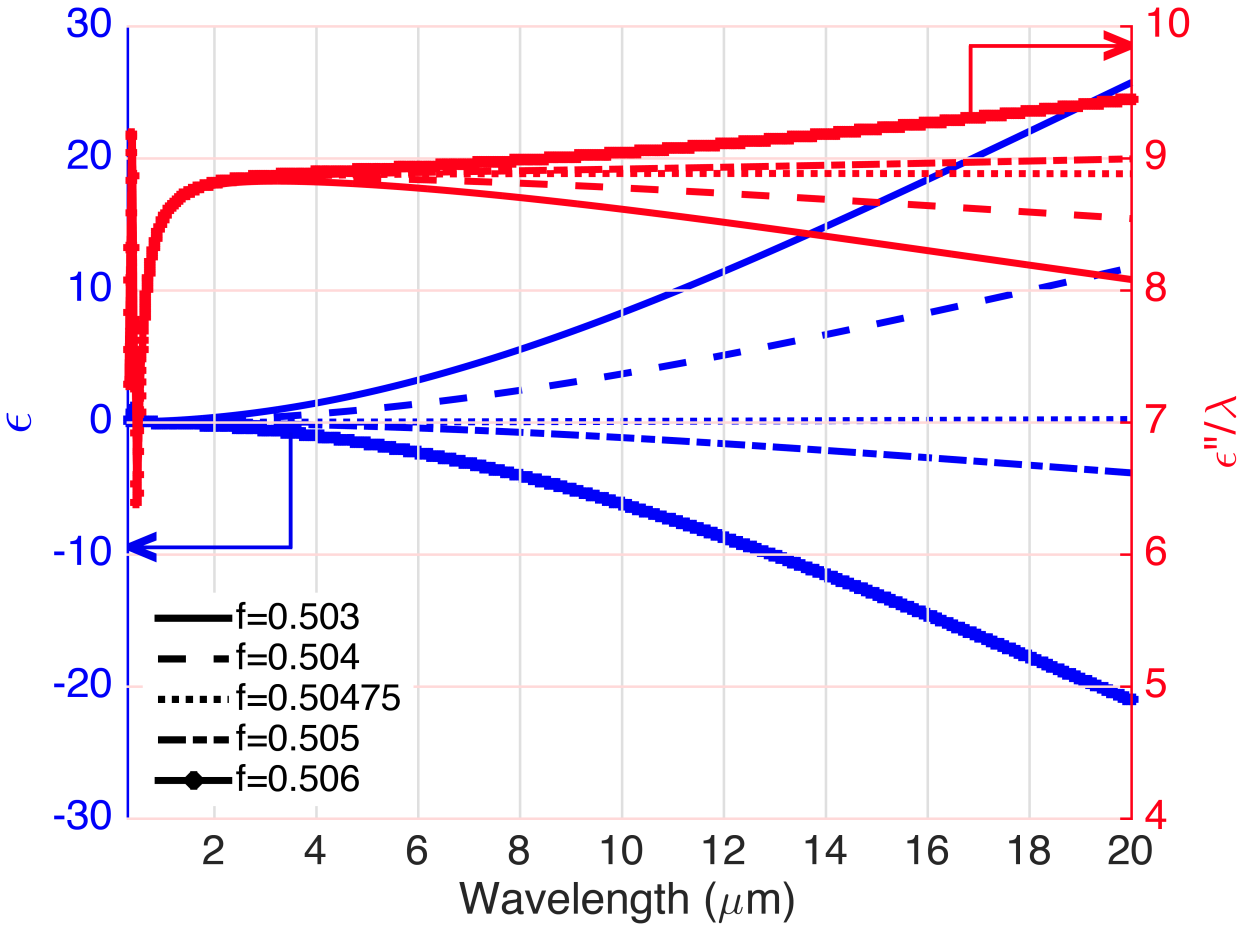

FIGURE 5.5. Real and imaginary effective epsilon of gold film with different metal filling fraction f (0.503, 0.504, 0.50475, 0.505, 0.506).

independent at f = 0.50475) of wavelength. Note that the imaginary part of the permittivity multiplied by the frequency is responsible for the energy density dissipation rate of the monochromatic plane waves. The numerical simulations show that the effective medium model works reasonably well reflecting all the observed features. The model qualitatively reproduces the cancelation of the silica absorption at 9 μm by the gold shell with gradually increasing gold coverage. The model also shows scattering suppression at the Mie resonance wavelength.

The EMT permittivity implies the long-wavelength approximation meaning that the wavelength in the bulk mixture $\frac{\lambda_0}{\sqrt{\varepsilon_{eff}}}$ is much larger than any scale of the system. It is proven though that the EMT can be inconsistent for the planar films close to the percolation threshold [86, 51]. We analyze the limitations of EMT using the scaling theory consideration. The samples can be treated as homogeneous for wavelengths larger than crossover wavelength, and the scaling theory

reduces to the effective medium description [86]. The scaling theory potentially provides a more general approach to the fractal structure and here we discuss the applicability of EMT using the scaling theory model. In the scaling theory model, the relevant length scale $L(\omega)$ is the anomalous diffusion length on the time scale $\frac{1}{\omega}$ (ω is the optical frequency) and can be much shorter than the optical wavelength. As long as the percolation correlation length ξ is larger than length scale $L(\omega)$, the film is inhomogeneous and the effective-medium approach is not applicable. Following the above arguments, films close to the percolation threshold may appear inhomogeneous even in the far-infrared regime, where ξ is much shorter than the optical wavelength but larger than $L(\omega)$. According to Yagil et al. [51] $L(\omega) = L_0\xi_0(\frac{1}{k\xi_0})^{\frac{1}{2+\theta}}$ where k is the wavenumber, θ= 0.8 for 2D, L_0 is a coefficient of nearly unity, and ξ_0 is the characteristic scale of the percolation correlation length. The exponent ν determines the scaling behavior of the percolation correlation length as p approaches p_c, $\xi = \xi_0[\frac{p-p_c}{p_c}]^{-\nu}$. The crossover from inhomogeneous to homogeneous behavior occurs at the wavelength $\lambda_\xi = 2\pi\xi_0(\frac{\xi}{L_0\xi_0})^{2+\theta}$. Using the literature data [51] with ξ_0=10 nm, L_0=1 [62], p_c=0.68, ν=1.33, we obtained the crossover wavelength of 370 nm at p = 0.505. The other source data [62] gives L_0=4 resulting in the crossover wavelength about 8 nm at p=0.505. Our simulations use p = 0.505, and the whole spectral range can be well described by the effective medium theory. This explains why the EMT shows quite good agreement with the experimental results. Note also that the long-wavelength condition, where the wavelength in the bulk mixture $\frac{\lambda_0}{\sqrt{\varepsilon_{eff}}}$ is much larger than any scale of the system, is fulfilled due to the epsilon-near-zero effective permittivity.

5.3. Methods

In order to fabricate microspheres with fractal shells, we modified a synthesis procedure developed for continuous shells [33]. See section 2.5.2 for more details. The synthesized gold-coated microspheres were deposited on zinc selenide (ZnSe) substrates for the infrared spectroscopy and on fused silica substrates for spectroscopy in the visible range.

The structural characterization was performed with Hitachi S-4800 field emission scanning electron microscope (FESEM). To collect the optical spectra in 0.32 μm-2.5 μm and 2.5 μm-20 μm wavelength ranges, we used Perkin Elmer Lambda 950 spectrometer and Nicolet Fourier-

transform infrared (FTIR) Nexus 670 spectrometer, respectively. The reflectance and scattering measurements were performed with the integrating sphere module of the Perkin Elmer Lambda 950 spectrometer [91].

5.4. Conclusions

Experimental results show that the optical response of the core-shell microsphere with a gold fractal shell is dominated by the shell absorption. Similar to the planar fractal films, the absorption is enhanced in the broad spectral range up to 20 μm . It is interesting, though, that the specular reflection and backscattering are relatively small for the fractal shells due to 3D spherical geometry. Also counterintuitive is that the resulting transmission cross-section for the core-shell is higher than the bare silica core at the Mie resonance. This is due to the forward scattering suppression of silica microspheres by adding the plasmonic gold shells. Increasing the gold coverage can gradually decrease the scattering peak of silica microsphere in the visible range, where the microsphere size is greater than wavelength. By measuring transmittance, reflectance, and forward and back scattering we found that the absorption in the shell contributes the most to the extinction of the whole core- shell microsphere. Another surprising result is that the Mie scattering resonance at 560 nm of a silica core with 780 nm diameter is suppressed by 75$\%$ and partially substituted by the absorption in the shell so that the total transmission is increased by factor of 1.6 due to the gold fractal shell. The effective permittivity of the gold shell manifests the epsilon-near-zero condition over the whole spectral range under study.

Also, in the mid-infrared spectral range, one can see that the Si-O-Si vibrational stretching band of the core is hidden in the spectra of the core-shell extinction. As the gold coverage increases on the silica microspheres, the relative contribution of the vibrational stretching band at 9 μm in the total extinction gradually decreases and eventually disappears. Effective medium theory describes the experimental spectra reasonably well and gives an epsilon-near-zero real part of the effective shell permittivity and an approximately wavelength independent product of the imaginary part of the permittivity and light frequency over the broad spectral range 0.5-20 μm (this product is responsible for the energy density dissipation rate of the plane wave). These observations for the visible and mid-IR spectra indicate that the light passes mostly through the epsilon-near- zero shell

with approximately wavelength independent absorption rate. Thus, the fractal films synthesized on the microspheres show interesting properties of guiding light and could be promising aerosolized obscurants in the visible-infrared spectral range.

CHAPTER 6

ACTIVE NANOPLASMONICS

6.1. Introduction

The focus of this chapter is on the study of nanoplasmonic and gain medium, which consists of the spaser, plasmonic gain, amplification and compensation of loss. The chapter will show the experimental results of gain nanoplasmonics. After decades of developments, studies and theories, it appears that nanoplasmonics needs a new direction which could be the active device with generator and amplifier of localized optical fields. In the semiconductor field there is an active device which acts as a nanoscale amplifier called metal oxide semiconductor field effect transistor (MOSFET) [97]. MOSFET enables almost all the electronics that we use in day to day tasks. However, there are some limitations. A bandwidth limited to $\lesssim$ 100 GHz is already an obstacle in further development of the technology. Sensitivity to high temperature and electric fields also a limiting factor for extreme situations like warfare technologies. In the nanoplasmonic field an active device is the surface plasmon amplification by stimulated emission of radiation (SPASER). Spaser was proposed [98, 99] as a quantum generator of highly localized optical fields. This Spaser effect is first seen experimentally in 2009 [100] and further developed theoretically in later studies [101, 6]. Spasers that use surface plasmon polariton (SPP) are called the nanolasers.

Active nanoplasmonic or spaser is an equivalent of laser [98, 101] and works as a quantum generator and amplifier. Figure 6.1 shows the geometry of the spaser, which consists of a metal nanoparticle that acts as a cavity (resonator) and the dye molecules as the gain (active) medium as in the laser.

As for the laser, there are two main conditions. First, the cavity (resonator), which creates the photonic mode and the gain (active) medium that is populated and inverted, creates enough energy to reach lasing mode. A laser's obvious limitation is the size of the cavity, which is is at least half of the wavelength in the propagation direction in theory, but in practice have been found to be greater [102, 103].

The spaser [98] can overcome this limitation. Metal nanoparticles' surface plasmons (SPs)

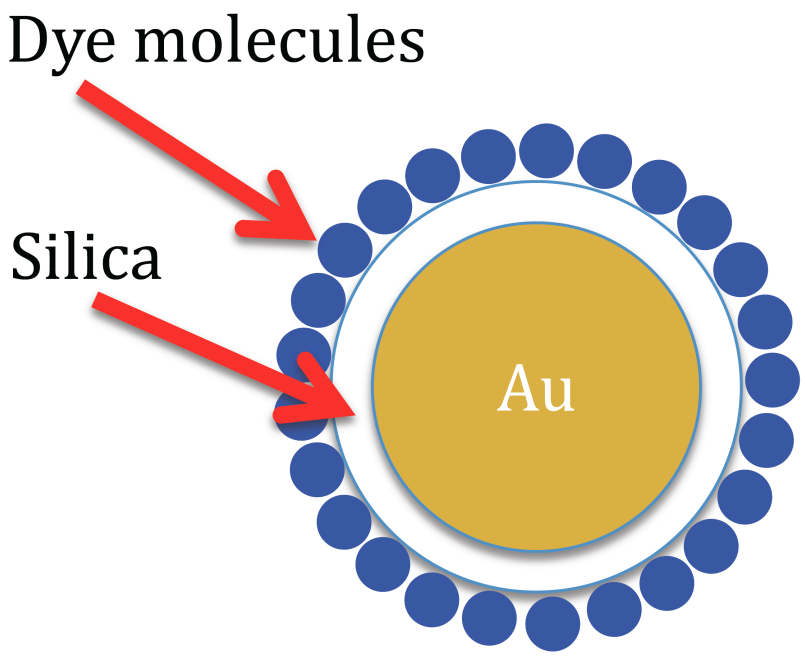

FIGURE 6.1. Schematic of a spaser geometry.

are on the nanoscale level [41] when they are localized. Also, the nonlocality length [104] l_{nl} is $\sim$ 1nm and is calculated by equation 35 where it is defined as the distance of an electron with the fermi velocity V_F moving during a period of the field.

$$l_{nl} \sim \frac{V_F}{\omega} \sim 1nm \tag{35}$$

Where ω is 2πf, f is in the range of optical frequencies, and l_{nl} in equation 35 is calculated such that the spaser is a few nanometers in the size.

$$l_s = \bar{\lambda}\left[Re\left(\frac{-\varepsilon_m^2}{\varepsilon_m + \varepsilon_d}\right)^{\frac{1}{2}}\right]^{-1} \tag{36}$$

Equation 36 calculates the skin depth (l_s), where $\bar{\lambda}$=$\lambda/(2\pi)$ is called the reduced vacuum wavelength, and ε_m and ε_d are dielectric permittivities of the metal core and dielectric shell respectively. The size of the metal nanoparticle (R) in the spaser must be much less than the wavelength λ and between l_{nl} and l_s. For silver, and gold, l_s is between 25-27 nm for the optical spectral region.

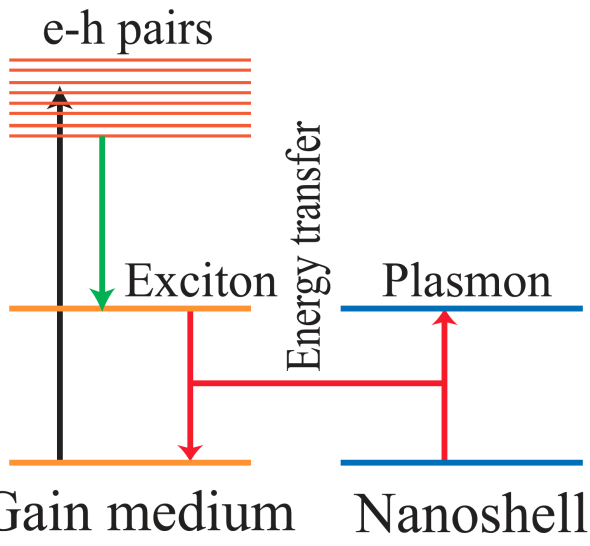

FIGURE 6.2. Theoretical process of a spaser [6].

In this study, we investigate experimentally the stimulated emission created by the spontaneous emission of inhomogeneously broadened emitters that are coupled to a metamaterial mode. This is called the spaser. Metamaterial mode in this study is core-shell nanostructures made of Au core and silica shell, and emitters are Rhodamine 800 and ATTO655 dye molecules. SPs from the Au core will excite the dye molecules and vice versa, creating the stimulated emission. When compared to lasers where photons are created, stimulated emissions through SPs are localized in nanoscale level. The emitters, or dye molecules are a two-level system similar to the laser active medium and are excited in the same way as the laser but by the SPs (this resonant Au nanoparticle is similar to laser cavity). These excited energy, stimulated by the SPs in the Au nanoparticle causes the system to buildup SPs in a single mode. The schematic of this process can be seen in figure 6.2 [6].

As discussed, spaser's emission of coherent radiation, or we call it stimulated emission, is a result of a spontaneous emission between the two-level emitter system. This was studied theoretically using Monte Carlo numerical methods by Temnov [105]. According to Temnov, these single mode SPs in the cavity, or in our case Au nanoparticle with low plasmonic quality factor (Q), inherently have bi-exponential emission characteristics. It is found that when coupling the Au nanoparticle with dye molecules we see a bi-exponential decay.

The collective modes produced during the coupling of dye molecules and plasmonic Au

nanoparticle are called superradiance and subradiance. In the bi-exponential decays, fast superradiant decay is followed by a slow subradiant decay, which was predicted by Temnov [105] using Dikie model [106]. It is also found analytically, that indeed there are superradiance and subradiance modes are present even after averaging over coupling parameters [107]. We discuss this experimentally further through time resolved fluorescence lifetime measurements in section 6.3.

6.2. The Fluorescence Process

Fluorescence occurs when the molecule undergoes a three stage process. Please refer to figure 6.3. First, an energetic photon is provided externally, which will then be absorbed by the molecule and populated by a chemical reaction to create an excited electronic singlet state $\mathbf{S}_1^{'}$.

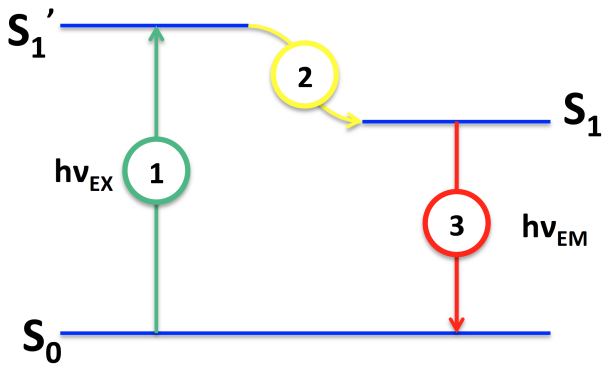

FIGURE 6.3. Two level system.

Populated excited state exists only for very small finite time ($\sim$10 ns) [6]. During this short excited state lifetime, fluorophores go through some changes due to interaction with their environment. Therefore, energy dissipated from $\mathbf{S}_1^{'}$ results in $\mathbf{S}_1$ singlet excited state. This is where the fluorescence emission originates. Not all the molecules that were excited return to ground state $\mathbf{S}_0$ as fluorescence emission due to processes such as quenching, fluorescence resonance energy transfer (FRET), etc. Thus, fluorescence quantum yield can be calculated using the ratio of the number of fluorescence photons emitted to the number of photons absorbed during the excitation. Usually, the entire fluorescence process recurs as long as fluorophores are not destroyed in the excited state. Fluorescence emission will have a longer wavelength than the excitation wavelength. This is due to energy dissipation during the $\mathbf{S}_1$ to $\mathbf{S}_1^{'}$. The energy of photon is lower and results in

longer wavelength. The energy difference between excited and emission ($hv_{EX} - hv_{EM}$) is called the Stokes shift and allows emission to be detected against the excited photons.

6.3. Results and Discussion

In this section, discussion of fabrication procedures for core-shell type nanostructures with different dye molecules attached to them. Also discussion of optical measurements carried out using UV-Vis-Near-IR spectrometer, flurometer, and time resolved fluorescence lifetime measurements using Picoquant Microtime200-Time Correlated Photon Counting (TCSPC) spectrometer.

6.3.1. Core-Shell Nanoparticles

Materials

Tetraethyl orthosilicate (TEOS), Ethanol, (3-aminopropyl)trimethoxysilane, ammonium hydroxide, and Rhodamine 800 (RH800) were purchased from Sigma-Aldrich (St. Louis, MO, USA). SU8-2000 epoxy was purchased from Micro Chem (Westborough, MA, USA). Au 20nm colloid was purchased from Ted Pella (Redding, CA, USA). ATTO655 was purchased from ATTO-TEC GmbH (Siegen, Germany).

Fabrication

Synthesis of Au-SiO_2 core-shell is done under vigorous stirring of 1 mL of Au 20 nm colloids concentration at $7E^{11}$ particles/mL in 250 mL of 200 proof ethanol solution. After the stirring was done for 10 minutes, 4 mL of 30% ammonium hydroxide was added. Immediately after adding ammonium hydroxide, 100 μL of TEOS were added to the solution. The solution was stirred for 2 hours and the solution aged without stirring at 4^oC for 24 hours. After that, solution was centrifuged (3000 rpm, 30 minutes) and washed with ethanol 4 times. Next, 500 μL of (3-aminopropyl)trimethoxysilane was added to the separated solution (10 mL) and stirred vigorously for 24 hours and separated again [108]. The figure 6.4 show that there is only few nanometers difference between Au and Au-SiO_2 due to the thin silica shell thickness, which is described below. Peak positions for 20nm Au nanoparticles and Au-SiO_2 are at 526 nm and 528 nm respectively.

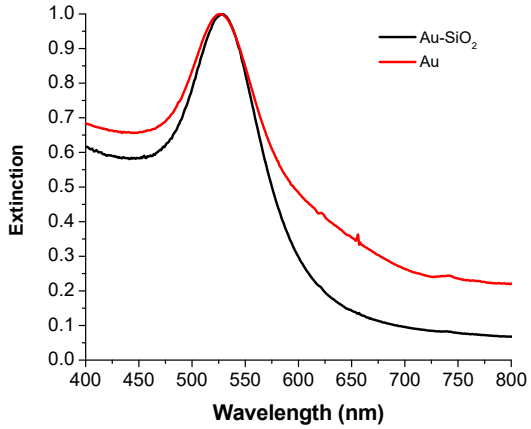

FIGURE 6.4. Normalized Extinction of Au-SiO_2 and Au (20nm) in Ethanol in 2mm Cuvette.

Preparation of fluorescent-coated Au-SiO_2 core-shell is done by dyeing (doping) method. Add 4 mL of 6.2 μM ATTO655 (in ethanol) to 100 μL of Au-SiO_2 ($7E^9$ particles) and keep it in a shaker for 24 hours. After completion of the procedure, once again separate the particles using previously mentioned method and re-disperse in 10% SU8. Substrate preparation for optical time resolved confocal fluorescence spectroscopy was done as follows. Thin glass substrates (0.25 mm thickness) were used in this experiment, and the final solution spin coated in 10% SU8 at different spin speeds from 500rpm to 10000rpm. Then let it dry for a few hours before taking the optical measurements (figure6.5).

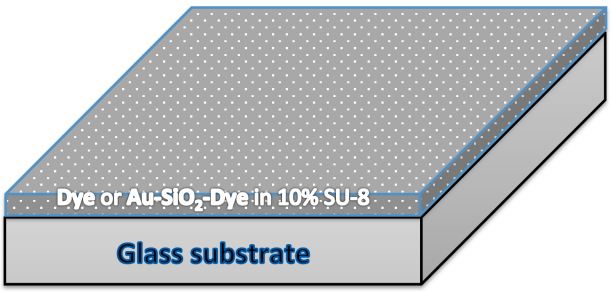

FIGURE 6.5. Scheme of how the dye molecules and core-shell nanoparticles with dye molecules are deposited on a glass substrate for experimental measurements.

The fabricated core-shell nanoparticles with Au as the core and silica as the shell have a broad size distribution. As you see from figure 6.6, there are three types of core-shell structures: one with single core-shell, one with two Au cores and one shell around them, and another with two

separate cores but shells which are connected together.

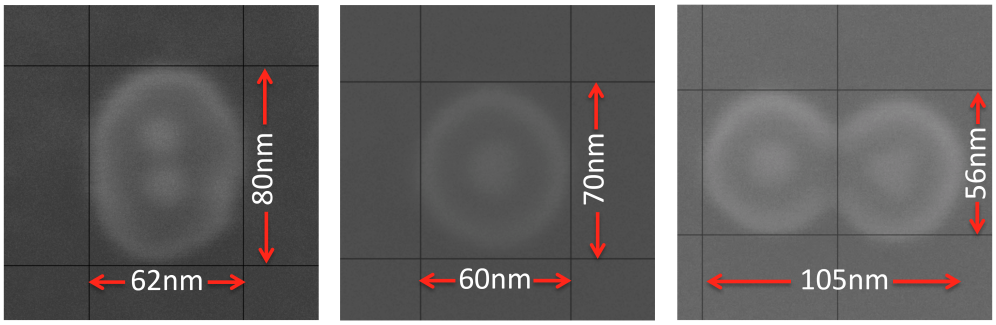

FIGURE 6.6. Coreshell nanoparticle size distribution is shown here. Left image shows that it has two cores (Au nanoparticles) inside the shell, which makes the Y axis longer than others. Middle image shows bit larger coreshell particle. Right image shows different conjoint coreshell particle. The difference between this and the left coreshell structure is the separation of the core particles.

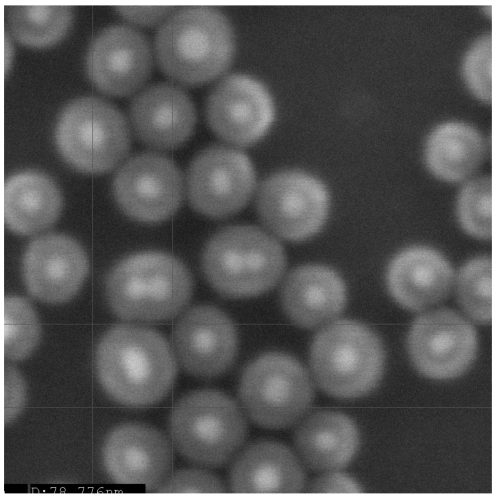

FIGURE 6.7. Coreshell nanoparticle distribution on the substrate. This includes different types of coreshell structural types mentioned in figure 6.6.

The FESEM images in figure 6.7 show how these core-shells are distributed on substrate. 24% of the coreshell particles are in the range of r=25-26 nm, which means that the total diameter of the core-shell is in the range of 50-52 nm. By considering table 6.1, the Au mean particle size is 19-21 nm in diameter. The thickness of the shell is around 15.5 nm. The broad size distribution in figure 6.8 shows that the sample contains groups of emitters with quite broad coupling parameters.

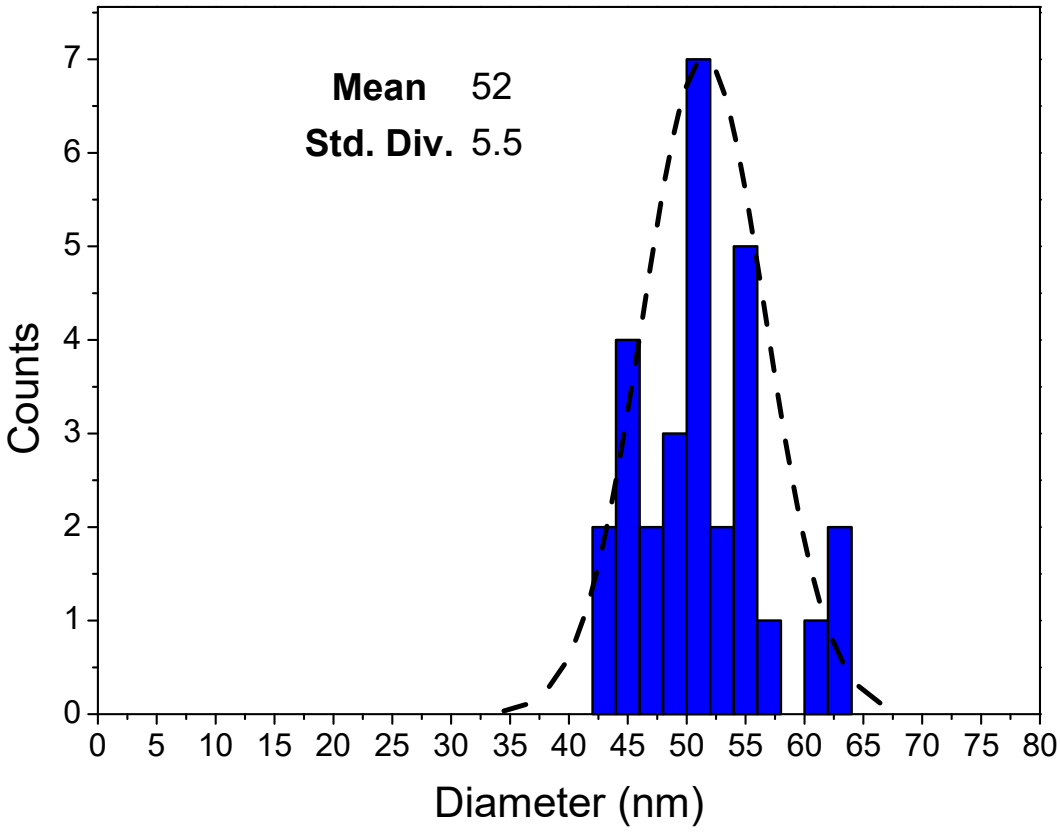

FIGURE 6.8. Size distribution graph for core-shell nanoparticles on the substrate.

TABLE 6.1. 20 nm Au nanoparticle size distribution

Size of Au Nanoparticle	Mean Particle Size	Maximum Acceptable %CV[a]	Number of Odd Shapes per 100 particles
20nm	19.0-21.0nm	8%	$\leq$5

[a]Coefficient of Variation (CV).

6.3.2. Dye Molecules

In this study, we have used two different dye molecules (fluorophores), ATTO655 and Rhodamine 800 to study their optical properties before and after attaching them to core-shell structures mentioned in section 6.3.1.

ATTO655

ATTO655 is a zwitterionic dye [109], a molecule containing a positively charged ion at one end a negatively charged ion at the other end, resulting in zero net electrical charge. This dye is highly suitable for single molecule detection and high resolution application. It provides strong absorption over longer time periods of irradiation compared to other dye molecules such as Cy5 [109].

In this study's experimental results, ATTO655 (see figure 6.9) is dissolved in ethanol at 5 nM and excitation and emission peak positions are found at 656 nm and 663 nm, respectively.

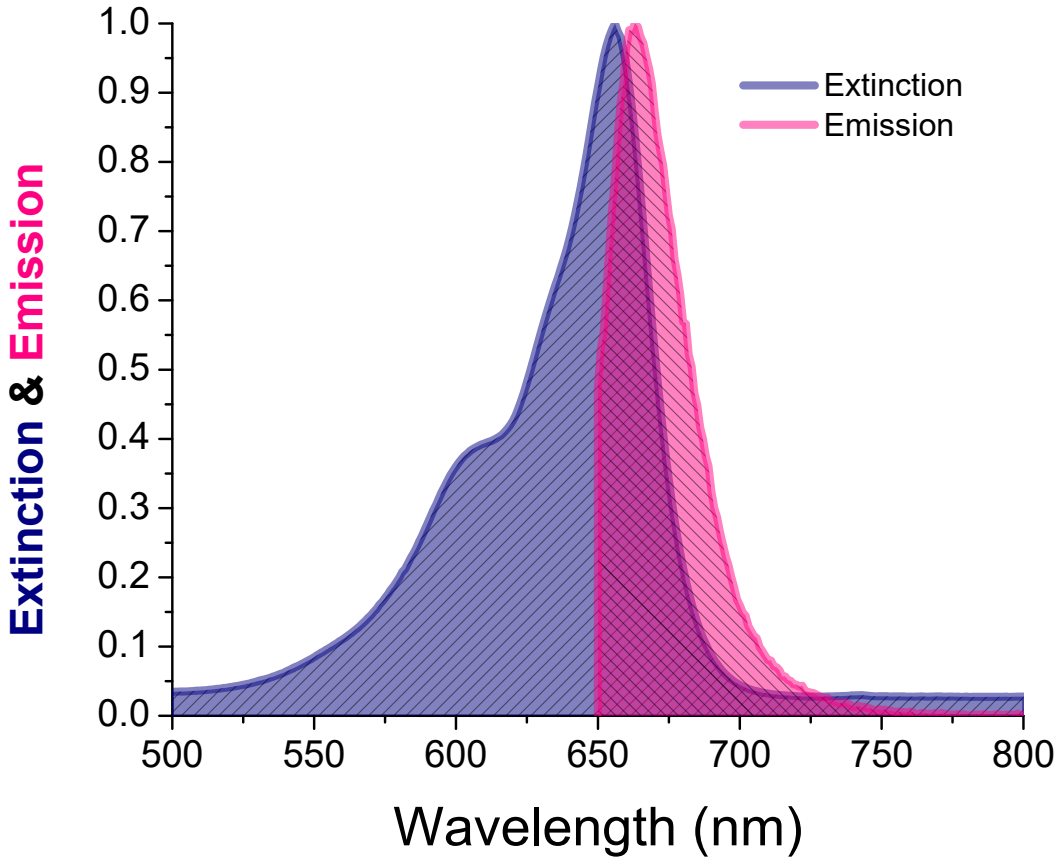

FIGURE 6.9. Normalized Extinction and Emission of ATTO655 in Ethanol (5 nM in 2mm Cuvette).

Rhodamine 800 (RH800)

Rhodamine 800 is a xanthenes family dye, an organic compound mainly used as a class of dye ranging from yellow to red. Figure 6.10 shows the normalized extinction and emission (excited at 640 nm). RH800 extinction spectrum shows maximum absorption above 675 nm, and emission around 710 nm.

In this study's experimental results, RH800 is dissolved in ethanol at 25μM and excitation and emission peak positions are found at 682 nm and 702 nm, respectively.

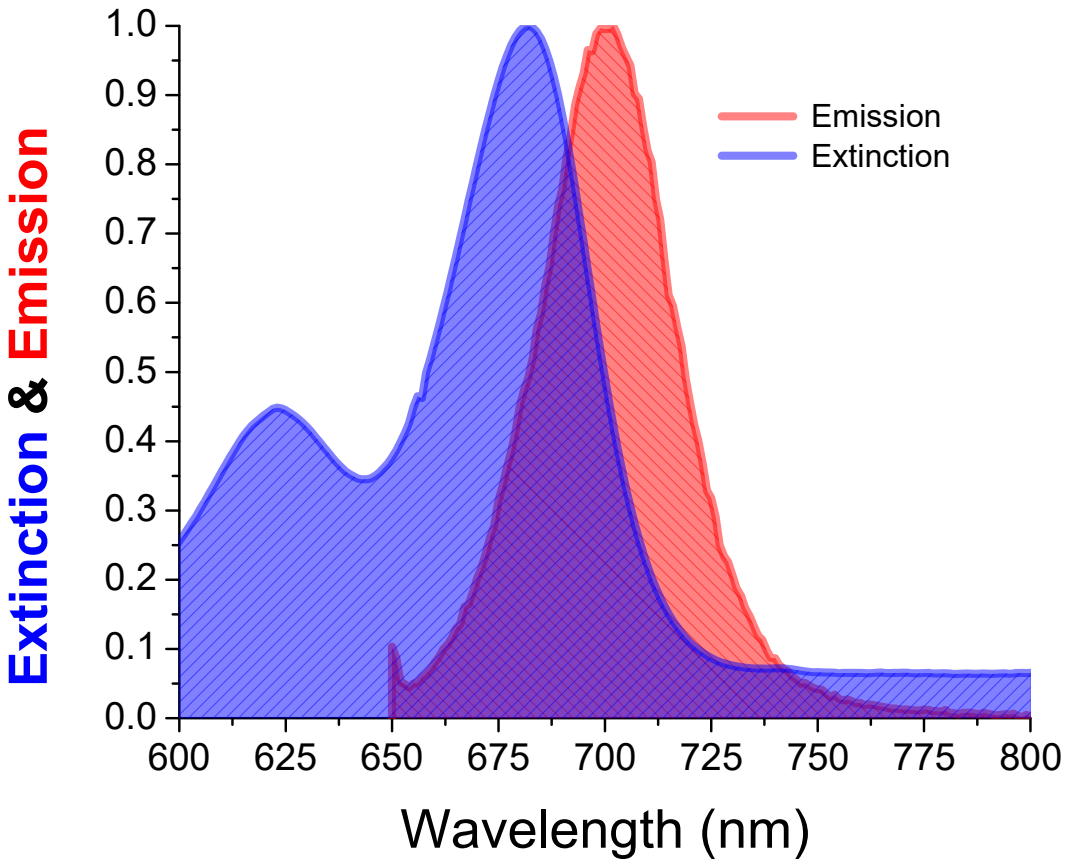

FIGURE 6.10. Normalized Extinction and Emission of Rhodamine 800 in Ethanol (25μM in 2mm Cuvette).

6.3.3. Dye Doped Core-Shell Nanoparticles

ATTO655 doped Au-SiO_2 nanoparticles were dispersed in 10% SU8. The extinction and emission spectra in figure 6.11 have peak positions at 531 nm and 665 nm, respectively. It is found

that Au-SiO_2 has peak extinction at 528 nm (see figure 6.4), but when the ATTO655 is doped, peak position is red-shifted by 3 nm.

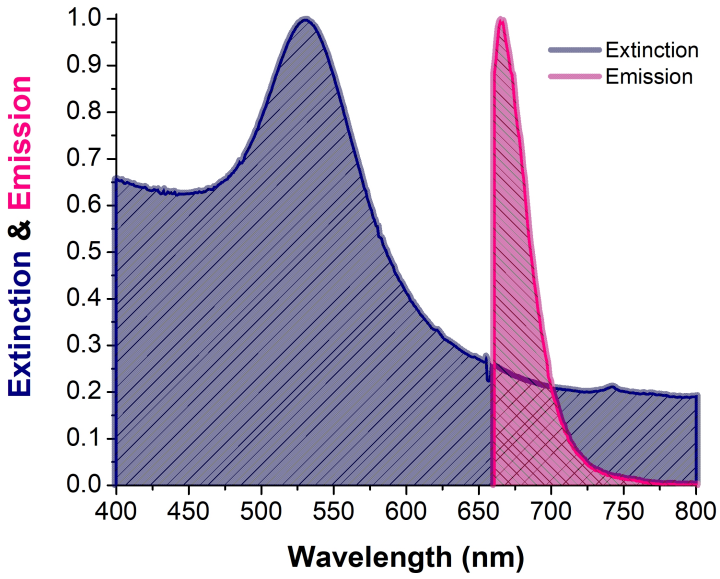

FIGURE 6.11. Normalized Extinction and Emission of Au-SiO_2-ATTO655 in 10% SU8 (5nM in 2mm Cuvette).

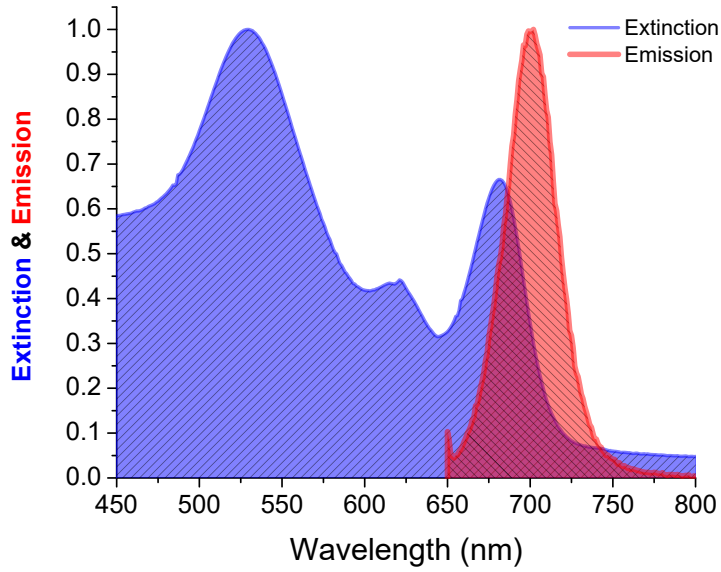

FIGURE 6.12. Normalized Extinction and Emission of Au-SiO_2-RH800 in 10% SU8 (5nM in 2mm Cuvette).

RH800 doped Au-SiO_2 nanoparticles were dispersed in 10% SU8. The extinction and emission spectra in figure 6.12 have peak positions at 530 nm and 702 nm, respectively. Peak position of the extinction is red-shifted to red by 2 nm when compared with the extinction peak of Au-SiO_2 (see figure 6.4).

6.3.4. Time-Correlated Photon Counting (TCSPC)

A picosecond pulsed diode laser is used to excite dye or core-shell with dye samples spin-coated on thin glass substrates, with spectral line at 640 nm with 80 ps pulsed width. Also it is possible to have a continuous wave (CW) operation as well. Laser light is focused through Olym-

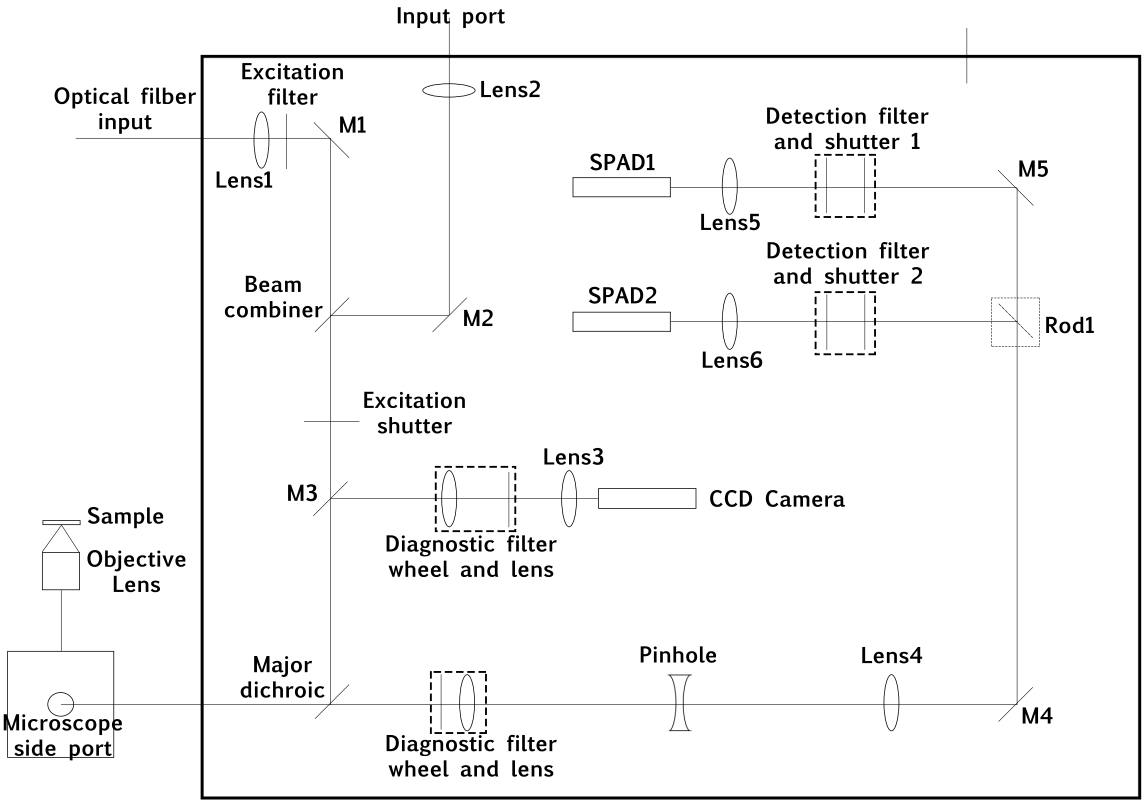

FIGURE 6.13. Diagram of Picoquant Microtime200.

pus 60x 1.2NA water immersion objective lens which is mounted in an Olympus IX71 confocal microscope. We used the MicroTime 200 time resolved confocal microscope system (PicoQuant, Berlin, Germany) to direct the laser as seen from the figure 6.13. The laser is aligned into the MicroTime 200 main optical unit (MOU)by coupling through fiber. An excitation bandpass filter is

used to clean up the 640nm laser, and an emission bandpass filter that works in the range of 655 nm $<$ fluorescence $<$ 725 nm, is used for the time resolved emission collection. The major dichroic beam splitter with 50% reflection starts at 605 nm and ends at 650 nm. This major dichroic directs the excitation beam into the Olympus IX71.

Time-Correlated Photon Counting (TCSPC) measurements were taken by focusing the laser beam on to the sample on a 0.25mm glass substrate. There will be a fluorescence response and back scattered excitation light by the sample, which is going to be perpendicular to the excitation beam, passes through the major dichroic, reflects the the back scattered excitation light into the diagnostic section. As seen from the diagram in figure 6.13, reflected beam focuses through **M2** and is steered by **M3** and **M4** mirrors to the CCD camera. The output of the video is displayed in the SymPhoTime software. The fluorescence goes through a optical filter that is selected by the filter wheel. In our case it is the emission band pass filter mentioned in the previous paragraph. Then the beam is focused by an achromatic tube lens to the 50 μm pinhole. Then the collimated beam passes through beam splitters and reaches the detectors. The detectors that collect the fluorescence photons are called 2-Tau-SPADs, and use single photon avalanche diodes. These SPADs have active area diameter between 50 μm to 100 μm with spectral range from 400 nm to 1000 nm (highest quantum efficiency around 550 nm)

Time Tagged Time Resolved (TTTR) Data acquisition is done through PicoHarp 300 standalone unit. This unit supports two time tagging modes, T2 and T3 modes. They vary by their input channels. T3 mode is specifically use for periodic signal with high repetition rate up to 84MHz [110]. Channel one is dedicated to the sync signal, where time tag is measured by counting the sync pulses. Channel two receives the stop signals from detectors, and synchronization information is fed to PicoHarp 300 through MicroTime 200 Microscope controller. This method allows us to measure the exact sync time period that correspond to the arrival time of photon with respect to total time of the experiment. In other words, it measures the time between excitation and emission, which can be used to measure fluorescence lifetime.

T2 mode uses both signal inputs from both photon detectors, and no sync signal. Both inputs record information about the channel it came from and arrival time with respect to the total

time of the experiment. Detectors and electronics go silent for typically 90 ns [110]: this is called the dead time but does not occur across the channels. Thus, one can analyze cross correlation that can be calculated with zero lag time. This includes Fluorescence Correlation Spectroscopy (FCS), Antibunching and many more valuable applications.

Antibunching experiments are performed using an interferometer setup by Hanbury Brown-Twiss. In the Picoquant system, the emitted light is split with a 70/30 beam splitter onto two single photon sensitive SPAD detectors. The SPAD outputs are then connected to a TCSPC unit and the time difference between two output signals coming from two emitted photons through the sample are repetitively measured and graphed with the highest resolution (picosecond). The measured antibunching experiments are done using continuous wave (CW) excitation. The antibunching results using CW excitation show an even level line with a notable dip at a time difference of zero. This is because a single molecule can emit only one photon at a time.

The principle of TCSPC is to measure the time between excitation and emission, i.e. the fluorescence lifetime. The excitation pulse from the laser is identified by a constant function discriminator (CFD) which sends a start signal to a time to amplitude converter (TAC). Once the TAC is triggered, the voltage is increased linearly with time until a stop signal, initiated by the detection of a single photon, is received from the CFD connected to the detector. The voltage on the TAC at the time of a stop signal from the detector is amplified and passed via an analog to digital converter (ADC) to a PC which logs times in a histogram. The intensity of the excitation is set low enough that less than 1% of the excitation pulses result in a fluorescence photon being detected. This reduces the probability of multiple emission events occurring per excitation pulse, which would result in a deviation from Poisson statistics.

6.4. Lifetime Fitting

The picoquant Microtime 200 system has its own software for data analysis and fitting called SymPhoTime. In this software, the fitted data is characterized by a few conditions. First, the fitted curve should adequately overlay with the decay curve. Second, the weighted residual values should spread arbitrarily around zero. A good fit is estimated by plotting the weighted residuals R(i) vs. time. Here R(i) is defined as $R(i) = W(i)[Decay(i) - Fit(i)]$ and is usually plotted

below the fitted decay plot. The advantage of having such a plot is that it can show where the misfit happens. As mentioned earlier, usually weighted residual spread randomly around zero, but sometimes there are some spikes near the rising edge of Instrument Response Function (IRF) or decay. These are usually due to instrument artifacts. Lastly, the χ^2_R value should approach one. If these three conditions are satisfactory, the calculated fitting values are said to be reasonable.

For lifetime, fit parameter assumes gaussian noise of the measured curve. The χ^2 is a good approximation for lifetime fitting only if there are enough counts in each channel of the decay curve.

$$\chi^2 = \sum_i \frac{[Decay(i) - Fit(i)]^2}{Decay(i)} \tag{37}$$

In our case, we have two data channels with more than 10 counts, as Picoquant [110] requires more than 10 counts for such fitting. χ^2_R is reduced chi square and defined in the following equation. Here $N - p \sim \chi^2$. $\chi^2_R \gg 1$ indicates a poor fitting of the lifetime data, and $\chi^2_R \ll 1$ indicates that errors on the lifetime data is over estimated.

$$\chi^2_R = \frac{1}{N-p} \sum_i \{[Decay(i) - Fit(i)].W(i)\}^2$$
$$\chi^2_R = \frac{1}{N-p} \sum_i \frac{[Decay(i) - Fit(i)]^2}{Decay(i)} \tag{38}$$

with $W(i) = \frac{1}{\sqrt{Decay(i)}}$

Parameters:

- N: Number of fitted channels.
- p: Number of fitted parameters.
- W(i): Weighting factor for the ith channel.
- Decay(i): Measured intensity for the ith channel.
- Fit(i): Fitted intensity for the ith channel.

6.4.1. Lifetime Fitting Methods

A time Correlated Single Photon Counting (TCSPC) system relies on the precise accuracy of overall timing. TCSPC system is characterized by the IRF. In an ideal system, or a system with extremely accurate detectors and electronics, would observe a very sharp excitation pulse, which would result in extremely narrow IRF. But the systems we have do not have such a luxury. Our systems will have broadened IRF due to the laser source 80 ps pulse duration, detectors and electronics. Therefore, we need to analyze decay curves precisely with the proper method. There are two methods, namely Multi-Exponential Reconvolution and Multi-Exponential Tailfit. Multi-exponential Reconvolution is the best method to use when fitted lifetimes are shorter than the IRF. And Multi-exponential Tailfit can be used only when the fitted lifetimes are significantly greater than the IRF.

Multi-Exponential Reconvolution

$$y(t) = \sum_{i=0}^{n-1} \mathbf{IRF} \bigotimes |_{Bkgr_{IRF}|Shift_{IRF}} \mathbf{A}[i] exp \frac{t}{\tau[i]} + Bkgr_{Dec} \tag{39}$$

Multi-Exponential Tailfit

$$y(t) = \sum_{i=0}^{n-1} \mathbf{A}[i] exp - \frac{t - t_0}{\tau[i]} + Bkgr_{Dec} \tag{40}$$

Model Parameters:

- n: Number of exponentials.
- t_0: Extrapolated reference point for scaling the exponential prefactors.

Fitting Parameters:

- A: Exponential prefactors ('amplitudes').
- τ: Exponential decay times (e.g. lifetimes).
- Bkgr$_{Dec}$: Correction for decay background (afterpulsing, dark counts, environmental light).

- Shift$_{IRF}$: Correction for IRF displacement (e.g. wavelength dependent time zero of the detector).
- Bkgr$_{IRF}$: Correction for IRF background (afterpulsing, dark counts, environmental light).

6.5. Lifetime Measurements

The lifetime measurements were done in liquid and on substrates for both dye molecules and dye doped core-shell nanoparticles. For the liquid, absolute ethanol and diluted epoxy were used. And for the substrate measurements, dye molecules and dye doped core-shell nanoparticles were dissolved in diluted epoxy and spincoated on a thin glass substrate.

ATTO655 and ATTO655 Dopped Core-Shell in 10% SU8

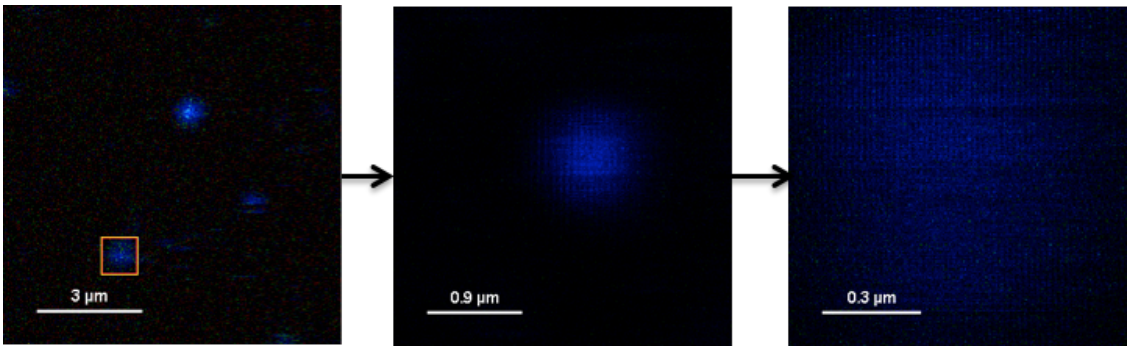

FIGURE 6.14. The fluorescence life time microscopy (FLIM) images.

Figure 6.14 shows the fluorescence lifetime microscopy (FLIM) images. When the dye molecules or dye doped core-shell particles on thin 0.25 mm substrate were focused by the laser beam and scanned at a certain area of interest, saw the lifetime distribution through FLIM as seen in figure 6.14. This was taken by focusing the laser beam on to the correct beam waist on Z axial position. In other words, we need correct axial position of the excitation laser light with respect to the thin glass substrate top surface, where glass meets air. The bottom surface is the glass and water interface. This is important in order to get the best resolution and highest transmission through the 50 μm pinhole. To achieve such conditions, one needs to focus the beam with respect to the fluorescent sample types. If the fluorescent samples are bigger than 100 nm, focus the laser beam waist to the above surface of glass and air interface, and if the fluorescent samples are

smaller, focus the laser beam waist to the interface of top glass surface. This will provide maximum fluorescent signal out of respective samples.

FLIM images shown in figure 6.14 are done for dye doped core-shell nanoparticles. The left image was done for a larger area and shows few bright spots. The middle image shows a smaller area of the previous image, which was scanned again to get precise measurement. And the last image on the far right shows much smaller area of the middle image, which was selected and scanned to collect proper measurements for lifetime decays of dye doped core-shell nanoparticles. It was calculated that the radius (R) of the beam waist is going to be around 0.325 μm for excitation wavelength at 640 nm for 60x 1.2NA water immersion objective lens. Figure 6.15 represents how the dye doped core-shell nanoparticles were distributed on the substrate after being spincoated. As seen from the FESEM image with scale bar at 1 μm, there are few different nanoparticle patterns that are distributed along the substrate: single nanoparticles, circle of nanoparticles, lines of nanoparticles and some empty areas. When performing FLIM measurements at such a collection diameter 0.650 μm (d=2R), one can get fluorescence emission from group of nanoparticles.

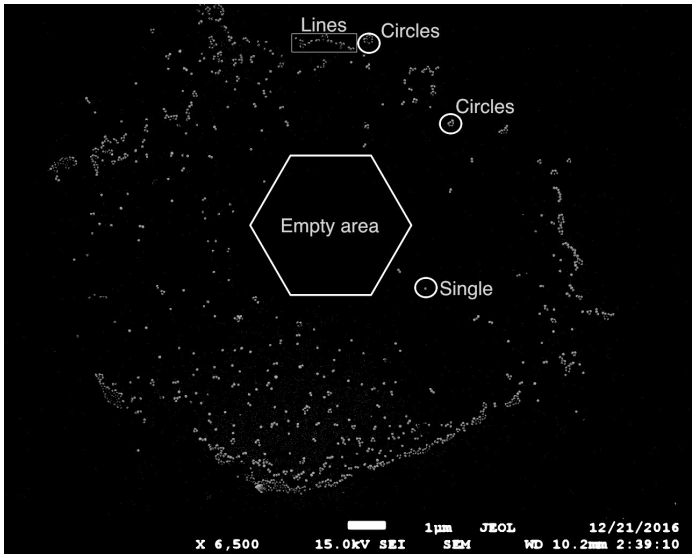

FIGURE 6.15. FESEM image shows how the core-shell particles in 10% SU8 is distributed on Silicone substrate at 2000rpm.

In order to calculate the lifetime measurements, one first needs to fit the raw data according to one of the fitting methods mentioned in section 6.4. The fitted data are readable as equation 41, where I_1 and I_2 are the total number of photons collected during the lifetime measurement fitting

with kilo counts(Kcnts) as the units, and each corresponds to short and long exponents. A_1 and A_2 are the exponential prefactors (amplitudes) with kilo counts (Kcnts) as the units, and τ_1 and τ_2 are the exponential decay times for each short and long decays.

$$I(t') = \int_{-\infty}^{t} IRF(t') \sum_{i=1}^{n} A_i e^{-\frac{t-i}{\tau_i}} dt' \tag{41}$$

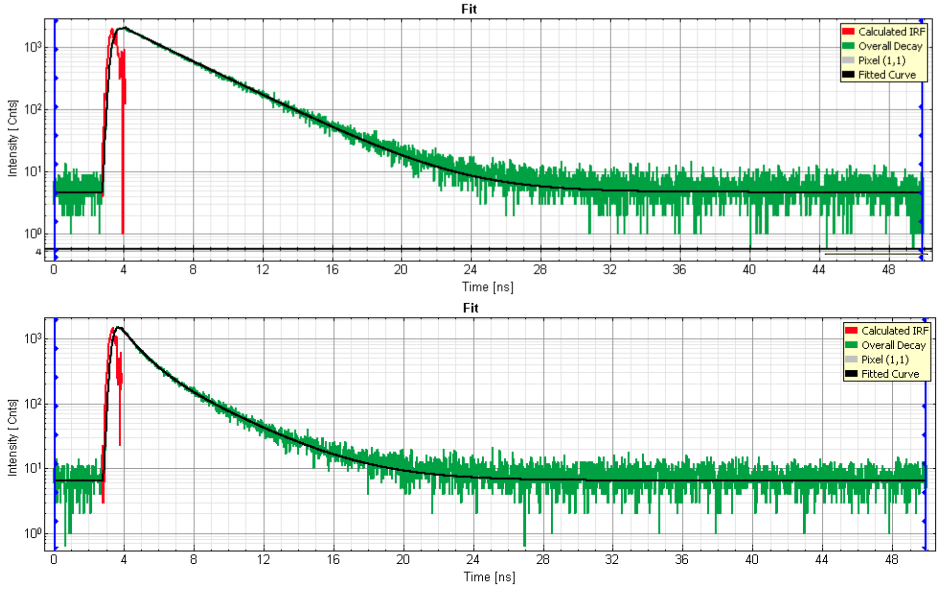

FIGURE 6.16. (Top) A single exponential emission decay and (Bottom) bi-exponential emission decay; Green color is the raw data, Black is the fitting with the exponential reconvolution, and Red is the IRF.

As per equation 41, bi-exponential fitting has two components, and single exponential fitting has only one. Both single exponential and bi-exponential fitting are shown in figure 6.16. The top figure is an example of the ATTO655 313 μM in 10% SU8 dried droplet on the substrate, with lifetime 3.2 ns which shows single exponential decay with χ^2_R=1.062. This lifetime of 3.2 ns is done without the core-shell nanostructure. ATTO655 5nM in 10% SU8 in liquid was measured in 2mm cuvette and found out that lifetime is 1.88 ns with χ^2_R=1.041. Next ATTO655 5nM in 10% SU8 was spincoated on a substrate and measured with fitting of χ^2_R=1.035, and lifetime of 2.17 ns. Lifetime of fluorophores change with the environment. It was found that ATTO655 in phosphate-buffered saline (PBS) has a lifetime of 1.8 ns [109].

TABLE 6.2. Lifetime measurements of ATTO655 and ATTO655 doped core-shell nanoparticles in 10% SU8

Sample	CA[a]	Fit [b]	I_1	I_2	A_1	A_2	τ_1(ns)	$\pm\tau_1$(ns)	$\tau_2(ns)$	$\pm\tau_2$(ns)	n	χ^2_R
1 [c]	0.322	ERF	499	NA	2.5	NA	3.2	0.0033	NA	NA	1	1.062
2 [d]	0.322	ETF	8.37	NA	0.071	NA	1.88	0.037	NA	NA	1	1.041
3 [e]	0.322	ERF	90	NA	0.66	NA	2.17	0.0071	NA	NA	1	1.035
4[f]	0.322	ERF	19	8	0.692	0.056	0.44	0.0044	2.5	0.1	2	1.010

[a]Collection area

[b]ERF: Exponential Reconvolution Fit, ETF: Exponential Tail Fit.

[c]ATTO655 313μM droplet

[d]ATTO655 5nM 2mm cuvette

[e]ATTO655 5nM 2000rpm

[f]Au-SiO_2-ATTO655 2000rpm

When lifetime of dye doped core-shell was measured, it is shown in table 6.2 that the decay mechanism changed rapidly as it became bi-exponential. With better fitting χ^2_R=1.010, ATTO655 doped core-shell shows bi-exponential behavior with shorter τ_1 and longer τ_2 lifetimes, 0.44 ns and 2.5 ns, respectively. This is exactly what the theory [105] predicted. But when fitted with single exponent, $\chi^2_R \sim$1.4, which is not a good fit. This particular sample is spincoated at 2000rpm.

RH800 and RH800 Dopped Core-Shell in 10% SU8

TABLE 6.3. Lifetime measurements of RH800 and RH800 doped core-shell nanoparticles in 10% SU8

Sample	CA[a]	Fit [b]	I_1	I_2	A_1	A_2	τ_1(ns)	$\pm\tau_1$(ns)	$\tau_2(ns)$	$\pm\tau_2$(ns)	n	χ^2_R
1[c]	1.020	ERF	1221	1003	8.5	16.8	2.298	0.013	0.953	0.011	2	1.055
2[d]	0.0001	ERF	94	46	0.725	1.170	2.080	0.014	0.632	0.0089	2	1.011
3[e]	0.0004	ERF	117	120	0.632	2.30	2.950	0.024	0.85	0.0054	2	1.008
4[f]	0.0001	ERF	124	99	0.696	1.7	2.840	0.014	0.934	0.012	2	1.011

[a]Collection area

[b]ERF: Exponential Reconvolution Fit, ETF: Exponential Tail Fit.

[c]RH800 100μM 2000rpm

[d]RH800 100μM 2000rpm

[e]Au-SiO_2-RH800 2000rpm

[f]Au-SiO_2-RH800 2000rpm

Table 6.3 summarize the lifetime measurements done for RH800 and RH800 doped core-

shell nanoparticles in 10% SU8 spincoated at 2000rpm on 0.25 mm thin glass substrates. It is found that RH800 on substrate show bi-exponential decay compared to ATTO655 on substrate. One of the major differences between these two dye molecules are the concentrations: RH800 is at 100 μM and ATTO655 at 5 nM. It is found that for RH800 on substrate has shorter decay time between 0.6 to 0.9 ns and longer lifetime decay between 2 to 2.3 ns with good χ_R^2 fitting.

As for the RH800 doped core-shell nanoparticles, decay is bi-exponential. It shows better χ_R^2 fitting with shorter decay between 0.8-0.9 ns and longer decay between 2.8 to 2.9 ns.

6.6. Conclusions

It can be concluded from the experimental results that dye doped core-shell nanoparticles are represented by broad distribution of particle size, shape, and aggregate patterns, which can be seen from figures 6.15, 6.6, and 6.7. This distribution results in different coupling parameters and shows bi-exponential characteristics.

As we discussed earlier in section 6.1, dye molecules go through a superradiant and subradiant decay via plasmonic surface when there is coupling between them. It is found that subradiant decays have longer decay times with shorter amplitudes. Experimental data from tables 6.2 and 6.3 with bi-exponential decays show that indeed subradiant mode has longer lifetime and shorter amplitudes, which proves that the theory is accurate [105].

ATTO655 dye molecules on different solvents and on substrate shows single exponential fitting with very good χ_R^2 fitting parameters. The same can't be said for the RH800 dye molecules. The data for substrate measurements show only bi-exponential decay, but can't say conclusively that the decay will be bi-exponential for RH800, as the concentration was too high for RH800 measurements. Low concentrations, comparable to ATTO655, did not show any emission. Thus higher concentrations were needed.

ATTO655 dye molecules prepared with drop and dry method show longer lifetimes compared to the solvent and spincoated measurements. This is probably due to the thickness of the dried spot. It is important to mention that environment differences in the sample impact the lifetime decays. It is found that dye doped core-shell nanoparticles on substrate always show bi-exponential decays, even with the broad core-shell nanoparticle distribution and geometries.

BIBLIOGRAPHY

[1] The British Museum, *Lycurgus cup*, (2008). vii, 2

[2] CF Bohren and DR Huffman, *Absorption and scattering of light by small particles*, Wiley-Interscience, 1983. vii, 7, 8, 9, 10, 12, 13, 15, 16, 55, 57

[3] Zhen Sen Wu, Li Xin Guo, Kuan Fang Ren, Gerard Gouesbet, and Gerard Grehan, *Improved algorithm for electromagnetic scattering of plane waves and shaped beams by multilayered spheres*, Applied optics 36 (1997), no. 21, 5188–5198. vii, 16, 17, 56, 57

[4] S Ducourtieux, VA Podolskiy, S Grésillon, S Buil, B Berini, P Gadenne, AC Boccara, JC Rivoal, WD Bragg, K Banerjee, et al., *Near-field optical studies of semicontinuous metal films*, Physical Review B 64 (2001), no. 16, 165403. viii, 40, 41

[5] Dentcho A Genov, Andrey K Sarychev, and Vladimir M Shalaev, *Metal-dielectric composite filters with controlled spectral windows of transparency*, Journal of Nonlinear Optical Physics & Materials 12 (2003), no. 04, 419–440. viii, 26, 40, 41, 42, 44, 48, 49, 52

[6] Mark I Stockman, *The spaser as a nanoscale quantum generator and ultrafast amplifier*, Journal of Optics 12 (2010), no. 2, 024004. ix, 4, 62, 64, 65

[7] Richard A Zsigmondy, *Properties of colloids*, Nobel Lecture (1926), 45–57. 1

[8] Friedrich E Wagner, Siegfried Haslbeck, L Stievano, S Calogero, QA Pankhurst, and K-P Martinek, *Before striking gold in gold-ruby glass*, Nature 407 (2000), no. 6805, 691–692. 2

[9] Vladimir M Shalaev, Robert Botet, and Andrey V Butenko, *Localization of collective dipole excitations on fractals*, Physical Review B 48 (1993), no. 9, 6662. 3

[10] S Grésillon, L Aigouy, AC Boccara, JC Rivoal, X Quelin, C Desmarest, P Gadenne, VA Shubin, AK Sarychev, and Vladimir M Shalaev, *Experimental observation of localized optical excitations in random metal-dielectric films*, Physical Review Letters 82 (1999), no. 22, 4520. 3, 31, 49, 52

[11] Andrey K Sarychev, VA Shubin, and Vladimir M Shalaev, *Anderson localization of surface plasmons and nonlinear optics of metal-dielectric composites*, Physical Review B 60 (1999), no. 24, 16389. 3

[12] John David Jackson, *Classical electrodynamics*, Wiley, 1999. 3, 7, 9

[13] Lukas Novotny and Bert Hecht, *Principles of nano-optics*, Cambridge university press, 2012. 3

[14] Katrin Kneipp, Yang Wang, Harald Kneipp, Lev T Perelman, Irving Itzkan, Ramachandra R Dasari, and Michael S Feld, *Single molecule detection using surface-enhanced raman scattering (sers)*, Physical review letters 78 (1997), no. 9, 1667. 4

[15] Masatoshi Osawa, *Surface-enhanced infrared absorption*, Near-Field Optics and Surface Plasmon Polaritons, Springer, 2001, pp. 163–187. 4

[16] Patrice Gadenne, F Brouers, Vladimir M Shalaev, and Andrey K Sarychev, *Giant stokes fields on semicontinuous metal films*, JOSA B 15 (1998), no. 1, 68–72. 4

[17] Steven J Oldenburg, Sarah L Westcott, Richard D Averitt, and Naomi J Halas, *Surface enhanced raman scattering in the near infrared using metal nanoshell substrates*, The Journal of chemical physics 111 (1999), no. 10, 4729–4735. 4, 25

[18] JC Owrutsky, DA Steinhurst, HD Ladouceur, HH Nelson, and AP Baronavski, *Obscurants for infrared countermeasures iii*, Tech. report, DTIC Document, 2001. 4, 25

[19] Xiaohua Huang, Ivan H El-Sayed, Wei Qian, and Mostafa A El-Sayed, *Cancer cell imaging and photothermal therapy in the near-infrared region by using gold nanorods*, Journal of the American Chemical Society 128 (2006), no. 6, 2115–2120. 4, 25

[20] Oara Neumann, Curtis Feronti, Albert D Neumann, Anjie Dong, Kevin Schell, Benjamin Lu, Eric Kim, Mary Quinn, Shea Thompson, Nathaniel Grady, et al., *Compact solar autoclave based on steam generation using broadband light-harvesting nanoparticles*, Proceedings of the National Academy of Sciences 110 (2013), no. 29, 11677–11681. 4, 25

[21] Dietrich Stauffer and Ammon Aharony, *Introduction to percolation theory*, CRC press, 1994. 4, 49, 50

[22] P Gadenne, Y Yagil, and G Deutscher, *Transmittance and reflectance insitu measurements of semicontinuous gold films during deposition*, Journal of applied physics 66 (1989), no. 7, 3019–3025. 4, 26, 31

[23] K Kolwas, A Derkachova, and S Demianiuk, *The smallest free-electron sphere sustaining*

multipolar surface plasmon oscillation, Computational materials science 35 (2006), no. 3, 337–341. 7

[24] Hendrik Christoffel Van de Hulst and V Twersky, *Light scattering by small particles*, Physics Today 10 (1957), no. 12, 28–30. 8

[25] Gustav Mie, *Contributions to the optics of opaque media, especially colloidal metal solutions*, Annalen der physik 330 (1908), no. 3, 377–445. 12

[26] Arthur L Aden and Milton Kerker, *Scattering of electromagnetic waves from two concentric spheres*, Journal of Applied Physics 22 (1951), no. 10, 1242–1246. 16

[27] JC Maxwell Garnett, *Colours in metal glasses, in metallic films, and in metallic solutions. ii*, Philosophical Transactions of the Royal Society of London. Series A, Containing Papers of a Mathematical or Physical Character (1906), 237–288. 17

[28] Von DAG Bruggeman, *Calculation of different physical constants of heterogeneous substances. i. dielectric configurations and conductances of the mixing compounds of isotropic substances*, Annals of physics 416 (1935), no. 7, 636–664. 17

[29] Vladimir M Shalaev, *Optical properties of nanostructured random media*, vol. 82, Springer Science & Business Media, 2002. 17, 18

[30] Y Yagil, M Yosefin, DJ Bergman, G Deutscher, and P Gadenne, *Scaling theory for the optical properties of semicontinuous metal films*, Physical Review B 43 (1991), no. 13, 11342. 17

[31] Uwe Kreibig and Michael Vollmer, *Optical properties of metal clusters*, vol. 25, Springer Science & Business Media, 2013. 18, 31, 43

[32] David J Bergman, *The dielectric constant of a composite materiala problem in classical physics*, Physics Reports 43 (1978), no. 9, 377–407. 19

[33] Tan Pham, Joseph B Jackson, Naomi J Halas, and T Randall Lee, *Preparation and characterization of gold nanoshells coated with self-assembled monolayers*, Langmuir 18 (2002), no. 12, 4915–4920. 20, 51, 59

[34] Steven J Oldenburg, Joseph B Jackson, Sarah L Westcott, and NJ Halas, *Infrared extinction*

properties of gold nanoshells, Applied Physics Letters 75 (1999), no. 19, 2897–2899. 20, 43

[35] Julia Lovell, *The great wall: China against the world, 1000 bc-ad 2000*, Grove/Atlantic, Inc., 2007. 25

[36] Adrienne Mayor, *Greek fire, poison arrows, and scorpion bombs: biological & chemical warfare in the ancient world*, Penguin, 2008. 25

[37] J Thomas Hanley, BJ Wattle, and EJ Mack, *Extinction characteristics of pyrotechnically-generated alkali-halide smokes*, Tech. report, CALSPAN ADVANCED TECHNOLOGY CENTER BUFFALO NY, 1981. 26

[38] Merrill E Milham, DH Anderson, and RH Frickel, *Infrared optical properties of phosphorus-derived smoke*, Applied optics 21 (1982), no. 14, 2501–2507. 26

[39] GK Gautam, AD Joshi, SA Joshi, PR Arya, and MR Somayajulu, *Radiometric screening of red phosphorus smoke for its obscuration characteristics*, Defence Science Journal 56 (2006), no. 3, 377. 26

[40] Steven Oldenburg and John Holecek, *Surface modified tio2 obscurants for increased safety and performance*, Tech. report, NANOCOMPOSIX INC SAN DIEGO CA, 2012. 26

[41] Stanisław Cudziło and Andrzej Papliński, *An influence of the chemical structure of smoke-generating mixtures on laser radiation attenuation at 1.06-μm and 10.6-μm wavelengths*, Propellants, Explosives, Pyrotechnics 24 (1999), no. 4, 242–245. 26

[42] National Research Council et al., *Toxicity of military smokes and obscurants*, vol. 1, National Academies Press, 1997. 26

[43] JC Owrutsky, HH Nelson, HD Ladouceur, and AP Baronavski, *Obscurants for infrared countermeasures ii*, Tech. report, NAVAL RESEARCH LAB WASHINGTON DC, 2000. 26

[44] Brendan G DeLacy, David R Redding, and Joshua Matthews, *Optical, physical, and chemical properties of surface modified titanium dioxide powders*, Tech. report, ARMY EDGEWOOD CHEMICAL BIOLOGICAL CENTER APG MD RESEARCH AND TECHNOLOGY DIR, 2011. 26

[45] Paul G Appleyard and Nigel Davies, *Calculation and measurement of infrared mass extinction coefficients of selected ionic and partially ionic insulators and semiconductors: a guide for infrared obscuration applications*, Optical Engineering 43 (2004), no. 2, 376–386. 26

[46] National Research Council, *Toxicity of military smokes and obscurants volume 2*, The National Academies Press, 1999. 26

[47] Columbus Chemical Industries, Inc., *Graphite*, 1 2009. 26

[48] Charles W Bruce and Sharhabeel Alyones, *Extinction efficiencies for metallic fibers in the infrared*, Applied optics 48 (2009), no. 27, 5095–5098. 26

[49] Sharhabeel Alyones and Charles W Bruce, *Electromagnetic scattering and absorption by randomly oriented fibers*, JOSA A 32 (2015), no. 6, 1101–1108. 26

[50] RF Voss, RB Laibowitz, and EI Allessandrini, *Fractal (scaling) clusters in thin gold films near the percolation threshold*, Physical Review Letters 49 (1982), no. 19, 1441. 26, 31

[51] Yoad Yagil, Patrice Gadenne, Christian Julien, and Guy Deutscher, *Optical properties of thin semicontinuous gold films over a wavelength range of 2.5 to 500 μm*, Physical Review B 46 (1992), no. 4, 2503. 26, 49, 50, 52, 56, 58, 59

[52] Mark I Stockman, Lakshmi N Pandey, Leonid S Muratov, and Thomas F George, *Optical absorption and localization of eigenmodes in disordered clusters*, Physical Review B 51 (1995), no. 1, 185. 26, 49, 52

[53] Mark D Thoreson, Jieran Fang, Alexander V Kildishev, Ludmila J Prokopeva, Piotr Nyga, Uday K Chettiar, Vladimir M Shalaev, and Vladimir P Drachev, *Fabrication and realistic modeling of three-dimensional metal-dielectric composites*, Journal of Nanophotonics 5 (2011), no. 1, 051513–051513. 26, 49, 52

[54] Andrey K Sarychev and Vladimir M Shalaev, *Electrodynamics of metamaterials*, World Scientific, 2007. 26, 49, 52

[55] AV Karpov, AK Popov, SG Rautian, VP Safonov, VV Slabko, VM Shalaev, and MI Stockman, *Observation of a wavelength-and polarization-selective photomodification of silver clusters*, JETP Lett 48 (1988), no. 10, 571. 26, 40, 43, 47

[56] VP Safonov, VM Shalaev, VA Markel, Yu E Danilova, Ni N Lepeshkin, W Kim, SG Rautian,

and RL Armstrong, *Spectral dependence of selective photomodification in fractal aggregates of colloidal particles*, Physical review letters 80 (1998), no. 5, 1102. 26, 47

[57] P Nyga, VP Drachev, Mark D Thoreson, and VM Shalaev, *Mid-ir plasmonics and photomodification with ag films*, Applied Physics B: Lasers and Optics 93 (2008), no. 1, 59–68. 26, 44, 47, 48, 49, 52

[58] Arthur L Aden and Milton Kerker, *Scattering of electromagnetic waves from two concentric spheres*, Journal of Applied Physics 22 (1951), no. 10, 1242–1246. 27, 49, 50

[59] Milton Kerker, *Invisible bodies*, JOSA 65 (1975), no. 4, 376–379. 27, 49

[60] H Chew and M Kerker, *Abnormally low electromagnetic scattering cross sections*, JOSA 66 (1976), no. 5, 445–449. 27, 49

[61] SJ Oldenburg, RD Averitt, SL Westcott, and NJ Halas, *Nanoengineering of optical resonances*, Chemical Physics Letters 288 (1998), no. 2, 243–247. 27, 43, 49

[62] Charles A Rohde, Keisuke Hasegawa, and Miriam Deutsch, *Coherent light scattering from semicontinuous silver nanoshells near the percolation threshold*, Physical review letters 96 (2006), no. 4, 045503. 27, 49, 50, 56, 59

[63] Vashista C de Silva, Piotr Nyga, and Vladimir P Drachev, *Scattering suppression in epsilon-near-zero plasmonic fractal shells*, Optical Materials Express 5 (2015), no. 11, 2491–2500. 27

[64] *Matlab image processing toolbox*, 2014a, The MathWorks, Natick, MA, USA. 29, 38

[65] A Lee Smith, *Infrared spectra-structure correlations for organosilicon compounds*, Spectrochimica acta 16 (1960), no. 1-2, 87–105. 34, 36, 51, 53

[66] Gorachand Ghosh, *Dispersion-equation coefficients for the refractive index and birefringence of calcite and quartz crystals*, Optics communications 163 (1999), no. 1, 95–102. 36

[67] June D Passaretti, Trudy D Young, Michael J Herman, Kevin S Duane, and D Bruce Evans, *Application of high-opacity precipitated calcium carbonate*, Tappi journal (USA) (1993). 36

[68] S. Grésillon, L. Aigouy, A. C. Boccara, J. C. Rivoal, X. Quelin, C. Desmarest, P. Gadenne,

V. A. Shubin, A. K. Sarychev, and V. M. Shalaev, *Experimental observation of localized optical excitations in random metal-dielectric films*, Phys. Rev. Lett. 82 (1999), 4520–4523. 40

[69] S Gresillon, J-Cl Rivoal, P Gadenne, X Quelin, V Shalaev, and A Sarychev, *Nanoscale observation of enhanced electromagnetic field*, physica status solidi(a) 175 (1999), no. 1, 337–343. 40

[70] Yu E Danilova, NN Lepeshkin, SG Rautian, and VP Safonov, *Excitation localization and nonlinear optical processes in colloidal silver aggregates*, Physica A: Statistical Mechanics and its Applications 241 (1997), no. 1-2, 231–235. 40, 43

[71] V. P. Safonov, V. M. Shalaev, V. A. Markel, Yu. E. Danilova, N. N. Lepeshkin, W. Kim, S. G. Rautian, and R. L. Armstrong, *Spectral dependence of selective photomodification in fractal aggregates of colloidal particles*, Phys. Rev. Lett. 80 (1998), 1102–1105. 40, 43

[72] Ralph Weissleder et al., *A clearer vision for in vivo imaging*, Nature biotechnology 19 (2001), no. 4, 316–316. 43

[73] Garif Akchurin, Boris Khlebtsov, Georgy Akchurin, Valery Tuchin, Vladimir Zharov, and Nikolai Khlebtsov, *Gold nanoshell photomodification under a single-nanosecond laser pulse accompanied by color-shifting and bubble formation phenomena*, Nanotechnology 19 (2007), no. 1, 015701. 43

[74] Richard D Averitt, Sarah L Westcott, and Naomi J Halas, *Linear optical properties of gold nanoshells*, JOSA B 16 (1999), no. 10, 1824–1832. 43

[75] Daniel Werner, Shuichi Hashimoto, and Takayuki Uwada, *Remarkable photothermal effect of interband excitation on nanosecond laser-induced reshaping and size reduction of pseudospherical gold nanoparticles in aqueous solution*, Langmuir 26 (2010), no. 12, 9956–9963. 44

[76] Stephan Link, Clemens Burda, B Nikoobakht, and Mostafa A El-Sayed, *Laser-induced shape changes of colloidal gold nanorods using femtosecond and nanosecond laser pulses*, The Journal of Physical Chemistry B 104 (2000), no. 26, 6152–6163. 44

[77] Christopher J DeSantis, Da Huang, Hui Zhang, Nathaniel J Hogan, Hangqi Zhao, Yifei

Zhang, Alejandro Manjavacas, Yue Zhang, Wei-Shun Chang, Peter Nordlander, et al., *Laser-induced spectral hole-burning through a broadband distribution of au nanorods*, The Journal of Physical Chemistry C 120 (2015), no. 37, 20518–20524. 44

[78] Hristina Petrova, Jorge Perez Juste, Isabel Pastoriza-Santos, Gregory V Hartland, Luis M Liz-Marzán, and Paul Mulvaney, *On the temperature stability of gold nanorods: comparison between thermal and ultrafast laser-induced heating*, Physical Chemistry Chemical Physics 8 (2006), no. 7, 814–821. 44

[79] Carla M Aguirre, Cristin E Moran, James F Young, and Naomi J Halas, *Laser-induced reshaping of metallodielectric nanoshells under femtosecond and nanosecond plasmon resonant illumination*, The Journal of Physical Chemistry B 108 (2004), no. 22, 7040–7045. 44

[80] Dehui Wan, Hsuen-Li Chen, Shao-Chin Tseng, Lon A Wang, and Yung-Pin Chen, *One-shot deep-uv pulsed-laser-induced photomodification of hollow metal nanoparticles for high-density data storage on flexible substrates*, ACS nano 4 (2009), no. 1, 165–173. 44

[81] Andrea Alù and Nader Engheta, *Achieving transparency with plasmonic and metamaterial coatings*, Physical Review E 72 (2005), no. 1, 016623. 49

[82] Mário G Silveirinha, Andrea Alù, and Nader Engheta, *Parallel-plate metamaterials for cloaking structures*, Physical Review E 75 (2007), no. 3, 036603. 49

[83] Felicia Tam, Allen L Chen, Janardan Kundu, Hui Wang, and Naomi J Halas, *Mesoscopic nanoshells: geometry-dependent plasmon resonances beyond the quasistatic limit*, The Journal of chemical physics 127 (2007), no. 20, 204703. 49

[84] Christina Graf and Alfons van Blaaderen, *Metallodielectric colloidal core- shell particles for photonic applications*, Langmuir 18 (2002), no. 2, 524–534. 49, 50

[85] Tianhao Ji, Vladislav G Lirtsman, Yair Avny, Dan Davidov, et al., *Preparation, characterization, and application of au-shell/polystyrene beads and au-shell/magnetic beads*, Advanced Materials 13 (2001), no. 16, 1253. 49, 50

[86] Y Yagil, M Yosefin, DJ Bergman, G Deutscher, and P Gadenne, *Scaling theory for the*

optical properties of semicontinuous metal films, Physical Review B 43 (1991), no. 13, 11342. 49, 50, 51, 52, 58, 59

[87] MI Stockman, LN Pandey, LS Muratov, and TF George, *Comment on photon scanning tunneling microscopy images of optical excitations of fractal metal colloid clusters*, Physical review letters 75 (1995), no. 12, 2450. 49, 52

[88] MI Stockman, LN Pandey, and TF George, *Inhomogeneous localization of polar eigenmodes in fractals*, Physical Review B 53 (1996), no. 5, 2183. 49, 52

[89] Mark I Stockman, *Inhomogeneous eigenmode localization, chaos, and correlations in large disordered clusters*, Physical Review E 56 (1997), no. 6, 6494. 49, 52

[90] Von DAG Bruggeman, *Calculation of different physical constants of heterogeneous substances. i. dielectric configurations and conductances of the mixing compounds of isotropic substances*, Annals of physics 416 (1935), no. 7, 636–664. 50, 55

[91] PerkinElmer Inc., *Applications and Use of Integrating Sphere*, Tech. report, PerkinElmer Inc., 2004. 51, 53, 60

[92] IH Malitson, *Interspecimen comparison of the refractive index of fused silica*, Josa 55 (1965), no. 10, 1205–1209. 55

[93] TR Steyer, Kenrick L Day, and Donald R Huffman, *Infrared absorption by small amorphous quartz spheres*, Applied optics 13 (1974), no. 7, 1586–1590. 55

[94] Peter B Johnson and R-W_ Christy, *Optical constants of the noble metals*, Physical review B 6 (1972), no. 12, 4370. 55, 56

[95] Kuo-Ping Chen, Vladimir P Drachev, Joshua D Borneman, Alexander V Kildishev, and Vladimir M Shalaev, *Drude relaxation rate in grained gold nanoantennas*, Nano letters 10 (2010), no. 3, 916–922. 56

[96] GP Motulevich and VI Malyshev, *Optical properties of metals and intermolecular interactions*, Consultants bureau, 1973. 56

[97] Kahng Dawon, *Electric field controlled semiconductor device*, August 27 1963, US Patent 3,102,230. 62

[98] David J Bergman and Mark I Stockman, *Surface plasmon amplification by stimulated emis-*

sion of radiation: quantum generation of coherent surface plasmons in nanosystems, Physical review letters 90 (2003), no. 2, 027402. 62

[99] Mark I Stockman and David J Bergman, *Surface plasmon amplification by stimulated emission of radiation (spaser)*, August 4 2009, US Patent 7,569,188. 62

[100] MA Noginov, G Zhu, AM Belgrave, Reuben Bakker, VM Shalaev, EE Narimanov, S Stout, E Herz, T Suteewong, and U Wiesner, *Demonstration of a spaser-based nanolaser*, Nature 460 (2009), no. 7259, 1110. 62

[101] Mark I Stockman, *Spasers explained*, Nature Photonics 2 (2008), no. 6, 327–329. 62

[102] Martin T Hill, Milan Marell, Eunice SP Leong, Barry Smalbrugge, Youcai Zhu, Minghua Sun, Peter J Van Veldhoven, Erik Jan Geluk, Fouad Karouta, Yok-Siang Oei, et al., *Lasing in metal-insulator-metal sub-wavelength plasmonic waveguides*, Optics express 17 (2009), no. 13, 11107–11112. 62

[103] Rupert F Oulton, Volker J Sorger, Thomas Zentgraf, Ren-Min Ma, Christopher Gladden, Lun Dai, Guy Bartal, and Xiang Zhang, *Plasmon lasers at deep subwavelength scale*, Nature 461 (2009), no. 7264, 629. 62

[104] Ivan A Larkin and Mark I Stockman, *Imperfect perfect lens*, Nano Letters 5 (2005), no. 2, 339–343. 63

[105] Vasily V Temnov and Ulrike Woggon, *Superradiance and subradiance in an inhomogeneously broadened ensemble of two-level systems coupled to a low-q cavity*, Physical review letters 95 (2005), no. 24, 243602. 64, 65, 81, 82

[106] Robert H Dicke, *Coherence in spontaneous radiation processes*, Physical Review 93 (1954), no. 1, 99. 65

[107] David P Lyvers, Vashista C de Silva, Mojtaba Moazzezi, , Dean P Brown, Augustine M Urbas, Yuri Rostovtsev, and Vladimir P Drachev, *Bi-exponential decay of dye emission near plasmonic surface*, In preparation (2017). 65

[108] Xiaohu Xia, Yang Liu, Vadim Backman, and Guillermo A Ameer, *Engineering sub-100 nm multi-layer nanoshells*, Nanotechnology 17 (2006), no. 21, 5435. 66

[109] *Product information: Atto 655*, 3 2016, Am Eichenhang 50, D-57076 Siegen, Germany. 70, 80

[110] M Wahl and S Orthaus, *Technical note on tttr*, 2004. 74, 75, 76